A constitutive theory for the mechanical response of amorphous metals at high temperatures spanning the glass transition temperature: application to microscale thermoplastic forming of $Zr_{41.2}Ti_{13.8}Cu_{12.5}Ni_{10}Be_{22.5}$

by

David Lee Henann

B.S., State University of New York at Binghamton (2006)

Submitted to the Department of Mechanical Engineering
in partial fulfillment of the requirements for the degree of

Master of Science

at the

Massachusetts Institute of Technology
[June 2008]
May 2008

Author .....
Department of Mechanical Engineering
May 9, 2008

Certified by .....
Lallit Anand
Professor of Mechanical Engineering
Thesis Supervisor

Accepted by .....
Lallit Anand
Chairman, Department Committee on Graduate Students

A constitutive theory for the mechanical response of amorphous metals at high temperatures spanning the glass transition temperature: application to microscale thermoplastic forming of $Zr_{41.2}Ti_{13.8}Cu_{12.5}Ni_{10}Be_{22.5}$

by
David Lee Henann

Submitted to the Department of Mechanical Engineering
on May 9, 2008, in partial fulfillment of the
requirements for the degree of
Master of Science

Abstract

Bulk metallic glasses (BMGs) are a promising emerging engineering material distinguished by their unique mechanical properties and amorphous microstructure. In recent years, an extremely promising microscale processing method for bulk metallic glasses, called thermoplastic-forming has emerged. As with any emerging technology, the scientific basis for this process is at present fragmented and limited. As a result their is no generally agreed upon theory to model the large-deformation, elastic-visco-plastic response of amorphous metals in the temperature range relevant to thermoplastic-forming. What is needed is a unified constitutive framework that is capable of capturing the transition from a elastic-visco-plastic solid-like response below the glass transition to a Newtonian fluid-like response above the glass transition.

We have developed a finite-deformation constitutive theory aimed to fill this need. The material parameters appearing in the theory have been determined to reproduce the experimentally measured stress-strain response of $Zr_{41.2}Ti_{13.8}Cu_{12.5}Ni_{10}Be_{22.5}$ (Vitreloy-1) in a strain rate range of $[10^{-5}, 10^{-1}]\,\mathrm{s}^{-1}$, and in a temperature range $[593, 683]\,\mathrm{K}$, which spans the glass transition temperature $\vartheta_g = 623\mathrm{K}$ of this material. We have implemented our theory in the finite element program ABAQUS/Explicit. The numerical simulation capability of the theory is demonstrated with simulations of micron-scale hot-embossing processes for the manufacture of micro-patterned surfaces.

Thesis Supervisor: Lallit Anand
Title: Professor of Mechanical Engineering

Acknowledgments

First, I would like to thank my advisor Lallit Anand for his support. Under his guidance, I have learned not only a great deal about mechanics and materials but also how to think like a successful researcher. His encouragement to think creatively and push the envelop will continue to be an inspiration throughout my career.

My labmates, as well as the extended mechanics and materials group, have been like a second family. I would particularly like to thank Vikas Srivastava and Shawn Chester for many fruitful discussions, both relevant and irrelevant to our work. Furthermore, I would like to thank Shawn for his various technical assistance and acknowledge that his help comes faster than both the internet and email. An additional thanks to Ray Hardin for his help with various administrative issues, as well as his interest in my musical pursuits.

My roommates Jordan and Andrew have been like yet another family to me and have helped me to maintain some semblance of balance in my life over the last few years. I would also like to thank my girlfriend Stephanie for her support and her ability to bring out the best in life.

Of course, I thank my actual family, particularly my parents, for their constant encouragement and interest.

Financial support for this research was provided by grants from the NSF (CMS-0555614) and the Singapore-MIT Alliance (MST).

And lastly, I dedicate this thesis to my dog, Emily, who passed away during its writing. She brought my family and me many years of happiness and will be fondly remembered.

Contents

List of Figures

List of Tables

Chapter 1

Introduction

Bulk metallic glasses (BMGs) possess unique mechanical properties which make them attractive materials for fabricating components for a variety of applications. For example, the commercial Zr-based alloys exhibit superior tensile strength ($\approx 2.0\,\mathrm{GPa}$), high yield strain ($\approx 2\%$), relatively high fracture toughness ($\approx 10 - 40\,\mathrm{MPa}\sqrt{\mathrm{m}}$), and good corrosion resistance [cf., e.g., 1–3]. *A particularly important characteristic of metallic glasses is their intrinsic homogeneity to the nanoscale because of the absence of grain boundaries.* This characteristic, coupled with their unique mechanical properties, makes them ideal materials for fabricating micron-scale components, or high-aspect-ratio micro-patterned surfaces, which may in turn be used, for example, as dies for the manufacture of polymeric microfluidic devices. However, in order to realize the potential of BMGs in such applications, robust materials-processing techniques for fabricating microscale features and components must be developed.

In recent years, an extremely promising method called thermoplastic forming has emerged [cf., e.g., 4–9]. The thermal history of this processing method is schematically shown on a time-temperature-transformation (TTT) diagram for a bulk metallic glass in Figure(1-1). In this process, the BMG is first obtained in the amorphous state by traditional die-casting. The shape in this step is not the final shape but in the form of simple plates or rods. The BMG plate (or rod) is then heated into the supercooled liquid region above the glass transition temperature of the material, where it may be isothermally formed to produce intricate microscale patterns and then slowly cooled. Since BMGs in their supercooled region are metastable, they eventually crystallize; however, the crystallization kinetics in BMG alloys are sluggish, and this results in a relatively large temperature-time processing window in which thermoplastic forming may be carried out without crystallization.[1] Further, since the forming is done isothermally and the subsequent cooling is rather slow, and since there is no phase change on cooling, residual stresses and part distortion can be minimized

[1]The temperature-time processing window for thermoplastic forming is typically much larger than that afforded by die-casting.

— all factors which potentially allow for a forming process which is much better controlled than die-casting.

A specific thermoplastic forming process geared towards producing nano/microscale, high-aspect ratio, patterned features on surfaces is that of *micro-hot-embossing*. In this process, the BMG is formed in its supercooled liquid region by pressing it against a master-surface with the desired nano/microscale features (usually a patterned silicon wafer). The viability of this process has been demonstrated extensively in the literature [cf., e.g., 4–9]. However, as with any emerging technology, the scientific basis for this process is at present fragmented and limited. Experiments to determine the stress-strain response of BMGs in the appropriate temperature and strain-rate regime required to develop mechanistically-informed continuum-level constitutive equations useful for applications are just beginning to appear [cf., e.g., 10, 11]. Because of this, numerically-based process-simulation capabilities for thermoplastic forming of BMGs also do not exist, and most of the recent experimental micro-hot-embossing studies have been conducted by trial-and-error.

While no set of widely-accepted constitutive equations spanning the necessary range of processing temperatures and strain rates exists, some recent progress towards this end has been made by [12, 13].[2] In addition, in two recent papers Anand and Su [15, 16] have developed a continuum-level constitutive theory aimed at modeling the room-temperature response of metallic glasses, and in [17] these authors have extended their theory to model the response of metallic glasses at high homologous temperatures in the range $0.7\vartheta_g \lesssim \vartheta \lesssim 0.9\vartheta_g$. The purpose of this thesis is to build on the constitutive framework of Anand and Su to represent the mechanical response of metallic glasses in the temperature range $0.9\vartheta_g \lesssim \vartheta \lesssim \vartheta_x$ where $\vartheta_x > \vartheta_g$ is the first crystallization temperature of the material; the higher-end of this temperature range is of utmost importance for thermoplastic forming.

The structure of this thesis is as follows. In Chapter 2, we recall the constitutive framework of Anand and Su [15–17] for bulk metallic glasses. In Chapter 3, we specialize this theory to model the elastic-viscoplastic response of metallic glasses in the temperature range $0.9\vartheta_g \lesssim \vartheta \lesssim \vartheta_x$. We use the experimental data of [10] for the widely studied metallic glass $Zr_{41.2}Ti_{13.8}Cu_{12.5}Ni_{10}Be_{22.5}$ (Vitreloy-1) to estimate the material parameters appearing in our specialized equations, and using the specialized model, we compare the numerically-calculated stress-strain curves with the corresponding experimental results. We have implemented our constitutive model in the finite element program ABAQUS/Explicit (2006). In Chapter 4, we use this simulation capability to determine appropriate processing conditions for several micron-scale hot-embossing processes and compare results from the hot-embossing simulations against results from corresponding physical experiments. We close in Chapter 5 with some final remarks.

[2] Also see [10, 14]; however, these two sets of authors use a "fictive-stress" model, whose physical basis we do not comprehend.

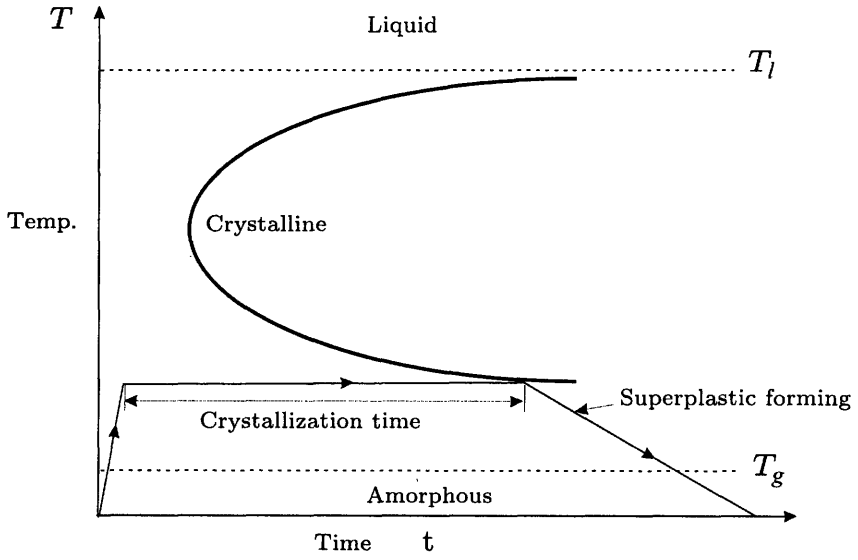

Figure 1-1: A schematic time-temperature-transformation (TTT) diagram for a bulk metallic glass. The processing route for thermoplastic forming is shown: the amorphous metal is heated into the supercooled region, isothermally formed, and then slowly cooled.

Bibliography

[1] A. Inoue. Stabilization of metallic supercooled liquid and bulk amorphous alloys. *Acta Materialia*, 48:279–306, 2000.

[2] W. L. Johnson. Bulk glass forming metallic alloys: science and technology. *MRS Bulletin*, 24:7249–7251, 1999.

[3] C. A. Schuh, T. C. Hufnagel, and U. Ramamurty. Mechanical behavior of amorphous alloys. *Acta Materialia*, 55:4067–4109, 2007.

[4] Y. Saotome, S. Miwa, T. Zhang, and A. Inoue. The micro-formability of Zr-based amorphous alloys in the supercooled liquid state and their application to micro-dies. *Journal of Materials Processing Technology*, 113:64–69, 2001.

[5] Y. Saotome, K. Itoh, T. Zhang, and A. Inoue. Superplastic nanoforming of Pd-based amorphous alloys. *Scripta Materialia*, 44:1541–1545, 2001.

[6] Y. Saotome, K. Itoh, T. Zhang, and A. Inoue. The micro-nanoformability of Pt-based metallic glass and the nanoforming of three-dimensional structures. *Intermetallics*, 104: 1241–1247, 2002.

[7] Y. Saotome, Y. Noguchi, T. Zhang, and A. Inoue. Characteristic behavior of Pt-based metallic glass under rapid heating and its application to microforming. *Materials Science and Engineering A*, 375:389–393, 2004.

[8] J. Schroers. The superplastic forming of bulk metallic glasses. *Journal of Metals*, 57, 2005.

[9] J. Schroers, T. Nguyen, and A Desai. Thermoplastic forming of bulk metallic glass — a technology for MEMS and microstructure fabrication. *Journal of Microelectromechanical Systems*, 16, 2007.

[10] J. Lu, G. Ravichandran, and W. L. Johnson. Deformation behavior of the $Zr_{41.2}Ti_{13.8}Cu_{12.5}Ni_{10.0}Be_{22.5}$ bulk metallic glass over a wide range of strain-rates and temperatures. *Acta Materialia*, 51:3429–3443, 2003.

[11] B. Gun, K. J. Laws, and M. Ferry. Superplastic flow of a Mg-based bulk metallic glass in the supercooled liquid region. *Journal of non-crystalline solids*, 352:3896–3902, 2006.

[12] Q. Yang, A. Mota, and M. Ortiz. A finite deformation constitutive model of bulk metallic glass plasticity. *Computational Mechanics*, 37:194–204, 2006.

[13] P. Thamburaja and R. Ekambaram. Coupled thermo-mechanical modelling of bulk-metallic glasses: Theory, finite-element simulations and experimental verification. *Journal of the Mechanics and Physics of Solids*, 55:1236–1273, 2007.

[14] H. S. Kim, H. Kato, A. Inoue, and H. S. Chen. Finite element analysis of compressive deformation of bulk metallic glasses. *Acta Materialia*, 52:3813–3823, 2004.

[15] L. Anand and C. Su. A theory for amorphous viscoplastic materials undergoing finite deformations, with application to metallic glasses. *Journal of Mechanics and Physics of Solids*, 53:1362–1396, 2005.

[16] C. Su and L. Anand. Plane strain indentation of a Zr-based metallic glass: Experiments and numerical simulation. *Acta Materialia*, 54:179–189, 2006.

[17] L. Anand and C. Su. A constitutive theory for metallic glasses at high homologous temperatures. *Acta Materialia*, 55, 2007.

[18] ABAQUS, Inc. ABAQUS Reference Manuals, 2006.

Chapter 2

Finite-deformation Theory

2.1 Introduction

An accurate quantitative description of the elastic-viscoplastic constitutive response of metallic glasses at high temperatures spanning their glass transition temperature is crucial for the development of a numerical capability for simulation of thermoplastic forming of metallic glasses. The constitutive theory developed in this chapter is based on the work of Anand and Su [1–3].

An essential kinematical ingredient of elastic-viscoplastic constitutive theories for metallic glasses is the classical Kröner [4]- Lee [5] multiplicative decomposition

$$\mathbf{F} = \mathbf{F}^e\mathbf{F}^p \tag{2.1}$$

of the deformation gradient $\mathbf{F}$ into elastic and plastic parts $\mathbf{F}^e$ and $\mathbf{F}^p$ [e.g., 1–3, 6, 7].

It is important to note from the outset that $\mathbf{F}^p$ is to be regarded as an internal variable of the theory whose evolution is determined by an equation of the form $\dot{\mathbf{F}}^p = \mathbf{L}^p\mathbf{F}^p$ (to be discussed shortly), with $\mathbf{F}^e$ then defined by $\mathbf{F}^e \stackrel{\text{def}}{=} \mathbf{F}\mathbf{F}^{p-1}$. Hence $\mathbf{F}^p$ and $\mathbf{F}^e$ in the decomposition (2.1) are not purely kinematical in nature, as they are not defined independently of constitutive equations.

2.2 Notation

We use standard notation of modern continuum mechanics. Specifically: ∇ and Div denote the gradient and divergence with respect to the material point $\mathbf{X}$ in the *reference configuration*; grad and div denote these operators with respect to the point $\mathbf{x} = \boldsymbol{\chi}(\mathbf{X}, t)$ in the *deformed body*; a superposed dot denotes the material time-derivative. Throughout, we write $\mathbf{F}^{e-1} = (\mathbf{F}^e)^{-1}$, $\mathbf{F}^{p-\top} = (\mathbf{F}^p)^{-\top}$, etc. We write $\operatorname{tr}\mathbf{A}$, $\operatorname{sym}\mathbf{A}$, $\operatorname{skw}\mathbf{A}$, $\mathbf{A}_0$, and $\operatorname{sym}_0\mathbf{A}$ respec-

tively, for the trace, symmetric, skew, deviatoric, and symmetric-deviatoric parts of a tensor $\mathbf{A}$. Also, the inner product of tensors $\mathbf{A}$ and $\mathbf{B}$ is denoted by $\mathbf{A}:\mathbf{B}$, and the magnitude of $\mathbf{A}$ by $|\mathbf{A}| = \sqrt{\mathbf{A}:\mathbf{A}}$.

2.3 Kinematics

2.3.1 Basic Kinematics

We consider a homogeneous body B identified with the region of space it occupies in a fixed *reference configuration*, and denote by $\mathbf{X}$ an arbitrary material point of B. A *motion* of B is then a smooth one-to-one mapping $\mathbf{x} = \boldsymbol{\chi}(\mathbf{X}, t)$ with *deformation gradient*, *velocity*, and *velocity gradient* given by

$$\mathbf{F} = \nabla\boldsymbol{\chi}, \qquad \mathbf{v} = \dot{\boldsymbol{\chi}}, \qquad \mathbf{L} = \operatorname{grad}\mathbf{v} = \dot{\mathbf{F}}\mathbf{F}^{-1}. \tag{2.2}$$

To model the inelastic response of the material we assume that the deformation gradient $\mathbf{F}$ may be decomposed as

$$\mathbf{F} = \mathbf{F}^e\mathbf{F}^p. \tag{2.3}$$

As is standard, we assume that

$$J = \det\mathbf{F} > 0,$$

and consistent with this we assume that

$$J^e \stackrel{\text{def}}{=} \det\mathbf{F}^e > 0, \qquad J^p \stackrel{\text{def}}{=} \det\mathbf{F}^p > 0, \tag{2.4}$$

so that $\mathbf{F}^e$ and $\mathbf{F}^p$ are invertible.

Restrict attention to a prescribed *material point* $\mathbf{X}$, and let $\mathbf{x}$ denote its place in the deformed configuration at a fixed time t. Then, bearing in mind that (for $\mathbf{X}$ fixed) the linear transformations $\mathbf{F}^e(\mathbf{X})$ and $\mathbf{F}^p(\mathbf{X})$ at $\mathbf{X}$ are invertible, we let

$$\mathcal{M}_{\mathbf{X}} \stackrel{\text{def}}{=} \text{range of } \mathbf{F}^p(\mathbf{X}) = \text{domain of } \mathbf{F}^e(\mathbf{X}), \tag{2.5}$$

and refer to $\mathcal{M}_{\mathbf{X}}$ as the *intermediate space* at $\mathbf{X}$. $\mathcal{M}_{\mathbf{X}}$ plays roles for $\mathbf{F}^p(\mathbf{X})$ and $\mathbf{F}^e(\mathbf{X})$ analogous to those played by the infinitesimal neighborhoods of $\mathbf{X}$ and $\mathbf{x}$ for $\mathbf{F}$: $\mathbf{F}^p(\mathbf{X})$ is a linear transformation of an infinitesimal neighborhood of $\mathbf{X}$ to $\mathcal{M}_{\mathbf{X}}$; $\mathbf{F}^e(\mathbf{X})$ is a linear transformation from $\mathcal{M}_{\mathbf{X}}$ to an infinitesimal neighborhood of $\mathbf{x}$. Unlike the reference and deformed configurations, which are *global*, each intermediate space $\mathcal{M}_{\mathbf{X}}$ is *local. Note that the local intermediate space $\mathcal{M}_{\mathbf{X}}$ is only a mathematical construct, it is not local a "configuration" actually occupied by the body.*

We refer to $\mathbf{F}^p$ and $\mathbf{F}^e$ as the *plastic and elastic parts* of $\mathbf{F}$. Physically,

- $\mathbf{F}^p(\mathbf{X})$ represents the *local* plastic deformation of the *material* at $\mathbf{X}$ due to "plastic mechanisms" such as the cumulative effects of inelastic transformations resulting from

the cooperative action of atomic clusters in metallic glasses in a microscopic neighborhood of $\mathbf{X}$. This local deformation carries the material into — and ultimately "pins" the material to — a *coherent structure* that resides in the *intermediate space* at $\mathbf{X}$ (as represented by the range of $\mathbf{F}^p(\mathbf{X})$);

- $\mathbf{F}^e(\mathbf{X})$ represents the subsequent stretching and rotation of this coherent structure, and thereby represents the "elastic mechanisms," such as stretching and rotation of the interatomic structure in metallic glasses.

By $(2.2)_3$ and (2.3),

$$\mathbf{L} = \operatorname{grad} \mathbf{v} = \mathbf{L}^e + \mathbf{F}^e \mathbf{L}^p \mathbf{F}^{e-1}, \tag{2.6}$$

with

$$\mathbf{L}^e = \dot{\mathbf{F}}^e \mathbf{F}^{e-1}, \qquad \mathbf{L}^p = \dot{\mathbf{F}}^p \mathbf{F}^{p-1}. \tag{2.7}$$

As is standard, we define the total, elastic, and plastic stretching and spin tensors through

$$\left.\begin{aligned} \mathbf{D} &= \operatorname{sym} \mathbf{L}, & \mathbf{W} &= \operatorname{skw} \mathbf{L}, \\ \mathbf{D}^e &= \operatorname{sym} \mathbf{L}^e, & \mathbf{W}^e &= \operatorname{skw} \mathbf{L}^e, \\ \mathbf{D}^p &= \operatorname{sym} \mathbf{L}^p, & \mathbf{W}^p &= \operatorname{skw} \mathbf{L}^p, \end{aligned}\right\} \tag{2.8}$$

so that $\mathbf{L} = \mathbf{D} + \mathbf{W}$, $\mathbf{L}^e = \mathbf{D}^e + \mathbf{W}^e$, and $\mathbf{L}^p = \mathbf{D}^p + \mathbf{W}^p$.

The right and left and polar decompositions of $\mathbf{F}^e$ are given by

$$\mathbf{F}^e = \mathbf{R}^e \mathbf{U}^e = \mathbf{V}^e \mathbf{R}^e, \tag{2.9}$$

where $\mathbf{R}^e$ is a rotation (proper orthogonal tensor), while $\mathbf{U}^e$ and $\mathbf{V}^e$ are symmetric, positive-definite tensors with

$$\mathbf{U}^e = \sqrt{\mathbf{F}^{e\top} \mathbf{F}^e}, \qquad \mathbf{V}^e = \sqrt{\mathbf{F}^e \mathbf{F}^{e\top}}. \tag{2.10}$$

Also, the right and left elastic Cauchy-Green tensors are given by

$$\mathbf{C}^e = \mathbf{U}^{e2} = \mathbf{F}^{e\top} \mathbf{F}^e, \qquad \mathbf{B}^e = \mathbf{V}^{e2} = \mathbf{F}^e \mathbf{F}^{e\top}, \tag{2.11}$$

and the right and left inelastic Cauchy-Green tensors by

$$\mathbf{C}^p = \mathbf{U}^{p2} = \mathbf{F}^{p\top} \mathbf{F}^p, \qquad \mathbf{B}^p = \mathbf{V}^{p2} = \mathbf{F}^p \mathbf{F}^{p\top}. \tag{2.12}$$

We refer to

$$\operatorname{tr} \mathbf{L}^p = \operatorname{tr} \mathbf{D}^p \quad \text{as the } \textit{plastic dilatation-rate},$$

and note that

$$j^p = J^p \operatorname{tr} \mathbf{L}^p. \tag{2.13}$$

For later use, we define the *plastic volumetric strain* by

$$\varphi \overset{\text{def}}{=} \varphi_0 + \ln J^p, \tag{2.14}$$

where φ_0 is the plastic volumetric strain when $J^p = 1$; then

$$\dot{\varphi} = \mathrm{tr}\mathbf{L}^p. \tag{2.15}$$

2.4 Frame-indifference

Changes in frame (observer) are smooth time-dependent rigid transformations of the Euclidean space through which the body moves. We require that the theory be invariant under such transformations, and hence under transformations of the form

$$\boldsymbol{\chi}(\mathbf{X}, t) \to \mathbf{Q}(t)(\boldsymbol{\chi}(\mathbf{X}, t) - \mathbf{o}) + \mathbf{y}(t) \tag{2.16}$$

with $\mathbf{Q}(t)$ a rotation (proper-orthogonal tensor), $\mathbf{y}(t)$ a point at each t, and $\mathbf{o}$ a fixed origin. Then, under a change in observer, the deformation gradient transforms according to

$$\mathbf{F} \to \mathbf{Q}\mathbf{F}. \tag{2.17}$$

Thus, $\dot{\mathbf{F}} \to \mathbf{Q}\dot{\mathbf{F}} + \dot{\mathbf{Q}}\mathbf{F}$, and by $(2.2)_3$,

$$\mathbf{L} \to \mathbf{Q}\mathbf{L}\mathbf{Q}^\top + \dot{\mathbf{Q}}\mathbf{Q}^\top. \tag{2.18}$$

Hence,

$$\mathbf{D} \to \mathbf{Q}\mathbf{D}\mathbf{Q}^\top, \qquad \mathbf{W} \to \mathbf{Q}\mathbf{W}\mathbf{Q}^\top + \dot{\mathbf{Q}}\mathbf{Q}^\top. \tag{2.19}$$

Moreover, $\mathbf{F}^e\mathbf{F}^p \to \mathbf{Q}\mathbf{F}^e\mathbf{F}^p$, and therefore, since *observers view only the deformed configuration*,

$$\mathbf{F}^e \to \mathbf{Q}\mathbf{F}^e, \qquad \mathbf{F}^p \text{ is invariant}, \tag{2.20}$$

and, by $(2.7)_1$,

$$\mathbf{L}^e \to \mathbf{Q}\mathbf{L}^e\mathbf{Q}^\top + \dot{\mathbf{Q}}\mathbf{Q}^\top. \tag{2.21}$$

Hence,

$$\mathbf{D}^e \to \mathbf{Q}\mathbf{D}^e\mathbf{Q}^\top, \qquad \mathbf{W}^e \to \mathbf{Q}\mathbf{W}^e\mathbf{Q}^\top + \dot{\mathbf{Q}}\mathbf{Q}^\top. \tag{2.22}$$

Also, by $(2.7)_2$,

$$\mathbf{L}^p,\ \mathbf{D}^p, \text{ and } \mathbf{W}^p \text{ are invariant}. \tag{2.23}$$

Further, by (2.9),

$$\mathbf{F}^e = \mathbf{R}^e\mathbf{U}^e \to \mathbf{Q}\mathbf{F}^e = \underline{\mathbf{Q}\mathbf{R}^e}\mathbf{U}^e,$$
$$\mathbf{F}^e = \mathbf{V}^e\mathbf{R}^e \to \mathbf{Q}\mathbf{F}^e = \underline{\mathbf{Q}\mathbf{V}^e\mathbf{Q}^\top}\ \mathbf{Q}\mathbf{R}^e,$$

and we may conclude from the uniqueness of the polar decomposition that

$$\mathbf{R}^e \to \mathbf{Q}\mathbf{R}^e, \qquad \mathbf{V}^e \to \mathbf{Q}\mathbf{V}^e\mathbf{Q}^\top, \qquad \mathbf{U}^e \text{ is invariant}. \tag{2.24}$$

Hence, from (2.11), $\mathbf{B}^e$ and $\mathbf{C}^e$ transform as

$$\mathbf{B}^e \to \mathbf{Q}\mathbf{B}^e\mathbf{Q}^\top, \qquad \text{and} \qquad \mathbf{C}^e \text{ is invariant.} \tag{2.25}$$

2.5 Development of the theory based on the principle of virtual power

Following [8–10], the theory presented here is based on the belief that

- *the power expended by each independent "rate-like" kinematical descriptor be expressible in terms of an associated force system consistent with its own balance.*

However, the basic "rate-like" descriptors, namely, $\mathbf{v}$, $\mathbf{L}^e$, and $\mathbf{L}^p$ *are not independent*, since by (2.6) they are constrained by

$$\operatorname{grad}\mathbf{v} = \mathbf{L}^e + \mathbf{F}^e\,\mathbf{L}^p\,\mathbf{F}^{e-1}, \tag{2.26}$$

and it is not apparent what forms the associated force balances should take. It is in such situations that the strength of the principle of virtual power becomes apparent, since *the principle of virtual power automatically determines the underlying force balances.*

2.5.1 External and internal expenditures of power

We write $\mathcal{B}_t = \boldsymbol{\chi}(\mathrm{B}, t)$ for the *deformed body.* We use the term *part* to denote an arbitrary time-dependent subregion $\mathcal{P}_t$ of $\mathcal{B}_t$ that *deforms* with the body, so that

$$\mathcal{P}_t = \boldsymbol{\chi}(\mathrm{P}, t) \tag{2.27}$$

for some *fixed* subregion P of B. The outward unit normal on the boundary $\partial\mathcal{P}_t$ of $\mathcal{P}_t$ is denoted by $\mathbf{n}$.

The power expended on $\mathcal{P}_t$ by material or bodies exterior to $\mathcal{P}_t$ results from a *macroscopic surface traction* $\mathbf{t}(\mathbf{n})$, measured per unit area in the deformed body, and a *macroscopic body force* $\mathbf{b}$, measured per unit volume in the deformed body, each of whose working accompanies the macroscopic motion of the body. The body force $\mathbf{b}$ is assumed to include inertial forces; that is, granted that the underlying frame is inertial,

$$\mathbf{b} = \mathbf{b}_0 - \rho\dot{\mathbf{v}}, \tag{2.28}$$

with $\mathbf{b}_0$ the noninertial body force, and $\rho(\mathbf{x}, t) > 0$ is the mass density in the deformed body. We therefore write the *external power* as

$$\mathcal{W}_{\text{ext}}(\mathcal{P}_t) = \int_{\partial\mathcal{P}_t} \mathbf{t}(\mathbf{n}) \cdot \mathbf{v}\, da + \int_P \mathbf{b} \cdot \mathbf{v}\, dv, \tag{2.29}$$

with $\mathbf{t}(\mathbf{n})$ (for each unit vector $\mathbf{n}$) and $\mathbf{b}$ defined over the body for all time.

We assume that power is expended internally by

- *elastic stresses* $\mathbf{T}$ power-conjugate to $\mathbf{L}^e$, and
- *microstresses* $\mathbf{T}^p$ power-conjugate to $\mathbf{L}^p$,

and we write the *internal power* as

$$\mathcal{W}_{\text{int}}(\mathcal{P}_t) = \int_{\mathcal{P}_t} \left(\mathbf{T} : \mathbf{L}^e + J^{e-1}\, \mathbf{T}^p : \mathbf{L}^p \right) dv\,. \tag{2.30}$$

Here $\mathbf{T}$ and $\mathbf{T}^p$ are defined over the body for all time. The term J^{e-1} arises because the microstress-power $\mathbf{T}^p : \mathbf{L}^p$ is measured per unit volume in the corresponding intermediate space, but the integration is carried out within the deformed body.

2.5.2 Principle of virtual power.

Assume that, at some arbitrarily chosen but *fixed time*, the fields $\boldsymbol{\chi}$ and $\mathbf{F}^e$ (and hence $\mathbf{F}$ and $\mathbf{F}^p$) are known, and consider the fields $\mathbf{v}$, $\mathbf{L}^e$, and $\mathbf{L}^p$ as virtual velocities to be specified independently in a manner consistent with (2.26); that is, denoting the virtual fields by $\tilde{\mathbf{v}}$, $\tilde{\mathbf{L}}^e$, and $\tilde{\mathbf{L}}^p$ to differentiate them from fields associated with the actual evolution of the body, we require that

$$\operatorname{grad} \tilde{\mathbf{v}} = \tilde{\mathbf{L}}^e + \mathbf{F}^e \tilde{\mathbf{L}}^p \mathbf{F}^{e-1}. \tag{2.31}$$

More specifically, we define a *generalized virtual velocity* to be a list

$$\mathcal{V} = (\tilde{\mathbf{v}}, \tilde{\mathbf{L}}^e, \tilde{\mathbf{L}}^p)$$

consistent with (2.31).

We write

$$\left.\begin{aligned} \mathcal{W}_{\text{ext}}(\mathcal{P}_t, \mathcal{V}) &= \int_{\partial \mathcal{P}_t} \mathbf{t}(\mathbf{n}) \cdot \tilde{\mathbf{v}}\, da + \int_{\mathcal{P}_t} \mathbf{b} \cdot \tilde{\mathbf{v}}\, dv, \\ \mathcal{W}_{\text{int}}(\mathcal{P}_t, \mathcal{V}) &= \int_{\mathcal{P}_t} (\mathbf{T} : \tilde{\mathbf{L}}^e + J^{e-1}\, \mathbf{T}^p : \tilde{\mathbf{L}}^p)\, dv, \end{aligned}\right\} \tag{2.32}$$

respectively, for the external and internal expenditures of *virtual power*. Then, the *principle of virtual power* is the requirement that the external and internal powers be balanced. That is

- *given any part* $\mathcal{P}_t$,

$$\mathcal{W}_{\text{ext}}(\mathcal{P}_t, \mathcal{V}) = \mathcal{W}_{\text{int}}(\mathcal{P}_t, \mathcal{V}) \quad \textit{for all generalized virtual velocities } \mathcal{V}. \tag{2.33}$$

2.5.3 Frame-indifference of the internal power and its consequences

To deduce the consequences of the principle of virtual power, assume that (2.33) is satisfied. In applying the virtual balance (2.33) we are at liberty to choose any $\mathcal{V}$ consistent with the constraint (2.31).

We require that

- *the internal power be invariant under a change in frame.*

Thus, consider the internal power $\mathcal{W}_{\text{int}}(\mathcal{P}_t, \mathcal{V})$ under an arbitrary change in frame. In the new frame, $\mathcal{P}_t$ transforms rigidly to a region $\mathcal{P}_t^*$, $\mathbf{T}$ transforms to $\mathbf{T}^*$, $\mathbf{T}^p$ transforms to $\mathbf{T}^{p*}$, $\tilde{\mathbf{L}}^e$ transforms to

$$\tilde{\mathbf{L}}^{e*} = \mathbf{Q}\tilde{\mathbf{L}}^e\mathbf{Q}^\top + \dot{\mathbf{Q}}\mathbf{Q}^\top .$$

and $\tilde{\mathbf{L}}^p$ is invariant. Hence, under a change in frame $\mathcal{W}_{\text{int}}(\mathcal{P}_t, \mathcal{V})$ transforms to

$$\begin{aligned}\mathcal{W}^*_{\text{int}}(\mathcal{P}_t^*, \mathcal{V}^*) &= \int_{\mathcal{P}_t^*} \left\{ \mathbf{T}^* : \left(\mathbf{Q}\tilde{\mathbf{L}}^e\mathbf{Q}^\top + \dot{\mathbf{Q}}\mathbf{Q}^\top \right) + J^{e-1}\, \mathbf{T}^{p*} : \tilde{\mathbf{L}}^p \right\} dv, \\ &= \int_{\mathcal{P}_t} \left\{ \mathbf{T}^* : \left(\mathbf{Q}\tilde{\mathbf{L}}^e\mathbf{Q}^\top + \dot{\mathbf{Q}}\mathbf{Q}^\top \right) + J^{e-1}\, \mathbf{T}^{p*} : \tilde{\mathbf{L}}^p \right\} dv,\end{aligned}$$

where in the second of the equations above, since $\mathcal{P}_t^*$ is simply $\mathcal{P}_t$ transformed *rigidly*, we have replaced the region of integration $\mathcal{P}_t^*$ by $\mathcal{P}_t$.

We deduce below the transformation rules for the elastic stress $\mathbf{T}$ and the microstress $\mathbf{T}^p$ under a change in frame by using the requirement that the internal power be invariant under a change in frame:

$$\mathcal{W}^*_{\text{int}}(\mathcal{P}_t^*, \mathcal{V}^*) = \mathcal{W}_{\text{int}}(\mathcal{P}_t, \mathcal{V}).$$

Since the region $\mathcal{P}_t$ is arbitrary, this requirement yields the relation

$$\mathbf{T}^* : \left(\mathbf{Q}\tilde{\mathbf{L}}^e\mathbf{Q}^\top + \dot{\mathbf{Q}}\mathbf{Q}^\top \right) + J^{e-1}\, \mathbf{T}^{p*} : \tilde{\mathbf{L}}^p = \mathbf{T} : \tilde{\mathbf{L}}^e + J^{e-1}\, \mathbf{T}^p : \tilde{\mathbf{L}}^p.$$

Also, since the change in frame is arbitrary, if we choose it such that $\mathbf{Q}$ is an arbitrary *time-independent* rotation, so that $\dot{\mathbf{Q}} = \mathbf{0}$, we find that

$$\begin{aligned}\mathbf{T} : \tilde{\mathbf{L}}^e + J^{e-1}\, \mathbf{T}^p : \tilde{\mathbf{L}}^p &= \mathbf{T}^* : (\mathbf{Q}\tilde{\mathbf{L}}^e\mathbf{Q}^\top) + J^{e-1}\, \mathbf{T}^{p*} : \tilde{\mathbf{L}}^p \\ &= (\mathbf{Q}^\top\mathbf{T}^*\mathbf{Q}) : \tilde{\mathbf{L}}^e + J^{e-1}\, \mathbf{T}^{p*} : \tilde{\mathbf{L}}^p,\end{aligned}$$

or

$$\left(\mathbf{T} - (\mathbf{Q}^\top\mathbf{T}^*\mathbf{Q}) \right) : \tilde{\mathbf{L}}^e + J^{e-1} \left(\mathbf{T}^p - \mathbf{T}^{p*} \right) : \tilde{\mathbf{L}}^p = 0 .$$

Since this must hold for all $\tilde{\mathbf{L}}^e$ and $\tilde{\mathbf{L}}^p$, we find that the elastic stress $\mathbf{T}$ transforms according to

$$\mathbf{T}^* = \mathbf{Q}\mathbf{T}\mathbf{Q}^\top. \tag{2.34}$$

and the microstress $\mathbf{T}^p$ is invariant:

$$\mathbf{T}^{p*} = \mathbf{T}^p. \tag{2.35}$$

Next, if we assume that $\mathbf{Q} = \mathbf{1}$ at the time in question, so that $\dot{\mathbf{Q}}$ is an arbitrary skew tensor, we find that

$$\mathbf{T} : \dot{\mathbf{Q}} = 0,$$

or that the elastic stress $\mathbf{T}$ is symmetric,

$$\mathbf{T} = \mathbf{T}^\top. \tag{2.36}$$

Finally, using (2.36) we may write the internal power (2.30) as

$$\mathcal{W}_{\text{int}}(\mathcal{P}_t) = \int_{\mathcal{P}_t} (\mathbf{T} : \mathbf{D}^e + J^{e-1}\, \mathbf{T}^p : \mathbf{L}^p)\, dv. \tag{2.37}$$

2.5.4 Macroscopic force balance. Microscopic force balance

As previously stated, to deduce the consequences of the principle of virtual power, assume that (2.33) is satisfied. In applying the virtual balance (2.33) we are at liberty to choose any $\mathcal{V}$ consistent with the constraint (2.31).

First consider a generalized virtual velocity which is strictly elastic in the sense that

$$\tilde{\mathbf{L}}^p \equiv \mathbf{0}, \quad \text{so that by (2.31)} \quad \operatorname{grad} \tilde{\mathbf{v}} = \tilde{\mathbf{L}}^e. \tag{2.38}$$

For this choice of $\mathcal{V}$, (2.33) yields

$$\int_{\partial \mathcal{P}_t} \mathbf{t}(\mathbf{n}) \cdot \tilde{\mathbf{v}}\, da + \int_{\mathcal{P}_t} \mathbf{b} \cdot \tilde{\mathbf{v}}\, dv = \int_{\mathcal{P}_t} \mathbf{T} : \operatorname{grad} \tilde{\mathbf{v}}\, dv.$$

Then, using the divergence theorem,

$$\int_{\partial \mathcal{P}_t} \big(\mathbf{t}(\mathbf{n}) - \mathbf{T}\mathbf{n}\big) \cdot \tilde{\mathbf{v}}\, da + \int_{\mathcal{P}_t} (\operatorname{div} \mathbf{T} + \mathbf{b}) \cdot \tilde{\mathbf{v}}\, dv = 0.$$

Since this relation must hold for all $\mathcal{P}_t$ and all $\tilde{\mathbf{v}}$, standard variational arguments yield the traction condition

$$\mathbf{t}(\mathbf{n}) = \mathbf{T}\mathbf{n}, \tag{2.39}$$

and the local force balance

$$\operatorname{div} \mathbf{T} + \mathbf{b} = \mathbf{0}. \tag{2.40}$$

Recall that we have assumed that that $\mathbf{b}$ includes inertial body forces. Thus, recalling (2.28), the local force balance (2.40) becomes

$$\operatorname{div} \mathbf{T} + \mathbf{b}_0 = \rho \dot{\mathbf{v}}, \tag{2.41}$$

with $\mathbf{b}_0$ the noninertial body force. Therefore, the symmetric stress $\mathbf{T}$ plays the role of the macroscopic *Cauchy stress*, and (2.41) and (2.36) represent the classical *macroscopic force and moment balances.*

Next, to discuss the microscopic counterparts of these results, we choose a generalized virtual velocity field $\mathcal{V}$ for which

$$\tilde{\mathbf{v}} \equiv \mathbf{0}, \quad \text{so that by (2.31)} \quad \tilde{\mathbf{L}}^e = -\mathbf{F}^e \tilde{\mathbf{L}}^p \mathbf{F}^{e-1}. \tag{2.42}$$

Then, the external power vanishes identically, so that, by (2.33), the internal power must also vanish, and satisfy

$$\mathcal{W}_{\text{int}}(\mathcal{P}_t, \mathcal{V}) = \int_{\mathcal{P}_t} J^{e-1} \Big(\mathbf{T}^p - J^e \, \mathbf{F}^{e\top} \mathbf{T} \mathbf{F}^{e-\top} \Big) : \tilde{\mathbf{L}}^p \, dv = 0.$$

Since this must be satisfied for all $\mathcal{P}_t$ and all tensors $\tilde{\mathbf{L}}^p$, a standard argument yields the *microforce balance*

$$\mathbf{M}^e = \mathbf{T}^p, \tag{2.43}$$

where

$$\mathbf{M}^e \stackrel{\text{def}}{=} J^e \mathbf{F}^{e\top} \mathbf{T} \mathbf{F}^{e-\top} \tag{2.44}$$

is a Mandel stress. *The balance* (2.43) *characterizes the interaction between internal forces associated with the elastic response of the material and internal forces associated with inelasticity.*

For later use we introduce a stress measure

$$\mathbf{S}^e \stackrel{\text{def}}{=} J^e \mathbf{F}^{e-1} \mathbf{T} \mathbf{F}^{e-\top}, \tag{2.45}$$

then the corresponding $\mathbf{M}^e$ is given by

$$\mathbf{M}^e = \mathbf{C}^e \mathbf{S}^e. \tag{2.46}$$

2.6 Local dissipation inequality

We consider a purely mechanical theory. Thus, we limit our considerations here to isothermal situations in the absence of temperature gradients. Let

- $\vartheta > 0$ denote the absolute temperature,
- ε and η represent the *specific internal energy* and *specific entropy* densities, measured per unit mass in the deformed body,

Then, *balance of energy* is the requirement that

$$\dot{\int_{\mathcal{P}_t}} \rho \, \varepsilon \, dv = \mathcal{W}_{\text{ext}}(\mathcal{P}_t), \tag{2.47}$$

while the *second law* takes the form of an *entropy imbalance*

$$\overline{\int_{\mathcal{P}_t} \rho\,\eta\,dv}^{\cdot} \geq 0. \tag{2.48}$$

Thus, since $\mathcal{W}_{\text{ext}}(\mathcal{P}_t) = \mathcal{W}_{\text{int}}(\mathcal{P}_t)$ and since $\mathcal{P}_t$ is arbitrary, we may use (2.37) to obtain local forms of (2.47) and (2.48):

$$\left.\begin{aligned} &\rho\,\dot{\varepsilon} = \mathbf{T}:\mathbf{D}^e + J^{e-1}\,\mathbf{T}^p:\mathbf{L}^p, \\ &\rho\,\dot{\eta} \geq 0\,. \end{aligned}\right\} \tag{2.49}$$

Let

$$\psi \overset{\text{def}}{=} \varepsilon - \vartheta\eta \tag{2.50}$$

denote the *specific (Helmholtz) free energy.* Then (2.49) yields the *local dissipation inequality*

$$\rho\dot{\psi} - \mathbf{T}:\mathbf{D}^e - J^{e-1}\,\mathbf{T}^p:\mathbf{L}^p \leq 0\,. \tag{2.51}$$

The free-energy density per unit volume of the intermediate space is given by

$$\psi_{\text{I}} = \rho_{\text{I}}\,\psi. \tag{2.52}$$

Also, note that

$$\rho_{\text{R}} = J^p\rho_{\text{I}}, \quad \rho_{\text{I}} = J^e\rho, \quad \text{and} \quad \rho_{\text{R}} = J\rho. \tag{2.53}$$

Furthermore, taking the time derivative of $(2.53)_1$ and noting that ρ_{R} is not a function of time, we obtain the following expression for the rate of change of ρ_{I}:

$$\dot{\rho}_{\text{I}} = -\rho_{\text{I}}\text{tr}\,\mathbf{L}^p, \tag{2.54}$$

and from (2.52) and (2.54) we obtain an expression for $\dot{\psi}$:

$$\dot{\psi} = \frac{1}{\rho_{\text{I}}}\left(\dot{\psi}_{\text{I}} + \psi_{\text{I}}\text{tr}\,\mathbf{L}^p\right). \tag{2.55}$$

Then multiplying (2.51) through by J^e and using (2.55), we obtain

$$\dot{\psi}_{\text{I}} + \psi_{\text{I}}\text{tr}\,\mathbf{L}^p - J^e\,\mathbf{T}:\mathbf{D}^e - \mathbf{T}^p:\mathbf{L}^p \leq 0, \tag{2.56}$$

Further, differentiating $(2.11)_1$ results in the following expression for the rate of change of $\mathbf{C}^e$:

$$\begin{aligned}\dot{\overline{\mathbf{C}^e}} &= \big(\mathbf{F}^{e\top}\dot{\overline{\mathbf{F}^e}} + \dot{\overline{\mathbf{F}^{e\top}}}\mathbf{F}^e\big)\\ &= \mathbf{F}^{e\top}\big(\dot{\overline{\mathbf{F}^e}}\mathbf{F}^{e-1} + \mathbf{F}^{e-\top}\dot{\overline{\mathbf{F}^{e\top}}}\big)\mathbf{F}^e\\ &= 2\,\mathbf{F}^{e\top}\mathbf{D}^e\mathbf{F}^e. \qquad (2.57)\end{aligned}$$

Hence

$$\mathbf{D}^e = \tfrac{1}{2}\mathbf{F}^{e-\top}\dot{\overline{\mathbf{C}^e}}\mathbf{F}^{e-1}, \qquad (2.58)$$

and therefore

$$J^e\mathbf{T}:\mathbf{D}^e = J^e\mathbf{T}:\Big(\tfrac{1}{2}\mathbf{F}^{e-\top}\dot{\overline{\mathbf{C}^e}}\mathbf{F}^{e-1}\Big) \qquad (2.59)$$

$$= \tfrac{1}{2}\Big(J^e\mathbf{F}^{e-1}\mathbf{T}\mathbf{F}^{e-\top}\Big):\dot{\overline{\mathbf{C}^e}}. \qquad (2.60)$$

Thus using (2.45), we obtain

$$J^e\mathbf{T}:\mathbf{D}^e = \tfrac{1}{2}\mathbf{S}^e:\dot{\overline{\mathbf{C}^e}} \qquad (2.61)$$

For later use, from (2.37), (2.43) and (2.61), we note that the internal power per unit volume of the intermediate space is

$$\tfrac{1}{2}\mathbf{S}^e:\dot{\overline{\mathbf{C}^e}} + \mathbf{T}^p:\mathbf{L}^p\,. \qquad (2.62)$$

Using (2.61) we may rewrite the free-energy imbalance as

$$\dot{\psi}_{\mathrm{I}} + \psi_{\mathrm{I}}\mathrm{tr}\,\mathbf{L}^p - \tfrac{1}{2}\mathbf{S}^e:\dot{\overline{\mathbf{C}^e}} - \mathbf{T}^p:\mathbf{L}^p \le 0, \qquad (2.63)$$

Finally, we note that ψ_{I} and ϑ are invariant under a change in frame since they are scalar fields, and on account of the transformation rules (2.23), (2.25), (2.34) and the definitions (2.44) and (2.45), the fields

$$\mathbf{C}^e, \quad \mathbf{L}^p, \quad \mathbf{S}^e, \quad \text{and} \quad \mathbf{T}^p, \qquad (2.64)$$

are also invariant.

2.7 Constitutive theory

The macroforce balance, the microforce balance, and the dissipation inequality are basic laws, common to large classes of elastic-plastic materials; we keep such laws distinct from specific constitutive equations, which differentiate between particular materials. We view the dissipation inequality (2.63) as a guide in the development of a suitable constitutive theory. In this regard *we do not seek the most general constitutive equations consistent with*

the dissipation inequality; instead we develop *special* constitutive equations close to those upon which the classical theories of plasticity are based.

2.7.1 Constitutive equations

To account for the major strain-hardening characteristics of materials observed during plastic deformation, we introduce a list of n scalar *internal state-variables* $\boldsymbol{\xi} = (\xi^1, \xi^2, \ldots, \xi^n)$ which represent important aspects of the microstructural resistance to plastic flow. Since $\boldsymbol{\xi}$ are scalar fields they invariant under a change in frame.

Guided by the dissipation inequality (2.63), we assume the following special set of constitutive equations:

$$\left.\begin{aligned} \psi_{\mathrm{I}} &= \bar{\psi}_{\mathrm{I}}(\mathbf{C}^e, \varphi, \vartheta), \\ \mathbf{S}^e &= \bar{\mathbf{S}}^e(\mathbf{C}^e, \varphi, \vartheta), \\ \mathbf{T}^p &= \bar{\mathbf{T}}^p(\mathbf{L}^p, \varphi, \boldsymbol{\xi}, \vartheta), \\ \dot{\xi}^i &= h^i(\mathbf{L}^p, \varphi, \boldsymbol{\xi}, \vartheta). \end{aligned}\right\} \tag{2.65}$$

Note that on account of the transformation rules listed in the paragraph containing (2.64) and since $(\varphi, \boldsymbol{\xi}, \vartheta)$ are also invariant,

- *the constitutive equations* (2.65) *are frame-indifferent.*

2.7.2 Thermodynamic restrictions

With a view toward determining the restrictions imposed by the local dissipation inequality, we note that under isothermal conditions

$$\dot{\bar{\psi}}_{\mathrm{I}}(\mathbf{C}^e, \varphi, \vartheta) = \frac{\partial \bar{\psi}_{\mathrm{I}}(\mathbf{C}^e, \varphi, \vartheta)}{\partial \mathbf{C}^e} : \dot{\overline{\mathbf{C}^e}} + \frac{\partial \bar{\psi}_{\mathrm{I}}(\mathbf{C}^e, \varphi, \vartheta)}{\partial \varphi}\dot{\varphi}.$$

Hence, satisfaction of the free-energy imbalance (2.63) requires that the constitutive equations (2.65) satisfy

$$\left[\tfrac{1}{2}\bar{\mathbf{S}}^e(\mathbf{C}^e, \varphi, \vartheta) - \frac{\partial \bar{\psi}_{\mathrm{I}}(\mathbf{C}^e, \varphi, \vartheta)}{\partial \mathbf{C}^e}\right] : \dot{\overline{\mathbf{C}^e}} + \left[\bar{\mathbf{T}}^p(\mathbf{L}^p, \varphi, \boldsymbol{\xi}, \vartheta) - \underbrace{\left(\bar{\psi}_{\mathrm{I}}(\mathbf{C}^e, \varphi, \vartheta) + \frac{\partial \bar{\psi}_{\mathrm{I}}(\mathbf{C}^e, \varphi, \vartheta)}{\partial \varphi}\right)\mathbf{1}}_{\text{this terms originates due to plastic dilatancy}}\right] : \mathbf{L}^p \geq 0. \tag{2.66}$$

Also, defining

$$\mathbf{Y}^p(\mathbf{C}^e,\mathbf{L}^p,\varphi,\boldsymbol{\xi},\vartheta)=\left[\bar{\mathbf{T}}^p(\mathbf{L}^p,\varphi,\boldsymbol{\xi},\vartheta)-\left(\bar{\psi}_{\rm I}(\mathbf{C}^e,\varphi,\vartheta)+\frac{\partial\bar{\psi}_{\rm I}(\mathbf{C}^e,\varphi,\vartheta)}{\partial\varphi}\right)\mathbf{1}\right], \tag{2.67}$$

we may write the free-energy imbalance as

$$\left[\tfrac{1}{2}\bar{\mathbf{S}}^e(\mathbf{C}^e,\varphi,\vartheta)-\frac{\partial\bar{\psi}_{\rm I}(\mathbf{C}^e,\varphi,\vartheta)}{\partial\mathbf{C}^e}\right]:\dot{\overline{\mathbf{C}^e}}+\mathbf{Y}^p(\mathbf{C}^e,\mathbf{L}^p,\varphi,\boldsymbol{\xi},\vartheta):\mathbf{L}^p\geq 0. \tag{2.68}$$

This must hold for all arguments in the domains of the constitutive functions, and in all motions of the body.

Thus, *sufficient* conditions that the constitutive equations satisfy the free-energy imbalance are that

(i) *the free energy determines the stress via the* **stress relation**:

$$\bar{\mathbf{S}}^e(\mathbf{C}^e,\varphi,\vartheta)=2\,\frac{\partial\bar{\psi}_{\rm I}(\mathbf{C}^e,\varphi,\vartheta)}{\partial\mathbf{C}^e}, \tag{2.69}$$

(ii) *the dissipative flow stress function* $\mathbf{Y}^p$ *satisfies the* **mechanical dissipation inequality**

$$\mathbf{Y}^p(\mathbf{C}^e,\mathbf{L}^p,\varphi,\boldsymbol{\xi},\vartheta):\mathbf{L}^p\geq 0. \tag{2.70}$$

The left side of (2.70) represents the rate of *energy dissipation*, measured per unit volume in the intermediate space.

We assume henceforth that (2.69) holds in all motions of the body, and that the material is **strictly dissipative** in the sense

$$\mathbf{Y}^p(\mathbf{C}^e,\mathbf{L}^p,\varphi,\boldsymbol{\xi},\vartheta):\mathbf{L}^p>0 \tag{2.71}$$

whenever $\mathbf{L}^p\neq\mathbf{0}$.

2.7.3 Flow rule

An important result of the theory is the flow rule, obtained upon using (2.67) and the microforce balance (2.43),

$$\mathbf{Y}^p(\mathbf{C}^e,\mathbf{L}^p,\varphi,\boldsymbol{\xi},\vartheta)=\left[\mathbf{M}^e-\left(\bar{\psi}_{\rm I}(\mathbf{C}^e,\varphi,\vartheta)+\frac{\partial\bar{\psi}_{\rm I}(\mathbf{C}^e,\varphi,\vartheta)}{\partial\varphi}\right)\mathbf{1}\right]. \tag{2.72}$$

For conciseness, we define the stress $\boldsymbol{\Sigma}$ as

$$\boldsymbol{\Sigma}\stackrel{\rm def}{=}\left[\mathbf{M}^e-\left(\bar{\psi}_{\rm I}(\mathbf{C}^e,\varphi,\vartheta)+\frac{\partial\bar{\psi}_{\rm I}(\mathbf{C}^e,\varphi,\vartheta)}{\partial\varphi}\right)\mathbf{1}\right]. \tag{2.73}$$

Thus, the flow rule becomes

$$\mathbf{Y}^p(\mathbf{C}^e, \mathbf{L}^p, \varphi, \boldsymbol{\xi}, \vartheta) = \boldsymbol{\Sigma}. \tag{2.74}$$

2.8 Isotropy

The following definitions help to make precise our notion of an isotropic (amorphous) material:

(i) Orth^+ = the group of all rotations (the proper orthogonal group);

(ii) the *symmetry group* $\mathcal{G}_{\mathrm{R}}$, is the group of all rotations of the *reference* configuration that leaves the response of the material unaltered.

(ii) the *symmetry group* $\mathcal{G}_{\mathrm{I}}$ at each time t, is the group of all rotations of the *intermediate* structural space that leaves the response of the material unaltered.

We now discuss the manner in which the basic fields transform under such transformations, granted the physically natural requirement of invariance of the internal power (2.62), or equivalently, the requirement that

$$\mathbf{S}^e : \dot{\mathbf{C}}^e \quad \text{and} \quad \mathbf{T}^p : \mathbf{L}^p \quad \text{be invariant.} \tag{2.75}$$

Let $\mathbf{Q}$ be a *time-independent rotation of the reference configuration.* Then $\mathbf{F} \to \mathbf{FQ}$, and hence

$$\mathbf{F}^p \to \mathbf{F}^p\mathbf{Q} \quad \text{and} \quad \mathbf{F}^e \text{ is invariant,} \tag{2.76}$$

so that, by (2.7) and (2.11), $\dot{\mathbf{C}}^e$ and $\mathbf{L}^p$ are invariant. We may therefore use (2.75) to conclude that $\mathbf{S}^e$ and $\mathbf{T}^p$ are invariant. Thus

- the constitutive equations (2.65) are unaffected by such rotations for the reference configuration.

Next, let $\mathbf{Q}$, a *time-independent rotation of the corresponding intermediate space*, be a symmetry transformation. Then $\mathbf{F}$ is unaltered by such a rotation, and hence

$$\mathbf{F}^e \to \mathbf{F}^e\mathbf{Q} \quad \text{and} \quad \mathbf{F}^p \to \mathbf{Q}^\top\mathbf{F}^p, \tag{2.77}$$

and also

$$\mathbf{C}^e \to \mathbf{Q}^\top\mathbf{C}^e\mathbf{Q}, \qquad \dot{\mathbf{C}}^e \to \mathbf{Q}^\top\dot{\mathbf{C}}^e\mathbf{Q}, \qquad \mathbf{L}^p \to \mathbf{Q}^\top\mathbf{L}^p\mathbf{Q}. \tag{2.78}$$

Then (2.78) and (2.75) yield the transformation laws

$$\mathbf{S}^e \to \mathbf{Q}^\top\mathbf{S}^e\mathbf{Q}, \qquad \mathbf{T}^p \to \mathbf{Q}^\top\mathbf{T}^p\mathbf{Q}. \tag{2.79}$$

Thus, with reference to the constitutive equations (2.65) we conclude that

$$\left.\begin{aligned} \bar{\psi}_{\mathrm{I}}(\mathbf{C}^e, \varphi, \vartheta) &= \bar{\psi}_{\mathrm{I}}(\mathbf{Q}^{\mathsf{T}}\mathbf{C}^e\mathbf{Q}, \varphi, \vartheta), \\ \mathbf{Q}^{\mathsf{T}}\bar{\mathbf{S}}^e(\mathbf{C}^e, \varphi, \vartheta)\mathbf{Q} &= \bar{\mathbf{S}}^e(\mathbf{Q}^{\mathsf{T}}\mathbf{C}^e\mathbf{Q}, \varphi, \vartheta), \\ \mathbf{Q}^{\mathsf{T}}\bar{\mathbf{T}}^p(\mathbf{L}^p, \varphi, \boldsymbol{\xi}, \vartheta)\mathbf{Q} &= \bar{\mathbf{T}}^p(\mathbf{Q}^{\mathsf{T}}\mathbf{L}^p\mathbf{Q}, \varphi, \boldsymbol{\xi}, \vartheta), \\ h_i(\mathbf{L}^p, \varphi, \boldsymbol{\xi}, \vartheta) &= h_i(\mathbf{Q}^{\mathsf{T}}\mathbf{L}^p\mathbf{Q}, \varphi, \boldsymbol{\xi}, \vartheta), \end{aligned}\right\} \tag{2.80}$$

must hold for all rotations $\mathbf{Q}$ in the *symmetry group* $\mathcal{G}_{\mathrm{I}}$ at each time t.

We refer to the material as *isotropic* (and to the reference configuration and intermediate spaces as undistorted) if

$$\mathcal{G}_{\mathrm{R}} = \mathrm{Orth}^+, \qquad \mathcal{G}_{\mathrm{I}} = \mathrm{Orth}^+, \tag{2.81}$$

so that the response of the material is invariant under arbitrary rotations of the reference and intermediate space at each time t. Henceforth

- *we restrict attention to materials that are* **isotropic**.

In this case,

- the response functions $\bar{\psi}_{\mathrm{I}}$, $\bar{\mathbf{S}}^e$, $\bar{\mathbf{T}}^p$, h_i, and $\mathbf{Y}^p$ must each be *isotropic*.

2.8.1 Consequences of isotropy of the elastic response

Since $\bar{\psi}_{\mathrm{I}}(\mathbf{C}^e, \varphi, \vartheta)$ is an isotropic function of $\mathbf{C}^e$, it has the representation

$$\bar{\psi}_{\mathrm{I}}(\mathbf{C}^e, \varphi, \vartheta) = \tilde{\psi}_{\mathrm{I}}(\mathcal{I}_{\mathbf{C}^e}, \varphi, \vartheta), \tag{2.82}$$

where

$$\mathcal{I}_{\mathbf{C}^e} = \Big(I_1(\mathbf{C}^e), I_2(\mathbf{C}^e), I_3(\mathbf{C}^e)\Big)$$

is the list of principal invariants of $\mathbf{C}^e$. The spectral representation of $\mathbf{C}^e$ is

$$\mathbf{C}^e = \sum_{i=1}^{3} \omega_i^e \mathbf{r}_i^e \otimes \mathbf{r}_i^e. \tag{2.83}$$

where $(\omega_1^e, \omega_2^e, \omega_3^e)$ are the positive eigenvalues, and $(\mathbf{r}_1^e, \mathbf{r}_2^e, \mathbf{r}_3^e)$ are the orthonormal eigenvectors of $\mathbf{C}^e$. Let

$$\lambda_i^e = \sqrt{\omega_i^e}, \tag{2.84}$$

denote the positive eigenvalues of $\mathbf{U}^e = \sqrt{\mathbf{C}^e}$. Then the principal invariants of $\mathbf{C}^e$ may be expressed as

$$\left.\begin{aligned} I_1(\mathbf{C}^e) &= \lambda_1^{e\,2} + \lambda_2^{e\,2} + \lambda_3^{e\,2}, \\ I_2(\mathbf{C}^e) &= \lambda_1^{e\,2}\lambda_2^{e\,2} + \lambda_2^{e\,2}\lambda_3^{e\,2} + \lambda_3^{e\,2}\lambda_1^{e\,2}, \\ I_3(\mathbf{C}^e) &= \lambda_1^{e\,2}\lambda_2^{e\,2}\lambda_3^{e\,2}; \end{aligned}\right\} \tag{2.85}$$

Using (2.85) in (2.82) to express the free energy in terms of the principal stretches, we obtain:

$$\begin{aligned}\psi_{\mathrm{I}} &= \tilde{\psi}_{\mathrm{I}}(\mathcal{I}_{\mathbf{C}^e}, \varphi, \vartheta) \\ &= \breve{\psi}_{\mathrm{I}}(\lambda_1^e, \lambda_2^e, \lambda_3^e, \varphi, \vartheta). \end{aligned} \tag{2.86}$$

Then, by the chain-rule and (2.69), the stress $\mathbf{S}^e$ is given by

$$\begin{aligned}\mathbf{S}^e &= 2\frac{\partial \breve{\psi}_{\mathrm{I}}(\lambda_1^e, \lambda_2^e, \lambda_3^e, \varphi, \vartheta)}{\partial \mathbf{C}^e} \\ &= 2\sum_{i=1}^{3} \frac{\partial \breve{\psi}_{\mathrm{I}}(\lambda_1^e, \lambda_2^e, \lambda_3^e, \varphi, \vartheta)}{\partial \lambda_i^e} \frac{\partial \lambda_i^e}{\partial \mathbf{C}^e} \\ &= \sum_{i=1}^{3} \frac{1}{\lambda_i^e} \frac{\partial \breve{\psi}_{\mathrm{I}}(\lambda_1^e, \lambda_2^e, \lambda_3^e, \varphi, \vartheta)}{\partial \lambda_i^e} \frac{\partial \omega_i^e}{\partial \mathbf{C}^e}. \end{aligned} \tag{2.87}$$

Assume that the squared principal stretches ω_i^e are distinct, so that the ω_i^e and the principal directions $\mathbf{r}_i^e$ may be considered as functions of $\mathbf{C}^e$. Then, from (2.83),

$$\frac{\partial \omega_i^e}{\partial \mathbf{C}^e} = \mathbf{r}_i^e \otimes \mathbf{r}_i^e, \tag{2.88}$$

and, granted this, (2.88) and (2.87) imply that

$$\mathbf{S}^e = \sum_{i=1}^{3} \frac{1}{\lambda_i^e} \frac{\partial \breve{\psi}_{\mathrm{I}}(\lambda_1^e, \lambda_2^e, \lambda_3^e, \varphi, \vartheta)}{\partial \lambda_i^e} \mathbf{r}_i^e \otimes \mathbf{r}_i^e. \tag{2.89}$$

Also, use of (2.83) and (2.89) in (2.46) gives

$$\mathbf{M}^e = \sum_{i=1}^{3} \lambda_i^e \frac{\partial \breve{\psi}_{\mathrm{I}}(\lambda_1^e, \lambda_2^e, \lambda_3^e, \varphi, \vartheta)}{\partial \lambda_i^e} \mathbf{r}_i^e \otimes \mathbf{r}_i^e. \tag{2.90}$$

Next, since

$$\mathbf{F}^e = \sum_{i=1}^{3} \lambda_i^e \mathbf{l}_i^e \otimes \mathbf{r}_i^e, \tag{2.91}$$

where

$$\mathbf{l}_i^e = \mathbf{R}^e \mathbf{r}_i^e,$$

are the eigenvectors of $\mathbf{V}^e$ (or $\mathbf{B}^e$), use of (2.45) and (2.89) gives

$$\mathbf{T} = J^{e-1} \Big(\sum_{i=1}^{3} \lambda_i^e \mathbf{l}_i^e \otimes \mathbf{r}_i^e \Big) \Big(\sum_{i=1}^{3} \frac{1}{\lambda_i^e} \frac{\partial \breve{\psi}_{\mathrm{I}}(\lambda_1^e, \lambda_2^e, \lambda_3^e, \varphi, \vartheta)}{\partial \lambda_i^e} \mathbf{r}_i^e \otimes \mathbf{r}_i^e \Big) \Big(\sum_{i=1}^{3} \lambda_i^e \mathbf{r}_i^e \otimes \mathbf{l}_i^e \Big),$$

or

$$\mathbf{T} = J^{e-1} \sum_{i=1}^{3} \lambda_i^e \frac{\partial \breve{\psi}_1(\lambda_1^e, \lambda_2^e, \lambda_3^e, \varphi, \vartheta)}{\partial \lambda_i^e} \mathbf{l}_i^e \otimes \mathbf{l}_i^e. \tag{2.92}$$

Further, (2.92) and (2.90) yield the important relation

$$\mathbf{M}^e = J^e \mathbf{R}^{e\mathsf{T}} \mathbf{T} \mathbf{R}^e. \tag{2.93}$$

and hence that

- *the Mandel stress* $\mathbf{M}^e$ *is* **symmetric**.

Furthermore, from (2.73), we recognize that the dissipative stress $\boldsymbol{\Sigma}$ is also symmetric.

2.9 Specialization of the constitutive equations

The constitutive equations listed in above are fairly general. With a view towards applications to amorphous metallic glasses, we specialize the theory by imposing additional constitutive assumptions based on experience with existing recent theories of isotropic viscoplasticity of metallic glasses.

2.9.1 Invertibility assumption for the flow rule

In classical theories of plasticity, the flow rule is usually specified as an equation for the plastic velocity gradient $\mathbf{L}^p$ in terms of a suitable stress measure and other internal variables. Accordingly, we assume that for a fixed state $(\mathbf{M}^e, \mathbf{C}^e, \varphi, \boldsymbol{\xi}, \vartheta)$, the dissipative flow stress function $\mathbf{Y}^p$ is invertible, so that we may write

$$\mathbf{L}^p = \bar{\mathbf{L}}^p(\boldsymbol{\Sigma}, \varphi, \boldsymbol{\xi}, \vartheta). \tag{2.94}$$

In this case, the dissipation inequality (2.70) may be written as

$$\boldsymbol{\Sigma} : \bar{\mathbf{L}}^p(\boldsymbol{\Sigma}, \varphi, \boldsymbol{\xi}, \vartheta) > 0 \qquad \text{for } \mathbf{L}^p \neq 0. \tag{2.95}$$

Since the function $\mathbf{Y}^p$ is isotropic, the function $\bar{\mathbf{L}}^p$ is also an isotropic function of its arguments.

2.9.2 Elastic energy and stress

Recall that $(\lambda_1^e, \lambda_2^e, \lambda_3^e)$ denote the principle stretches. Next, let

$$E_i^e \stackrel{\text{def}}{=} \ln \lambda_i^e \tag{2.96}$$

define *principal elastic logarithmic strains*, and consider a free energy function of the form

$$\breve{\psi}_{\mathrm{I}}(\lambda_1^e, \lambda_2^e, \lambda_3^e, \varphi, \vartheta) = \hat{\psi}_{\mathrm{I}}(E_1^e, E_2^e, E_3^e, \varphi, \vartheta) \tag{2.97}$$

so that, using (2.92)

$$\mathbf{T} = J^{e-1} \sum_{i=1}^{3} \frac{\partial \hat{\psi}_{\mathrm{I}}(E_1^e, E_2^e, E_3^e, \varphi, \vartheta)}{\partial E_i^e} \mathbf{l}_i^e \otimes \mathbf{l}_i^e. \tag{2.98}$$

We consider the following simple generalization of the classical strain energy function of infinitesimal isotropic elasticity which uses a logarithmic measure of finite strain,

$$\hat{\psi}_{\mathrm{I}}(E_1^e, E_2^e, E_3^e, \varphi, \vartheta) = G\left[(E_1^e)^2 + (E_2^e)^2 + (E_3^e)^2\right] + \tfrac{1}{2}\left(K - \tfrac{2}{3}G\right)\left(E_1^e + E_2^e + E_3^e\right)^2, \tag{2.99}$$

where the plastic volumetric strain-dependent and temperature-dependent parameters

$$G(\varphi, \vartheta) > 0, \quad K(\varphi, \vartheta) > 0, \tag{2.100}$$

are the shear modulus and bulk modulus, respectively.

Then, (2.98) gives

$$\mathbf{T} = J^{e-1} \left\{ \sum_{i=1}^{3} \left(2GE_i^e + \left(K - \frac{2}{3}G\right)\left(E_1^e + E_2^e + E_3^e\right) \right) \mathbf{l}_i^e \otimes \mathbf{l}_i^e \right\}. \tag{2.101}$$

Let

$$\mathbf{H}^e \stackrel{\text{def}}{=} \sum_{i=1}^{3} E_i^e \, \mathbf{l}_i^e \otimes \mathbf{l}_i^e, \tag{2.102}$$

denote the logarithmic elastic strain tensor in the deformed body, and

$$\mathbf{E}^e \stackrel{\text{def}}{=} \sum_{i=1}^{3} E_i^e \, \mathbf{r}_i^e \otimes \mathbf{r}_i^e, \tag{2.103}$$

denote the logarithmic elastic strain tensor in the intermediate space, so that

$$\mathbf{E}^e = \mathbf{R}^{e\mathsf{T}} \mathbf{H}^e \mathbf{R}^e. \tag{2.104}$$

Then, (2.101) gives

$$\mathbf{T} = J^{e-1} \left\{ 2G\mathbf{H}_0^e + K \operatorname{tr} \mathbf{H}^e \mathbf{1} \right\}. \tag{2.105}$$

Further, using (2.93) and (2.105), we find that the stress $\mathbf{M}^e$ is given by the simple relation

$$\mathbf{M}^e = 2G\mathbf{E}_0^e + K \operatorname{tr} \mathbf{E}^e \mathbf{1}. \tag{2.106}$$

Thus, summarizing, with

$$\mathbf{C}^e = \sum_{i=1}^{3} \omega_i^e \, \mathbf{r}_i^e \otimes \mathbf{r}_i^e, \tag{2.107}$$

the spectral representation of $\mathbf{C}^e$, and with

$$\mathbf{E}^e \stackrel{\text{def}}{=} \frac{1}{2} \ln \mathbf{C}^e \tag{2.108}$$

denoting a logarithmic strain measure, we consider an elastic free energy of the form:

$$\tilde{\psi}_{\text{I}}(\mathbf{E}^e, \varphi, \vartheta) = G|\mathbf{E}_0^e|^2 + \tfrac{1}{2}K(\text{tr}\,\mathbf{E}^e)^2, \tag{2.109}$$

where the plastic volumetric strain-dependent and temperature-dependent parameters

$$G(\varphi, \vartheta) > 0, \quad K(\varphi, \vartheta) > 0, \tag{2.110}$$

are the shear modulus and bulk modulus, respectively. In this case, the constitutive equation for the stress $\mathbf{M}^e$ becomes

$$\mathbf{M}^e = 2G\mathbf{E}_0^e + K\text{tr}\mathbf{E}^e\mathbf{1}\,, \tag{2.111}$$

and the corresponding Cauchy stress, using (2.93), is

$$\mathbf{T} = J^{e-1}\mathbf{R}^e\mathbf{M}^e\mathbf{R}^{e\top}. \tag{2.112}$$

2.9.3 Kinematical hypothesis for plastic velocity gradient. Internal variables

We assume that plastic flow occurs by shearing accompanied by dilatation (or compaction) relative to some slip systems. Each slip system is specified by a slip direction $\mathbf{s}^{(\alpha)}$, and a slip plane normal $\mathbf{m}^{(\alpha)}$ (we label slip systems by integers α), with

$$\mathbf{s}^{(\alpha)} \cdot \mathbf{m}^{(\alpha)} = 0, \qquad |\mathbf{s}^{(\alpha)}|, \; |\mathbf{m}^{(\alpha)}| = 1, \tag{2.113}$$

and we take the plastic stretching to be made up of shearing rates $\nu^{(\alpha)}$ on the set of potential slip systems, and assume that this shearing is accompanied by *shear-induced dilatation* rates $\delta^{(\alpha)}$ in the directions normal to the shear directions. That is, the total plastic velocity gradient is taken as

$$\left.\begin{aligned} &\mathbf{L}^p = \sum_{\alpha} \mathbf{L}^{p(\alpha)}, \\ &\mathbf{L}^{p(\alpha)} = \nu^{(\alpha)}(\mathbf{s}^{(\alpha)} \otimes \mathbf{m}^{(\alpha)}) + \delta^{(\alpha)}(\mathbf{m}^{(\alpha)} \otimes \mathbf{m}^{(\alpha)}), \qquad \nu^{(\alpha)} \geq 0, \\ &\delta^{(\alpha)} = \beta\,\nu^{(\alpha)}, \end{aligned}\right\} \tag{2.114}$$

where β is a *dilatancy function.* Positive values of β describe plastically dilatant behavior, while $\beta < 0$ describes behavior that is plastically compacting.

For an amorphous isotropic material there are no preferred directions other than the principal directions of stress, and accordingly we consider potential slip systems with respect to these principal directions of stress. The symmetric stress $\mathbf{\Sigma}$ has the spectral representation

$$\mathbf{\Sigma} = \sum_{i=1}^{3} \sigma_i \, \hat{\mathbf{e}}_i \otimes \hat{\mathbf{e}}_i, \tag{2.115}$$

where $\{\sigma_i | i = 1, 2, 3\}$ are the principal values, and $\{\hat{\mathbf{e}}_i | i = 1, 2, 3\}$ are the orthonormal principal directions of $\mathbf{\Sigma}$. We assume that the principal stresses $\{\sigma_i | i = 1, 2, 3\}$ are strictly ordered such that

$$\sigma_1 \geq \sigma_2 \geq \sigma_3. \tag{2.116}$$

First, consider potential slip in the $(\hat{\mathbf{e}}_1, \hat{\mathbf{e}}_3)$-plane. Let $\left(\mathbf{s}^{(\alpha)}, \mathbf{m}^{(\alpha)}\right)$ denote a potential slip system lying in this plane and oriented such that $\mathbf{s}^{(\alpha)}$ makes an angle ξ with respect to the $\hat{\mathbf{e}}_1$-axis

$$\mathbf{s}^{(\alpha)} = \cos\xi \hat{\mathbf{e}}_1 + \sin\xi \hat{\mathbf{e}}_3, \qquad \mathbf{m}^{(\alpha)} = \sin\xi \hat{\mathbf{e}}_1 - \cos\xi \hat{\mathbf{e}}_3,$$

and let

$$\tau^{(\alpha)}(\xi) = \mathbf{s}^{(\alpha)} \cdot \mathbf{\Sigma}\mathbf{m}^{(\alpha)}, \qquad \text{and} \qquad \sigma^{(\alpha)}(\xi) = -\mathbf{m}^{(\alpha)} \cdot \mathbf{\Sigma}\mathbf{m}^{(\alpha)},$$

denote the resolved shear stress and compressive normal traction for such a system. Then, introducing an internal variable $\mu \geq 0$ called the *internal friction coefficient*, we define the quantity

$$\varpi \stackrel{\text{def}}{=} \arctan\mu \tag{2.117}$$

called the *angle of internal friction*, and assume that any given instant for a fixed stress $\mathbf{\Sigma}$, shearing is possible only on those slip systems for which

$$f(\xi) = \{\tau(\xi) - (\tan\varpi)\,\sigma(\xi)\},$$

is a *maximum* with respect to ξ. It is easily shown that $f(\xi)$ is a maximum for

$$\xi = \pm\left\{\frac{\pi}{4} + \frac{\varpi}{2}\right\}. \tag{2.118}$$

Hence, there are two potential slip systems in the $(\hat{\mathbf{e}}_1, \hat{\mathbf{e}}_3)$-plane, with slip directions which are symmetrically disposed about the maximum principal stress direction:

$$\left.\begin{aligned} \mathbf{s}^{(1)} &= \cos\xi \hat{\mathbf{e}}_1 + \sin\xi \hat{\mathbf{e}}_3, \quad \mathbf{m}^{(1)} = \sin\xi \hat{\mathbf{e}}_1 - \cos\xi \hat{\mathbf{e}}_3, \\ \mathbf{s}^{(2)} &= \cos\xi \hat{\mathbf{e}}_1 - \sin\xi \hat{\mathbf{e}}_3, \quad \mathbf{m}^{(2)} = \sin\xi \hat{\mathbf{e}}_1 + \cos\xi \hat{\mathbf{e}}_3, \end{aligned}\right\} \tag{2.119}$$

with

$$\xi = (\pi/4) + (\varpi/2). \tag{2.120}$$

In an entirely analogous manner, the slip systems in the $(\hat{\mathbf{e}}_1, \hat{\mathbf{e}}_2)$-plane are

$$\left.\begin{aligned} \mathbf{s}^{(3)} &= \cos\xi\hat{\mathbf{e}}_1 + \sin\xi\hat{\mathbf{e}}_2, \quad \mathbf{m}^{(3)} = \sin\xi\hat{\mathbf{e}}_1 - \cos\xi\hat{\mathbf{e}}_2, \\ \mathbf{s}^{(4)} &= \cos\xi\hat{\mathbf{e}}_1 - \sin\xi\hat{\mathbf{e}}_2, \quad \mathbf{m}^{(4)} = \sin\xi\hat{\mathbf{e}}_1 + \cos\xi\hat{\mathbf{e}}_2, \end{aligned}\right\} \tag{2.121}$$

while those in the $(\hat{\mathbf{e}}_2, \hat{\mathbf{e}}_3)$-plane are

$$\left.\begin{aligned} \mathbf{s}^{(5)} &= \cos\xi\hat{\mathbf{e}}_2 + \sin\xi\hat{\mathbf{e}}_3, \quad \mathbf{m}^{(5)} = \sin\xi\hat{\mathbf{e}}_2 - \cos\xi\hat{\mathbf{e}}_3, \\ \mathbf{s}^{(6)} &= \cos\xi\hat{\mathbf{e}}_2 - \sin\xi\hat{\mathbf{e}}_3, \quad \mathbf{m}^{(6)} = \sin\xi\hat{\mathbf{e}}_2 + \cos\xi\hat{\mathbf{e}}_3. \end{aligned}\right\} \tag{2.122}$$

Thus, the total plastic stretching is made up of contributions from shearing on each of the six potential slip systems:

$$\mathbf{L}^p = \sum_{\alpha=1}^{6} \nu^{(\alpha)} \left\{ (\mathbf{s}^{(\alpha)} \otimes \mathbf{m}^{(\alpha)}) + \beta \mathbf{m}^{(\alpha)} \otimes \mathbf{m}^{(\alpha)} \right\}. \tag{2.123}$$

The corresponding shearing rates $\nu^{(\alpha)}$ are given by a flow function

$$\nu^{(\alpha)} = \hat{\nu}^{(\alpha)}(\tau^{(\alpha)}, \sigma^{(\alpha)}, \vartheta, S, \mu, \varphi) \geq 0, \tag{2.124}$$

where S is a stress-dimensioned internal variable which represents a transient *resistance* to plastic flow (accompanying the microstructural disordering), assumed for an isotropic material to be the same for all slip systems.

It is convenient to write Λ for the list of variables

$$\Lambda = (\boldsymbol{\Sigma}, \vartheta, S, \mu, \varphi).$$

Using this notation, we assume that the dilatancy parameter β depends on Λ,

$$\beta = \hat{\beta}(\Lambda). \tag{2.125}$$

With $\mathbf{L}^p$ given by (2.123) , the dissipation inequality requires that

$$\boldsymbol{\Sigma} : \mathbf{L}^p = \sum_{\alpha=1}^{6} \left[\tau^{(\alpha)} - \beta\, \sigma^{(\alpha)}\right] \nu^{(\alpha)} > 0 \tag{2.126}$$

whenever plastic flow occurs. We assume that the material is *strongly dissipative* in the sense that

$$\left[\tau^{(\alpha)} - \beta\, \sigma^{(\alpha)}\right] \nu^{(\alpha)} > 0 \qquad \text{for each } \alpha\,. \tag{2.127}$$

Thus, whenever $\nu^{(\alpha)} > 0$, we must have

$$\left[\tau^{(\alpha)} - \beta\, \sigma^{(\alpha)}\right] > 0, \tag{2.128}$$

which is a thermodynamic restriction that the dilatancy function $\beta = \hat{\beta}(\Lambda)$ must satisfy.

We emphasize that we do not assume that $\mu = \beta$, which (using classical terminology) would correspond to an *associated/normality flow rule.*

Straight-forward calculations show that the resolved shear stresses and compressive normal tractions on the slip systems are given by

$$\left.\begin{aligned} \tau^{(1,2)} &= \tfrac{1}{2}\sin(2\xi)(\sigma_1-\sigma_3), \quad \sigma^{(1,2)} &&= -\tfrac{1}{2}(\sigma_1+\sigma_3)+\tfrac{1}{2}\cos(2\xi)(\sigma_1-\sigma_3),\\ \tau^{(3,4)} &= \tfrac{1}{2}\sin(2\xi)(\sigma_1-\sigma_2), \quad \sigma^{(3,4)} &&= -\tfrac{1}{2}(\sigma_1+\sigma_2)+\tfrac{1}{2}\cos(2\xi)(\sigma_1-\sigma_2),\\ \tau^{(5,6)} &= \tfrac{1}{2}\sin(2\xi)(\sigma_2-\sigma_3), \quad \sigma^{(5,6)} &&= -\tfrac{1}{2}(\sigma_2+\sigma_3)+\tfrac{1}{2}\cos(2\xi)(\sigma_2-\sigma_3). \end{aligned}\right\} \tag{2.129}$$

Thus, from (2.124) we note that in the case of distinct principal stresses

$$\nu^{(1)} = \nu^{(2)}, \qquad \nu^{(3)} = \nu^{(4)}, \qquad \nu^{(5)} = \nu^{(6)}, \quad \text{if} \quad \sigma_1 > \sigma_2 > \sigma_3, \tag{2.130}$$

and in situations when the principal stresses are not distinct we have

$$\nu^{(1)} = \nu^{(2)} = \nu^{(3)} = \nu^{(4)}, \qquad \nu^{(5)} = \nu^{(6)} = 0 \quad \text{if} \quad \sigma_1 > \sigma_2 = \sigma_3, \tag{2.131}$$

$$\nu^{(1)} = \nu^{(2)} = \nu^{(5)} = \nu^{(6)}, \qquad \nu^{(3)} = \nu^{(4)} = 0, \quad \text{if} \quad \sigma_1 = \sigma_2 > \sigma_3\,, \tag{2.132}$$

and

$$\nu^{(1)} = \nu^{(2)} = \nu^{(3)} = \nu^{(4)} = \nu^{(5)} = \nu^{(6)} = 0 \quad \text{if} \quad \sigma_1 = \sigma_2 = \sigma_3\,. \tag{2.133}$$

Remark 1: When $\sigma_1 > \sigma_2 = \sigma_3$, $\hat{\mathbf{e}}_2$ and $\hat{\mathbf{e}}_3$ are *any two* orthonormal vectors perpendicular to $\hat{\mathbf{e}}_1$, and we have an *infinite number of potential slip systems with slip directions* $\mathbf{s}^{(\alpha)}$ *lying on a cone with axis* $\hat{\mathbf{e}}_1$ *and a semi-angle* $\xi = \{(\pi/4)+(\varpi/2)\}$. In enumerating our slip systems we choose *an arbitrary pair* of orthonormal vectors $(\hat{\mathbf{e}}_2, \hat{\mathbf{e}}_3)$ perpendicular to $\hat{\mathbf{e}}_1$; this choice, and therefore the choice of slip systems is clearly non-unique. A similar remark concerning a non-unique choice of slip systems holds when $\sigma_1 = \sigma_2 > \sigma_3$.

Remark 2: On account of (2.130), (2.131), (2.132), we can demonstrate that the plastic spin indeed does vanish, $\mathbf{W}^p = \mathbf{0}$.

2.9.4 Evolution equations for internal variables. Dilatancy equation

The internal variables $\boldsymbol{\xi}$ of the model are the resistance S and the internal friction $\mu = \tan\varpi$, for which we need to prescribe evolution equations, and we also need to specify a constitutive equation for the dilatancy function β, which determines the evolution of the volumetric plastic strain φ.

Recall from (2.14) that $\varphi = \varphi_0 + \ln J^p$, and therefore $\dot{\varphi} = \mathrm{tr}\mathbf{L}^p$. Thus using (2.123) we have that

$$\dot{\varphi} = \beta\,\nu^p, \tag{2.134}$$

where

$$\nu^p \stackrel{\text{def}}{=} \sum_{\alpha} \nu^{(\alpha)} \tag{2.135}$$

is the sum of the shearing rate on all the slip systems.

Furthermore, we assume that the evolution of the internal variables, S and μ, is given by a set of coupled differential equations:

$$\left.\begin{aligned} \dot{S} &= h(\Lambda, \nu^p) \\ \dot{\mu} &= g(\Lambda, \nu^p) \end{aligned}\right\}, \tag{2.136}$$

2.10 Summary of the specialized constitutive model

In this section, we summarize the specialized form of our theory. The underlying constitutive equations relate the following basic fields:

$\mathbf{x} = \boldsymbol{\chi}(\mathbf{X}, t)$,	motion;
$\mathbf{F} = \nabla\boldsymbol{\chi}, \quad J = \det\mathbf{F} > 0$,	deformation gradient;
$\mathbf{F} = \mathbf{F}^e\mathbf{F}^p$,	elastic-plastic decomposition of $\mathbf{F}$;
$\mathbf{F}^p, \quad J^p = \det\mathbf{F}^p > 0$,	inelastic distortion;
$\mathbf{F}^e, \quad J^e = \det\mathbf{F}^e > 0$,	elastic distortion;
$\mathbf{F}^e = \mathbf{R}^e\mathbf{U}^e = \mathbf{V}^e\mathbf{R}^e$,	polar decomposition of $\mathbf{F}^e$;
$\mathbf{U}^e = \sum_{\alpha=1}^{3} \lambda_\alpha^e \mathbf{r}_\alpha^e \otimes \mathbf{r}_\alpha^e$,	spectral decomposition of $\mathbf{U}^e$,
$\mathbf{E}^e = \sum_{\alpha=1}^{3} (\ln\lambda_\alpha^e)\mathbf{r}_\alpha^e \otimes \mathbf{r}_\alpha^e$,	logarithmic elastic strain,
$\varphi = \varphi_0 + \ln J^p$,	plastic volumetric strain;
$\mathbf{T}, \quad \mathbf{T} = \mathbf{T}^\top$,	Cauchy stress;
$\mathbf{M}^e = \mathbf{R}^{e\top}(J^e\mathbf{T})\mathbf{R}^e$,	stress conjugate to elastic strain, $\mathbf{E}^e$;
$\vartheta > 0$,	absolute temperature;
ψ_{I},	free energy density per unit intermediate volume;
S,	flow resistance;
$\mu \geq 0$,	internal friction coefficient;
$\varpi = \arctan\mu$,	internal friction angle;
β,	dilatancy parameter;

The set of constitutive equations are summarized below:

1. **Free energy**:

$$\tilde{\psi}_{\mathrm{I}}(\mathbf{E}^e, \varphi, \vartheta) = G|\mathbf{E}_0^e|^2 + \tfrac{1}{2}K(\mathrm{tr}\,\mathbf{E}^e)^2, \tag{2.137}$$

with

$$G = \hat{G}(\varphi, \vartheta) > 0, \quad K = \hat{K}(\varphi, \vartheta) > 0, \tag{2.138}$$

the elastic shear modulus and bulk modulus.

2. **Equation for the stress**: The Cauchy stress is given by

$$\mathbf{T} \overset{\text{def}}{=} J^{e-1}\left(\mathbf{R}^e\mathbf{M}^e\mathbf{R}^{e\top}\right), \tag{2.139}$$

where

$$\mathbf{M}^e = \frac{\partial\psi(\mathbf{E}^e, \vartheta)}{\partial\mathbf{E}^e} = 2G\mathbf{E}_0^e + K(\mathrm{tr}\,\mathbf{E}^e)\mathbf{1}\,. \tag{2.140}$$

3. **Dissipative stress**: The thermodynamically-consistent driving stress for plastic flow $\boldsymbol{\Sigma}$ is given by

$$\boldsymbol{\Sigma} \stackrel{\text{def}}{=} \mathbf{M}^e - \Big(\tilde{\psi}(\mathbf{E}^e, \varphi, \vartheta) + \frac{\partial \tilde{\psi}(\mathbf{E}^e, \varphi, \vartheta)}{\partial \varphi}\Big)\mathbf{1}. \tag{2.141}$$

The symmetric stress tensor $\boldsymbol{\Sigma}$ has the spectral representation

$$\boldsymbol{\Sigma} = \sum_{i=1}^{3} \sigma_i \, \hat{\mathbf{e}}_i \otimes \hat{\mathbf{e}}_i, \tag{2.142}$$

where $\{\sigma_i | i = 1, 2, 3\}$ are the principal values, and $\{\hat{\mathbf{e}}_i | i = 1, 2, 3\}$ the corresponding orthonormal principal directions. We assume that the principal stresses $\{\sigma_i | i = 1, 2, 3\}$ are strictly ordered such that

$$\sigma_1 \geq \sigma_2 \geq \sigma_3. \tag{2.143}$$

4. **Slip systems, resolved shear stress, and compressive normal traction:** We assume that plastic flow occurs by shearing accompanied by dilatation relative to some slip systems. Slip systems are labeled by integers α; each slip system is specified by a slip direction $\mathbf{s}^\alpha$, and a slip plane normal $\mathbf{m}^\alpha$ with

$$\mathbf{s}^{(\alpha)} \cdot \mathbf{m}^{(\alpha)} = 0, \qquad |\mathbf{s}^{(\alpha)}|, \; |\mathbf{m}^{(\alpha)}| = 1. \tag{2.144}$$

As discussed previously, for an amorphous isotropic material there are no preferred directions other than the principal directions of stress, and accordingly we consider plastic flow to be possible on six potential slip systems defined relative to the principal directions of stress $\boldsymbol{\Sigma}$:

$$\left.\begin{aligned}
\mathbf{s}^{(1)} &= \cos\xi\hat{\mathbf{e}}_1 + \sin\xi\hat{\mathbf{e}}_3, & \mathbf{m}^{(1)} &= \sin\xi\hat{\mathbf{e}}_1 - \cos\xi\hat{\mathbf{e}}_3, \\
\mathbf{s}^{(2)} &= \cos\xi\hat{\mathbf{e}}_1 - \sin\xi\hat{\mathbf{e}}_3, & \mathbf{m}^{(2)} &= \sin\xi\hat{\mathbf{e}}_1 + \cos\xi\hat{\mathbf{e}}_3, \\
\mathbf{s}^{(3)} &= \cos\xi\hat{\mathbf{e}}_1 + \sin\xi\hat{\mathbf{e}}_2, & \mathbf{m}^{(3)} &= \sin\xi\hat{\mathbf{e}}_1 - \cos\xi\hat{\mathbf{e}}_2, \\
\mathbf{s}^{(4)} &= \cos\xi\hat{\mathbf{e}}_1 - \sin\xi\hat{\mathbf{e}}_2, & \mathbf{m}^{(4)} &= \sin\xi\hat{\mathbf{e}}_1 + \cos\xi\hat{\mathbf{e}}_2, \\
\mathbf{s}^{(5)} &= \cos\xi\hat{\mathbf{e}}_2 + \sin\xi\hat{\mathbf{e}}_3, & \mathbf{m}^{(5)} &= \sin\xi\hat{\mathbf{e}}_2 - \cos\xi\hat{\mathbf{e}}_3, \\
\mathbf{s}^{(6)} &= \cos\xi\hat{\mathbf{e}}_2 - \sin\xi\hat{\mathbf{e}}_3, & \mathbf{m}^{(6)} &= \sin\xi\hat{\mathbf{e}}_2^e + \cos\xi\hat{\mathbf{e}}_3.
\end{aligned}\right\} \tag{2.145}$$

where

$$\xi = \frac{\pi}{4} + \frac{\varpi}{2}. \tag{2.146}$$

and

$$\varpi \stackrel{\text{def}}{=} \arctan\mu \tag{2.147}$$

is an *angle of internal friction*, and $\mu \geq 0$ is a *friction coefficient.*

The resolved shear and compressive normal traction on each slip system are given by

$$\tau^{(\alpha)} \stackrel{\text{def}}{=} \mathbf{s}^{(\alpha)} \cdot \boldsymbol{\Sigma}\mathbf{m}^{(\alpha)}, \qquad \sigma^{(\alpha)} \stackrel{\text{def}}{=} -\mathbf{m}^{(\alpha)} \cdot \boldsymbol{\Sigma}\mathbf{m}^{(\alpha)}. \tag{2.148}$$

5. **Flow rule**: The evolution equation for $\mathbf{F}^p$ is

$$\dot{\mathbf{F}}^p = \mathbf{L}^p \mathbf{F}^p, \qquad \mathbf{F}^p(\mathbf{X}, 0) = \mathbf{1}, \tag{2.149}$$

with $\mathbf{L}^p$ given by

$$\mathbf{L}^p = \sum_{\alpha=1}^{6} \nu^{(\alpha)} \left[\mathbf{s}^{(\alpha)} \otimes \mathbf{m}^{(\alpha)} + \beta\, \mathbf{m}^{(\alpha)} \otimes \mathbf{m}^{(\alpha)}\right]. \tag{2.150}$$

The constitutive equation for the shearing rates $\nu^{(\alpha)}$ is taken as

$$\nu^{(\alpha)} = \hat{\nu}^{(\alpha)}(\tau^{(\alpha)}, \sigma^{(\alpha)}, \vartheta, S, \mu, \varphi) \geq 0, \tag{2.151}$$

where S is a positive-valued, stress-dimensioned internal variable which represents a transient *resistance* to plastic flow (accompanying the microstructural disordering), assumed for an isotropic material to be the same for all slip systems.

The quantity β is a *shear-induced plastic dilatancy function.* Positive values of β describe plastically dilatant behavior, while $\beta < 0$ describes behavior that is plastically compacting. It is convenient to write Λ for the list of variables

$$\Lambda = (\boldsymbol{\Sigma}, \vartheta, S, \mu, \varphi).$$

Using this notation, we assume that the dilatancy parameter β depends on Λ,

$$\beta = \hat{\beta}(\Lambda). \tag{2.152}$$

The dissipation inequality (2.126) requires that

$$\boldsymbol{\Sigma} : \mathbf{L}^p = \sum_{\alpha=1}^{6} \left[\tau^{(\alpha)} - \beta\, \sigma^{(\alpha)}\right] \nu^{(\alpha)} > 0 \tag{2.153}$$

whenever plastic flow occurs. We require that

$$\left[\tau^{(\alpha)} - \beta\, \sigma^{(\alpha)}\right] \nu^{(\alpha)} > 0 \qquad \text{for each } \alpha\,; \tag{2.154}$$

thus, whenever $\nu^{(\alpha)} > 0$, we must have

$$\left[\tau^{(\alpha)} - \beta\, \sigma^{(\alpha)}\right] > 0. \tag{2.155}$$

This is a restriction that the dilatancy function β must satisfy.

We emphasize that we do not assume that $\mu = \beta$, which would correspond to an *associated/normality flow rule.*

6. **Evolution equations for φ, S and μ**: The evolution of the plastic volumetric strain is given by

$$\dot{\varphi} = \beta\, \nu^p, \qquad \varphi(\mathbf{X}, 0) = \varphi_0, \tag{2.156}$$

where

$$\nu^p \stackrel{\text{def}}{=} \sum_{\alpha=1}^{6} \nu^{(\alpha)}.$$

Furthermore, we assume that the evolution of the internal variables, S and μ, is given by a set of coupled differential equations:

$$\left.\begin{aligned} \dot{S} &= h(\Lambda, \nu^p) \\ \dot{\mu} &= g(\Lambda, \nu^p) \end{aligned}\right\}. \tag{2.157}$$

These evolution equations are accompanied by the appropriate initial conditions

$$S(\mathbf{X}, 0) = S_0, \qquad \mu(\mathbf{X}, 0) = \mu_0. \tag{2.158}$$

Bibliography

[1] L. Anand and C. Su. A theory for amorphous viscoplastic materials undergoing finite deformations, with application to metallic glasses. *Journal of Mechanics and Physics of Solids*, 53:1362–1396, 2005.

[2] C. Su and L. Anand. Plane strain indentation of a Zr-based metallic glass: Experiments and numerical simulation. *Acta Materialia*, 54:179–189, 2006.

[3] L. Anand and C. Su. A constitutive theory for metallic glasses at high homologous temperatures. *Acta Materialia*, 55, 2007.

[4] E. Kröner. Allgemeine kontinuumstheorie der versetzungen und eigenspannungen. *Archive for Rational Mechanics and Analysis*, 4:273–334, 1960.

[5] E. H. Lee. Elastic plastic deformation at finite strain. *AMSE Journal of Applied Mechanics*, 36:1–6, 1969.

[6] Q. Yang, A. Mota, and M. Ortiz. A finite deformation constitutive model of bulk metallic glass plasticity. *Computational Mechanics*, 37:194–204, 2006.

[7] P. Thamburaja and R. Ekambaram. Coupled thermo-mechanical modelling of bulk-metallic glasses: Theory, finite-element simulations and experimental verification. *Journal of the Mechanics and Physics of Solids*, 55:1236–1273, 2007.

[8] M. E. Gurtin. A gradient theory of single-crystal viscoplasticity that accounts for geometrically necessary dislocations. *Journal of the Mechanics and Physics of Solids*, 50: 5–32, 2002. doi: 10.1016/S0022-5096(01)00104-1.

[9] L. Anand and M. E. Gurtin. A theory of amorphous solids undergoing large deformations, with applications to polymeric glasses. *International Journal of Solids and Structures*, 40:1465–1487, 2003.

[10] M. E. Gurtin and L. Anand. The decomposition $\mathbf{F} = \mathbf{F}^e\mathbf{F}^p$, material symmetry, and plastic irrotationality for solids that are isotropic-viscoplastic or amorphous. *International Journal of Plasticity*, 21:1686–1719, 2005. doi: 10.1016/j.ijplas.2004.11.007.

Chapter 3

Application to amorphous metals at high temperatures spanning the glass transition temperature

3.1 Introduction

The constitutive theory outlined in the previous chapter is fairly general. In this chapter, we specialize this theory to model the elastic-viscoplastic response of metallic glasses in the temperature range $0.9\vartheta_g \lesssim \vartheta \lesssim \vartheta_x$.

3.2 Internal Friction

Since there is not enough experimental information concerning the pressure-sensitivity of plastic flow of metallic glasses at high homologous temperatures, and since the pressure-sensitivity is expected to be small, from the outset we set the internal friction coefficient $\mu = 0$. In setting the internal friction to be zero, the Coulomb-type theory of Anand and Su reduces to a Tresca-type theory.

3.3 Scalar flow function. Evolution of the internal variables.

Next, we discuss the specialization of the important scalar flow rate equation (2.124). To do this, we first review some physical aspects of the inelastic deformation of metallic glasses, and also recall the classical one-dimensional model of Spaepen (1977) which is often used to represent the macroscopic inelastic response of metallic glasses.

3.3.1 Physical Background

The micro-mechanisms of inelastic deformation in bulk metallic glasses are not related to dislocation-based mechanisms that characterize the plastic deformation of crystalline metals. The plastic deformation of amorphous metallic glasses is fundamentally different from that in crystalline solids because of the lack of long-range order in the atomic structure of these materials. The underlying atomistic mechanisms of the inelastic deformation of metallic glasses have been under intense investigation for the past three decades, and are still not completely understood [cf., e.g., 1–7]. However, atomistic simulations reported in the literature [cf., e.g., 8–12] show that at a micromechanical level, inelastic deformation in metallic glasses occurs by local shearing of clusters of atoms ($\approx$ 30-100 atoms), this shearing is accompanied by deformation-induced *microstructural disordering* and *inelastic dilatation* that produces *strain-softening*, which at low homologous temperatures leads to the formation of intense shear bands.

Deformation-induced microstructural disordering in a metallic glass also occurs in the high temperature range. A macroscopic manifestation of the structural disordering in this temperature range is that in strain-controlled isothermal compression or tension experiments at constant strain rate, the microstructural disordering leads to strain-softening. However, because of the high strain rate sensitivity of the material at elevated temperatures, it does not exhibit macroscopic localized shear bands and the deformation appears as *nominally homogeneous*. Experimental examples of such macroscopic response may be found in de Hey et al. [6] for the amorphous metal $Pd_{40}Ni_{40}P_{20}$, and in Lu et al. [2] for the commercial Zr-based alloy Vitreloy-1.

3.3.2 The Spaepen model

A continuum-level one-dimensional model which has long been used to represent the inelastic response of metallic glasses is the *free volume model* proposed by Spaepen [1], and it is this model that was used by de Hey et al. [6] to analyze their experimental results. Briefly, let $|\dot{\epsilon}^p|$ denote the magnitude of the plastic strain rate in a *one-dimensional* setting. In such a setting, the flow equation proposed by Spaepen has the form

$$|\dot{\epsilon}^p| = 2\, c_f\, k_f \frac{\epsilon_0 v_0}{\Omega} \sinh\Big(\frac{|\sigma|\, \epsilon_0\, v_0}{2\, k_B\, \vartheta}\Big). \tag{3.1}$$

Here $|\sigma|$ is the absolute value of the stress, ϵ_0 is a local transformation strain, v_0 is an activation volume, Ω is an atomic volume, k_f is a temperature dependent rate factor, k_B is Boltzmann's constant, and

$$c_f = \exp\Big(-\frac{1}{\zeta}\Big) \equiv \exp\Big(-\frac{\gamma\, v^*}{v_f}\Big) \tag{3.2}$$

is the concentration of flow defects defined in terms of a normalized free volume parameter $\zeta = v_f/(\gamma\, v^*)$, where v_f is the average free volume per atom, v^* is a critical value of the free

volume, and γ is a geometrical overlap factor with a value between 0.5 and 1. In de Hey et al. [6], the evolution of the defect concentration is taken as[1]

$$\dot{c}_f = \underbrace{\left(a_\zeta\, c_f\, (\ln c_f)^2\right) |\dot{\epsilon}^p|}_{\text{dynamic defect creation}} - \underbrace{k_r\, c_f\, (c_f - c_{f,eq})}_{\text{static thermal recovery}}, \tag{3.3}$$

with a_ζ a temperature dependent parameter, k_r a temperature dependent rate factor, and

$$c_{f,eq} = \exp(-\frac{1}{\zeta_{eq}}), \tag{3.4}$$

where

$$\zeta_{eq} = \frac{\vartheta - \vartheta_0}{B} \tag{3.5}$$

is the value of the free volume in thermal equilibrium at a temperature ϑ; here ϑ_0 and B are two material constants known as the Vogel-Fulcher-Tamann (VFT) parameters.

A study of the paper by de Hey et al. [6] reveals that the flow equation (3.1) and the evolution equation (3.3), when suitably calibrated, are *not able to produce stress-strain curves that match their corresponding experimental stress-strain data* which show the phenomena of stress-overshoot and strain-softening in monotonic experiments at a given strain rate, and strain rate history effects in experiments involving strain rate increments and decrements.

In our opinion, even though the flow and evolution equations (3.1) and (3.3) are physically reasonably well-motivated, they leave out some important *coupling effects* and thereby are unable to quantitatively reproduce the stress-overshoot and strain-softening phenomenon which arise in a metallic glass due to deformation-induced microstructural disordering. In what follows, we propose suitable simple phenomenological modifications to the Spaepen model in order to provide additional flexibility to reproduce the experimentally-observed stress-strain response of metallic glasses in the temperature range $0.9\vartheta_g \lesssim \vartheta \lesssim \vartheta_x$.

3.3.3 Modified Spaepen model

We begin by using the plastic volumetric strain φ and the internal variable S to modify Spaepen's flow equation to better reproduce the stress-overshoot and strain-softening phenomena due to deformation-induced disordering. In our macroscopic theory, we associate the widely observed deformation-induced microstructural disordering of a metallic glass with the plastic volumetric strain φ. Thus, throughout, we will refer to φ as an "order-parameter." The internal variable S is a stress-dimensioned parameter representing a transient change in resistance to plastic flow accompanying the microstructural disordering. Guided by (3.1)

[1] In Spaepen's original model [1], the evolution of the defect concentration is also controlled by diffusional mechanisms. However, the effects of diffusion of free volume at nominal strain rates $\gtrsim 10^{-5}\text{s}^{-1}$ and moderate strain levels is expected to be small, and is accordingly not considered here.

and (3.2), the flow function for the scalar shearing rate on each slip system is taken as

$$\nu^{(\alpha)} = \nu_0 \exp\left(-\frac{1}{\zeta}\right) \exp\left(-\frac{\Delta F}{k_B \vartheta}\right) \sinh\left(\frac{\tau_{\text{eff}}^{(\alpha)} V}{2 k_B \vartheta}\right), \tag{3.6}$$

with ν_0 a pre-exponential factor of the order of the Debye frequency, ζ a free volume parameter as in Spaepen's theory, ΔF an activation energy, $V \equiv (\epsilon_0 v_0)$ an activation volume, and

$$\tau_{\text{eff}}^{(\alpha)} \stackrel{\text{def}}{=} \tau^{(\alpha)} - S \tag{3.7}$$

an *effective stress*, where S is the transient change in flow resistance accompanying the microstructural disordering of the material. The scalar flow rate $\nu^{(\alpha)}$ is positive whenever $\tau_{\text{eff}}^{(\alpha)} > 0$, and is zero otherwise.

The evolution equation for the resistance S is *coupled* with the evolution equation for φ, and it is this coupling which is used to model the yield-peak observed in stress-strain response of metallic glasses.[2] Specifically we take the evolution of S to be governed by

$$\left.\begin{aligned} &\dot{S} = h\,\nu^p, \qquad \text{with initial value} \qquad S(\mathbf{X}, 0) = S_0\,, \\ &h = h_0\,(S^* - S)\,, \qquad \text{and} \qquad S^* = \hat{S}^*(\nu^p, \vartheta, \varphi). \end{aligned}\right\} \tag{3.8}$$

Next, we identify φ as

$$\varphi \stackrel{\text{def}}{=} \varphi_0 + \ln J^p, \tag{3.9}$$

with φ_0 a constant, so that the change in φ form its initial value φ_0 is due to the plastic volumetric strain $(\ln J^p)$. Then, the standard kinematical relation $\dot{J}^p = J^p \text{tr}\mathbf{L}^p$ gives $\dot{\varphi} = \text{tr}\mathbf{L}^p$, and hence, using (2.123), we obtain the following evolution equation for φ,

$$\dot{\varphi} = \beta \nu^p \qquad \text{with initial value} \qquad \varphi(\mathbf{X}, 0) = \varphi_0, \tag{3.10}$$

where β is the *shear-induced dilatancy function.* We take this dilatancy function to be given by

$$\beta = g\,(\varphi^* - \varphi)\,, \qquad \text{with} \qquad \varphi^* = \hat{\varphi}^*(\nu^p, \vartheta) \geq 0. \tag{3.11}$$

In these coupled evolution equations for S and φ, the parameters h_0, g, S_0 and φ_0 are constants. The function h represents the strain-hardening/softening function for the slip resistance during plastic flow: the material hardens $(h > 0)$ if $S < S^*$, and softens $(h < 0)$ if $S > S^*$. The critical value S^* of S controlling such hardening/softening transitions is assumed to depend on the current values of the plastic strain rate, temperature, and the order-parameter φ. In the dilatancy function, the parameter φ^* represents a strain rate and temperature dependent critical value for the order-parameter: the material dilates $(\beta > 0)$ when $\varphi < \varphi^*$, and compacts $(\beta < 0)$ when $\varphi > \varphi^*$. In a monotonic experiment at a given strain rate and temperature, the shear-induced dilatancy vanishes $(\beta = 0)$ when $\varphi =$

[2]Coupled differential evolution equations of this type have previously been used to model yield peaks in granular materials, Anand and Gu [13], as well as amorphous polymeric materials, Anand and Gurtin [14].

φ^*. However, in an experiment in which the strain rate and temperature are varying (e.g. strain rate or temperature jump experiments), the material will in general dilate or compact, depending on the strain rate and temperature history, and because of the coupling between the evolution equations for S and φ, the resistance S will also vary.

Particular forms for the functions $\hat{\varphi}^*(\nu^p, \vartheta)$ and $\hat{S}^*(\nu^p, \vartheta, \varphi)$ need to be specified. The function φ^* controls the amount of disordering the material undergoes during deformation and is both strain rate and temperature dependent. The strain rate and temperature dependence of φ^* is quite nonlinear; φ^* is expected to decrease with increasing temperature at a fixed strain rate, and increase with strain rate at a fixed temperature. Guided by the experimental data for the stress overshoot (cf. Figures 3-1, 3-2, 3-3, 3-4), we model this temperature and strain rate dependence of φ^* using the following functional form,

$$\varphi^* = \begin{cases} \varphi_s \left(1 - \left(\dfrac{\vartheta - \vartheta_0}{\vartheta_s}\right)^p\right)^q & \text{if } (\vartheta - \vartheta_0) \leq \vartheta_s, \\ 0 & \text{if } (\vartheta - \vartheta_0) > \vartheta_s, \end{cases} \tag{3.12}$$

with

$$\left.\begin{aligned} \varphi_s &= k_1 + k_2 \ln\left(\frac{\nu^p}{\nu_{\text{ref}}}\right), \\ \vartheta_s &= l_1 + l_2 \ln\left(\frac{\nu^p}{\nu_{\text{ref}}}\right), \end{aligned}\right\} \tag{3.13}$$

where $\{\vartheta_0, p, q, k_1, k_2, l_1, l_2, \nu_{\text{ref}}\}$ are constants. At a fixed strain rate, φ_s and ϑ_s are constant, and (3.12) describes the temperature variation of φ^* in the range $[\vartheta_0, \vartheta_s]$, with $\varphi^* = \varphi_s$ when $(\vartheta - \vartheta_0) = 0$ and $\varphi^* = 0$ when $(\vartheta - \vartheta_0) = \vartheta_s$; the parameters p and q control the nonlinear variation of φ^* between the limits $[\varphi_s, 0]$. The assumed strain rate dependence of φ_s and ϑ_s is given in (3.13).[3]

Further, for the function S^*, which controls the magnitude of the stress-overshoot, we assume

$$S^* = b\,(\varphi^* - \varphi)\,, \tag{3.14}$$

so that the value of S^* depends linearly on the difference between the current value of φ and the parameter φ^*. Also, since experimental data (cf. Figures 3-5, 3-6) shows that the magnitude of the stress overshoot is different in strain rate decrement and increment tests, we assign different values for the constant b during dilation ($\varphi < \varphi^*$), and compaction ($\varphi > \varphi^*$):

$$b = \begin{cases} b_{\text{dil}} & \text{if } \varphi < \varphi^*, \\ b_{\text{com}} & \text{if } \varphi > \varphi^*. \end{cases} \tag{3.15}$$

[3]Cf. Figure A-4, which schematically shows the temperature and strain rate variation of φ^* based on equations (3.12) and (3.13).

Next, we turn our attention to the term $\exp(-1/\zeta)$ in (3.6), which represents the concentration of flow defects. Having accounted for the deformation-induced disordering of the material via the internal variables S and φ, as discussed above, *we assume henceforth that the free volume ζ is only a function of temperature.*[4] Recall that in the Spaepen model the temperature dependence of the "equilibrium" value of ζ is taken in the linear Vogel-Fulcher-Tamann (VFT) form (3.5). Here, following [15] and [16], we adopt the Grest and Cohen [17] temperature dependent form for the free volume concentration,

$$\zeta(\vartheta) = \frac{1}{2d_1}\left[\vartheta - \vartheta_{\text{ref}} + \sqrt{(\vartheta - \vartheta_{\text{ref}})^2 + d_2\vartheta}\right], \tag{3.16}$$

where, d_1, d_2 and ϑ_{ref} are material constants. The non-linear Grest-Cohen relation (3.16) is well-defined at temperatures lower than ϑ_{ref}, and approaches a linear VFT-type relation at high temperatures.

In most previous models of viscoplastic flow of metallic glasses, attention has been restricted to temperature ranges either below ϑ_g or well-above ϑ_g (but below ϑ_x). In either of these two regimes, the activation energy ΔF and the activation volume V appearing in the thermally-activated model (3.6) may be assumed to have different but *constant* values in the two different temperature regimes. However, our interest here is in developing a simple model, which does not differ drastically from (3.6), but is able to capture the strain-rate and temperature dependent response of metallic glasses through the important, but difficult to model, temperature range of $0.9\vartheta_g \lesssim \vartheta \lesssim \vartheta_x$. We accomplish this by assuming that

- *the activation energy ΔF decreases, and the activation volume V increases, as the temperature increases from approximately $0.9\vartheta_g$ through ϑ_g to ϑ_x.*

Specifically, for the temperature dependence of the activation energy ΔF we adopt the following simple phenomenological form,

$$\Delta F(\vartheta) = \frac{1}{2}(\Delta F_{gl} + \Delta F_{sc}) - \frac{1}{2}(\Delta F_{gl} - \Delta F_{sc})\tanh\left(\frac{1}{\Delta_F}(\vartheta - \vartheta_{\text{g}})\right), \tag{3.17}$$

where ΔF_{gl} and $\Delta F_{sc}(< \Delta F_{gl})$ are the values of the activation energies in the glassy and supercooled liquid regions; and $\Delta_F > 0$ is a parameter denoting the temperature range across which the assumed hyperbolic-tangent-type transition in the value of the activation energy from ΔF_{gl} to ΔF_{sc} occurs.

Similarly, for the temperature dependence of the activation volume V we adopt the form,

$$V(\vartheta) = \frac{1}{2}(V_{gl} + V_{sc}) - \frac{1}{2}(V_{gl} - V_{sc})\tanh\left(\frac{1}{\Delta_V}(\vartheta - \vartheta_{\text{v}})\right), \tag{3.18}$$

[4] In our phenomenological macroscopic theory the order-parameter φ appears as an internal variable which is distinct from the free volume ζ in Spaepen's theory. However, physically, φ may be thought of as the *change* in the free volume due to deformation-induced disordering from the purely temperature dependent equilibrium value ζ .

where V_{gl} and $V_{sc}(> V_{gl})$ are values of the activation volumes in the glassy and supercooled liquid regions; ϑ_V is the temperature at which the activation volume begins to increase (not necessarily equal to ϑ_g); and $\Delta_V > 0$ is a parameter denoting the temperature range across which the transition occurs.

3.4 Elastic Moduli

Finally, the elastic moduli also change as the temperature changes across the range of interest. Since measurements of temperature variations of elastic moduli are typically made for the Young's modulus E, we first consider the temperature variation of this constitutive modulus. Following the work of [18] on amorphous polymers, we assume that the temperature dependence of the Young's modulus may be adequately approximated by the function

$$E(\vartheta) = \frac{1}{2}(E_{gl} + E_{sc}) - \frac{1}{2}(E_{gl} - E_{sc})\tanh\left(\frac{1}{\Delta_E}(\vartheta - \vartheta_g)\right) + k_E(\vartheta - \vartheta_g), \tag{3.19}$$

where E_{gl} and $E_{sc}(< E_{gl})$ are representative moduli in the glassy and supercooled liquid regions; and Δ_E is a parameter denoting the temperature range across which this transition occurs, and k_E represents the slope of the temperature variation of E beyond the transition region, where

$$k_E = \begin{cases} k_{E_{gl}} & \vartheta \leq \vartheta_g, \\ k_{E_{sc}} & \vartheta > \vartheta_g. \end{cases} \tag{3.20}$$

Further, for the temperature dependence of Poisson's ratio we assume

$$\nu(\vartheta) = \frac{1}{2}(\nu_{gl} + \nu_{sc}) - \frac{1}{2}(\nu_{gl} - \nu_{sc})\tanh\left(\frac{1}{\Delta_E}(\vartheta - \vartheta_g)\right) \tag{3.21}$$

with ν_{gl} and ν_{sc} representative values of Poisson's ratio below and above the temperature ϑ_g respectively. Using (3.19) and (3.21), the temperature dependent values of the shear and bulk moduli may then be found by using the standard relations:

$$G(\vartheta) = \frac{E(\vartheta)}{2(1 + \nu(\vartheta))}, \qquad K(\vartheta) = \frac{E(\vartheta)}{3(1 - 2\nu(\vartheta))}. \tag{3.22}$$

3.5 Stress-strain response of the metallic glass $Zr_{41.2}Ti_{13.8}Cu_{12.5}Ni_{10}Be_{22.5}$

We have estimated the materials parameters appearing in our constitutive model for $Zr_{41.2}Ti_{13.8}Cu_{12.5}Ni_{10}Be_{22.5}$ from the data published by Lu et al. [2], Masuhr et al. [15], and Tsau et al. [19] for this material. For ease of presentation, we relegate our procedure for material parameter estimation to Appendix A.

Figures 3-1, 3-2, 3-3, and 3-4 compare the one-dimensional stress-strain curves (dashed lines) calculated using our model, with the corresponding experimental results (solid lines) of Lu et al. [2], from which the material parameters were estimated. The quality of the fit over a wide range of temperatures and strain rates of interest is quite reasonable.

Predictions from the model were also compared against corresponding experimental data from the strain rate jump experiments of Lu et al. [2]. Figures 3-5 and 3-6 compare the experimental data and the model predictions for several of these strain rate increment and decrement experiments at temperatures both below and above T_g. The quality of the predictions over a wide variety of strain rate histories is quite encouraging.

A feature of the stress-strain response of metallic glasses of particular interest is the "steady-state stress," that is, the stress level at a given temperature and strain rate beyond which the stress level reaches a plateau and is essentially constant; cf. Figures 3-1, 3-2, 3-3, and 3-4. Our model, when specialized to a one-dimensional situation (cf. Appendix A), shows that in a fully-developed state at a given temperature ϑ and an axial strain rate $\dot{\epsilon}$, the axial stress reaches the steady-state stress σ_{ss} given by (A.9), viz.

$$\sigma_{ss} = \frac{4k_B\vartheta}{V}\sinh^{-1}\left(\frac{\dot{\epsilon}}{2\nu_0}\exp\left(\frac{1}{\zeta}\right)\exp\left(\frac{\Delta F}{k_B\vartheta}\right)\right). \tag{3.23}$$

Figure 3-7a shows the variation of the steady-state stress σ_{ss} versus the strain rate $\dot{\epsilon}$ at various temperatures, and compares it with the corresponding experimental data extracted from Lu et al. [2]. The quality of the fit of the model to the experimental data is quite reasonable.

Equation (3.23) may be used to define a strain rate and temperature dependent non-Newtonian shear viscosity

$$\eta\left(\dot{\epsilon},\vartheta\right) \stackrel{\text{def}}{=} \frac{\sigma_{\text{ss}}}{3\dot{\epsilon}} = \frac{4k_B\vartheta}{3V\dot{\epsilon}}\sinh^{-1}\left(\frac{\dot{\epsilon}}{2\nu_0}\exp\left(\frac{1}{\zeta}\right)\exp\left(\frac{\Delta F}{k_B\vartheta}\right)\right). \tag{3.24}$$

Under high temperatures and low strain rates, the inverse hyperbolic sine term in (3.24) may be approximated by its argument to obtain an expression for a Newtonian viscosity which is only a function of temperature,

$$\eta_{\text{Newtonian}}\left(\vartheta\right) = \frac{2k_B\vartheta}{3V\nu_0}\exp\left(\frac{1}{\zeta}\right)\exp\left(\frac{\Delta F}{k_B\vartheta}\right). \tag{3.25}$$

Figure 3-7b shows the experimental data of Figure 3-7a re-plotted in terms of a non-Newtonian viscosity as a function of the temperature at various strain rates, and compared against the curves generated according to (3.24); the Newtonian approximation (3.25) is also shown in this figure as a dashed line. As is clear from this figure, the model nicely reproduces the important transition of the viscosity from a non-Newtonian response to a Newtonian response as the material goes through the glass transition.

We have implemented our constitutive model in the finite element program ABAQUS/ Explicit [20] by writing a user-material subroutine. In the next chapter, we use this simulation capability to determine appropriate processing conditions for a representative micron-scale hot-embossing process for Vitreloy-1.

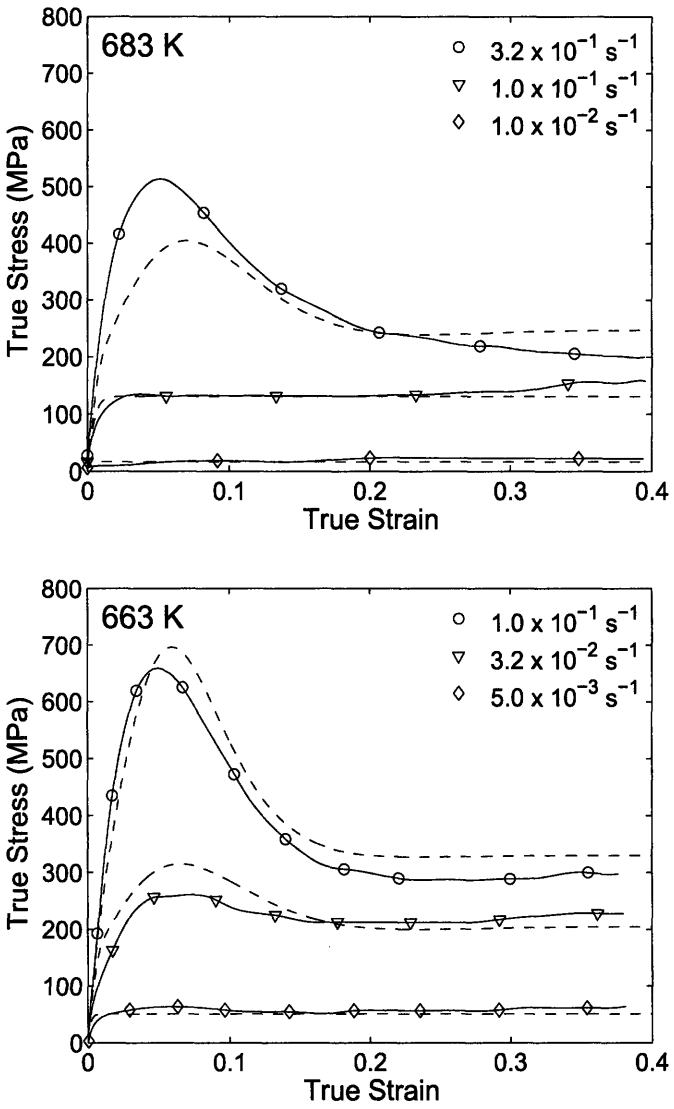

Figure 3-1: Stress-strain curves for Vitreloy-1 at various temperatures and strain rates from Lu et al. [2]. The solid lines are the experimental data, and the dashed lines are results from the model. Markers serve to distinguish data at different strain rates; they do not represent individual data points.

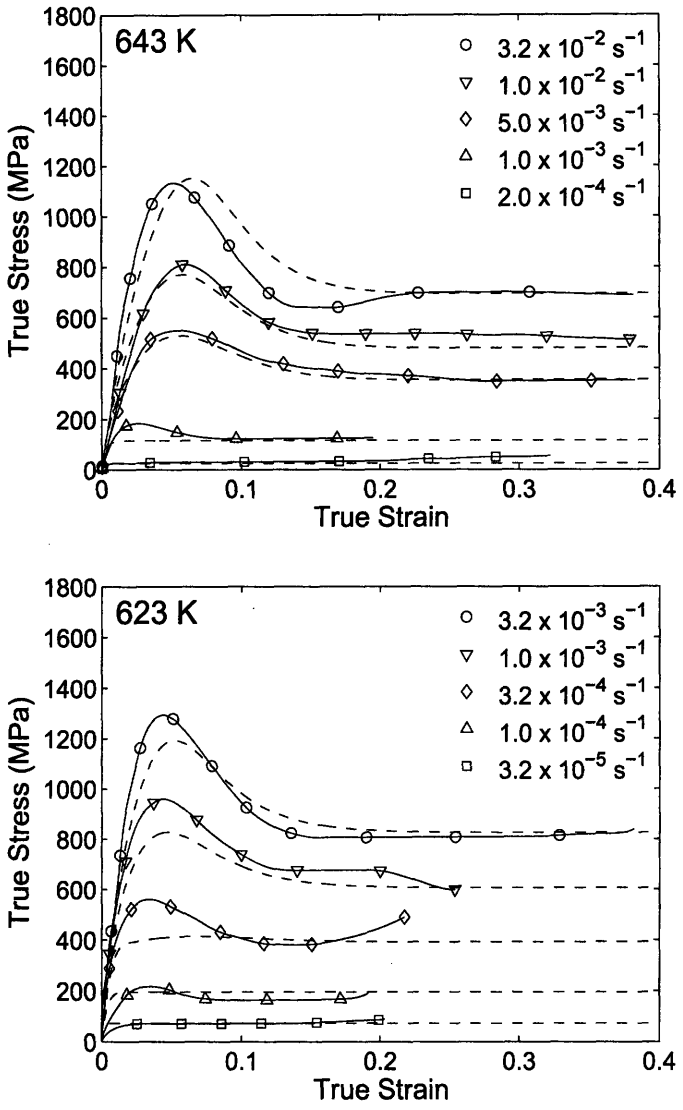

Figure 3-2: Stress-strain curves for Vitreloy-1 at various temperatures and strain rates from Lu et al. [2]. The solid lines are the experimental data, and the dashed lines are results from the model. Markers serve to distinguish data at different strain rates; they do not represent individual data points.

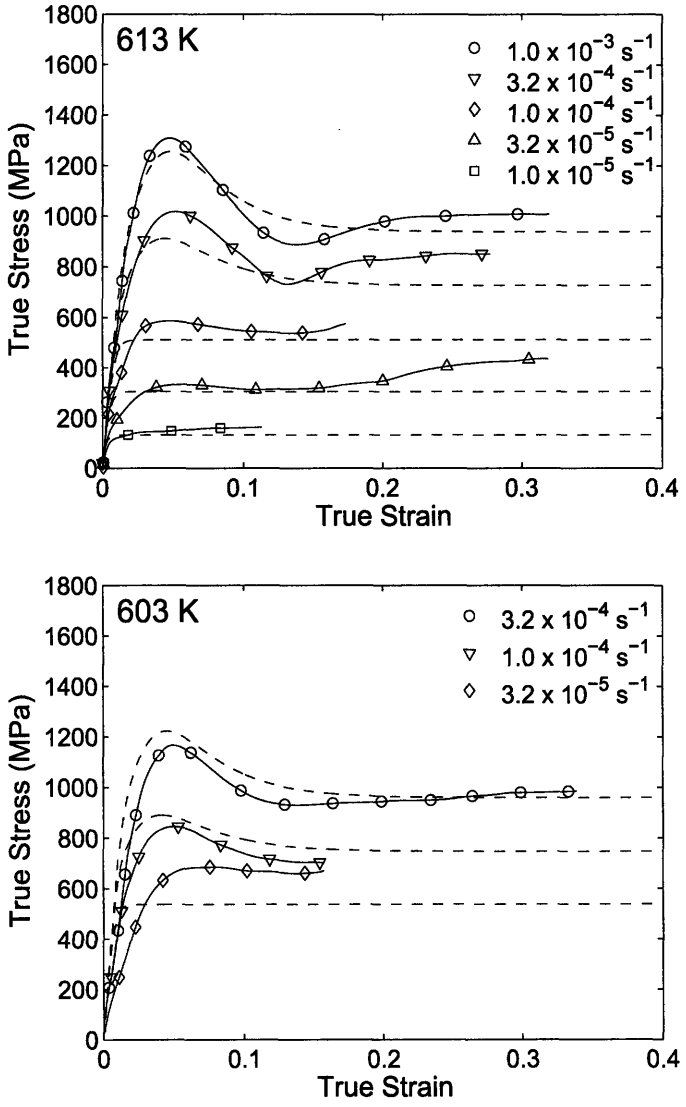

Figure 3-3: Stress-strain curves for Vitreloy-1 at various temperatures and strain rates from Lu et al. [2]. The solid lines are the experimental data, and the dashed lines are results from the model. Markers serve to distinguish data at different strain rates; they do not represent individual data points.

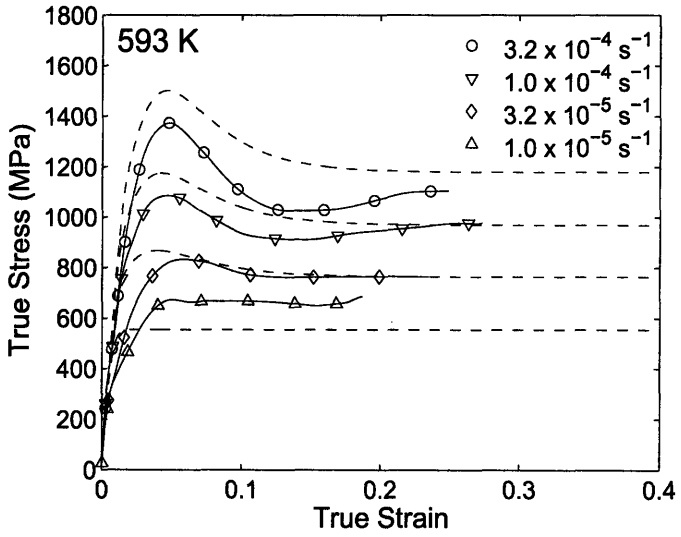

Figure 3-4: Stress-strain curves for Vitreloy-1 at various temperatures and strain rates from Lu et al. [2]. The solid lines are the experimental data, and the dashed lines are results from the model. Markers serve to distinguish data at different strain rates; they do not represent individual data points.

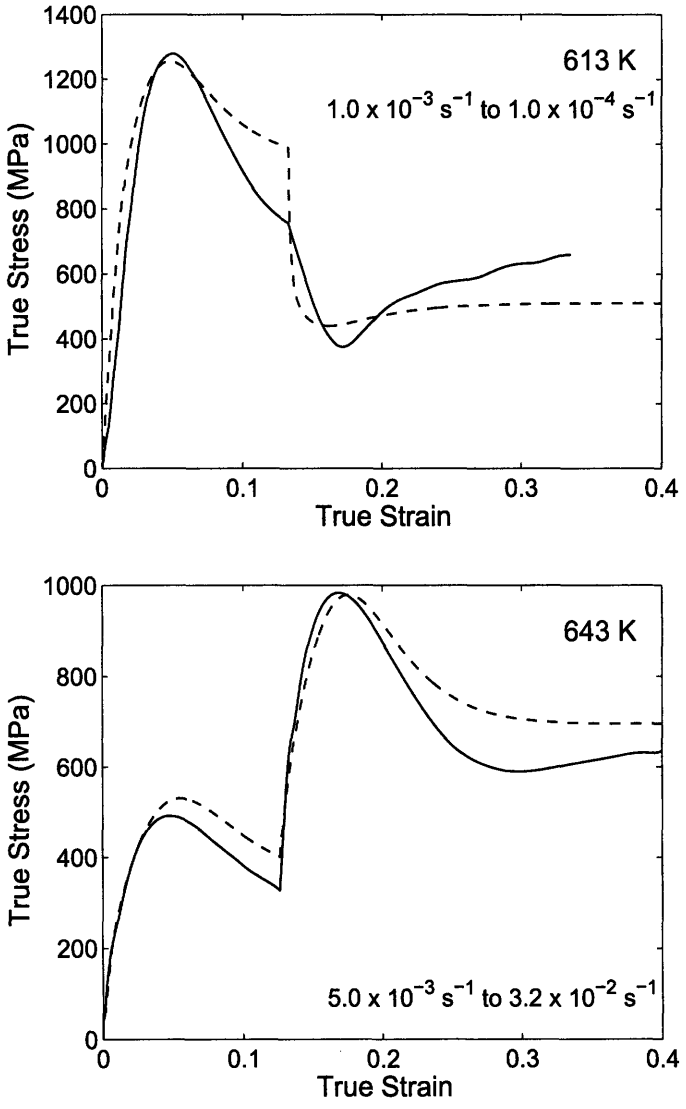

Figure 3-5: Stress-strain curves from strain rate decrement and increment experiments for Vitreloy-1 from Lu et al. [2]. The solid lines are the experimental data, and the dashed lines are results from the model.

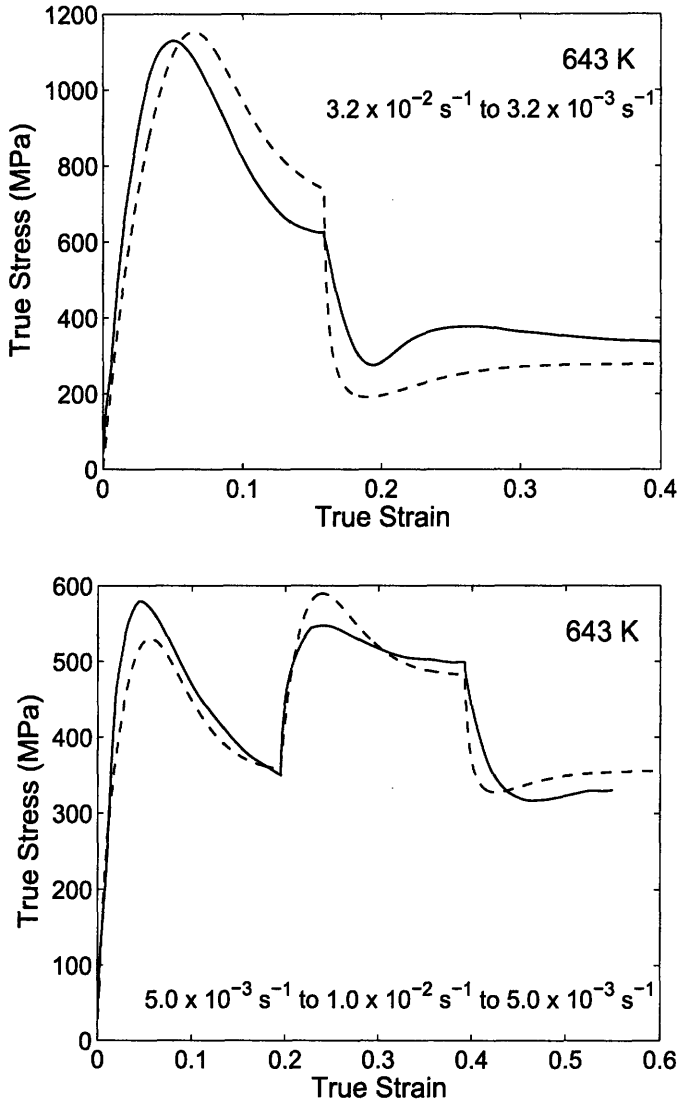

Figure 3-6: Stress-strain curves from strain rate decrement and increment experiments for Vitreloy-1 from Lu et al. [2]. The solid lines are the experimental data, and the dashed lines are results from the model.

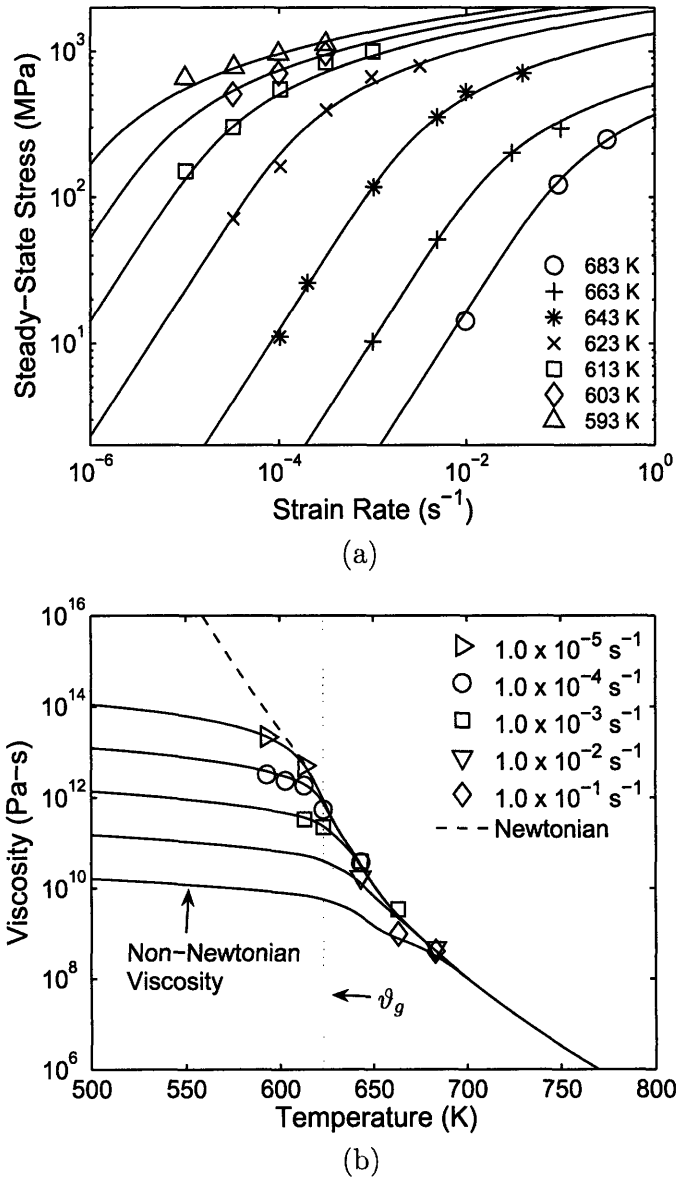

Figure 3-7: (a) Steady-state stress as a function of temperature and strain rate. (b) Viscosity as a function of temperature and strain rate. Points are data from [2]; each point represents a single monotonic compression experiment. Lines are the model prediction.

Bibliography

[1] F. Spaepen. A microscopic mechanism for steady state inhomogeneous flow in metallic glasses. *Acta Metallurgica*, 25:407–415, 1977.

[2] J. Lu, G. Ravichandran, and W. L. Johnson. Deformation behavior of the $Zr_{41.2}Ti_{13.8}Cu_{12.5}Ni_{10.0}Be_{22.5}$ bulk metallic glass over a wide range of strain-rates and temperatures. *Acta Materialia*, 51:3429–3443, 2003.

[3] A S Argon. Plastic deformation in metallic glasses. *Acta Metallurgica*, 27:47–58, 1979.

[4] P. E. Donovan. Compressive deformation of amorphous $Pd_{40}Ni_{40}P_{20}$. *Materials Science and Engineering*, 98:487–490, 1988.

[5] P. E. Donovan. A yield criterion for $Pd_{40}Ni_{40}P_{20}$ metallic glass. *Acta Metallurgica*, 37: 445–456, 1989.

[6] P. de Hey, J. Sietsma, and A. Beukel. Structural disordering in amorphous $Pd_{40}Ni_{40}P_{20}$ induced by high temperature deformation. *Acta Materialia*, 46:5873–5882, 1998.

[7] M Bletry, P Guyot, J J Blandin, and J L Soubeyroux. Free volume model: High-temperature deformation of a Zr-based bulk metallic glass. *Acta Materialia*, 54:1257–1263, 2006.

[8] A S Argon. Inelastic deformation and fracture of glassy solids. *Materials Science and Technology*, 6:461–508, 1993.

[9] M L Falk and J S Langer. Dynamics of viscoplastic deformation in amorphous solids. *Physical Review E*, 57:7192–7205, 1998.

[10] Y F Shi and M L Falk. Atomic-scale simulations of strain localization in three-dimensional model amorphous solids. *Physical Review B*, 73:214201, 2006.

[11] A S Argon and M J Demkowicz. Atomistic simulation and analysis of plasticity in amorphous silicon. *Philosophical Magazine*, 86:4153–4172, 2006.

[12] N P Bailey, J Schiotz, and K W Jacobsen. Atomistic simulations of metallic glasses: Mechanical properties. *Physical Review B*, 73:064108, 2006.

[13] L. Anand and C. Gu. Granular materials: constitutive equations and strain localization. *Journal of the Mechanics and Physics of Solids*, 48:1701–1733, 2000.

[14] L. Anand and M. Gurtin. A theory of amorphous solids undergoing large deformations, with application to polymeric glasses. *International Journal of Solids and Structures*, 40:1465–1487, 2003.

[15] A. Masuhr, T. A. Waniuk, R. Busch, and W. L. Johnson. Time scales for viscous flow, atomic transport, and crystallization in the liquid and supercooled liquid state of $Zr_{41.2}Ti_{13.8}Cu_{12.5}Ni_{10.0}Be_{22.5}$. *Physical Review Letters*, 82, 1999.

[16] Q. Yang, A. Mota, and M. Ortiz. A finite deformation constitutive model of bulk metallic glass plasticity. *Computational Mechanics*, 37:194–204, 2006.

[17] G S Grest and M H Cohen. Liquids, glasses, and glass transition: a free-volume approach. *Advances in Chemical Physics*, 48:455–525, 1981.

[18] R. B. Dupaix and M. C. Boyce. Constitutive modeling of the finite strain behavior of amorphous polymers in and above the glass transition. *Mechanics and Materials*, 39: 39–52, 2007.

[19] C.-H. Tsau, C.-C. Wu, and S.-S. Wu. The thermal stability and mechanical behaviors of $Zr-Cu-Ni-Ti-Be$ bulk metallic glasses. *Journal of Materials Processing Technology*, 182:257–261, 2007.

[20] ABAQUS, Inc. ABAQUS Reference Manuals, 2006.

Chapter 4

Micro-hot-embossing: numerical simulations and experiments

4.1 Introduction

Numerical simulation of micro-hot-embossing processes for metallic glasses are virtually non-existent. Most previously published attempts [1–6] have been hampered by the lack of a suitable constitutive model and its numerical implementation in a finite element program. In this chapter, we utilize our elastic-viscoplastic, large-deformation theory for metallic glasses and its numerical implementation in Abaqus/Explicit [7] by carrying out representative hot-embossing simulations and comparing aspects of the results from such simulations against the corresponding experimental results. We begin by considering a simple pattern consisting of a series of long channels. Then, we consider a pattern with practical applicability, that of a microfluidic mixer. We subsequently use the resulting metallic glass part in the manufacture of a polymeric microfluidic device.

4.2 A plain strain micro-hot-embossing

4.2.1 Finite element simulation

As a simple example of a micro-hot-embossing process, we consider the embossing of a series of long raised ridges into a bulk metallic glass substrate. To this end, a silicon tool was manufactured using deep-reactive-ion-etching (DRIE) of a 4 inch diameter silicon wafer. The pattern consists of 240 micron wide channels, 33 microns deep, spaced 360 microns apart. Figure 4-1a shows a schematic of the pattern, and Figure 4-1b shows an SEM photomicrograph of a portion of the silicon tool.

Since the channels are long relative to their width, and there are a large number of them aligned in parallel, we employ a plane strain idealization in our numerical simulation and consider only a single half-segment, with suitable boundary conditions. Figure 4-1c shows the finite element mesh. The metallic glass substrate is modeled using a mesh consisting of 1035 ABAQUS-CPE4R plane strain elements, and the silicon tool is modeled using an appropriately shaped rigid surface. Contact between the substrate and tool was approximated as frictionless. The displacement boundary conditions on the portions AD and BC of the mesh boundary are $u_1 = 0$, while on the portion CD of the mesh, $u_1 = u_2 = 0$ are prescribed.

The simulations were performed under typical conditions for micro-hot-embossing. We chose a temperature of 420°C and a process time of 2 minutes; for Vitreloy-1 the risk of crystallization and the subsequent deterioration of mechanical properties under these process conditions is expected to be minimal [e.g. 5, 6]. In our numerical simulations, we sought to determine a molding pressure that will result in good replication. After a few trial simulations, it was found that for the geometry under consideration, at 420°C, a pressure of 20 MPa would result in a filled mold after 2 minutes. Figure 4-2a,b show the time-histories of the compressive pressure and the vertical position of the tool. Figure 4-2c shows contours of the equivalent plastic strain ($\int_0^t \nu^p(\chi)\, d\chi$) after 20 seconds when the mold is only partially filled, and Figure 4-2d shows the contours of equivalent plastic strain at 120 seconds when the mold has completely filled; as expected, the plastic strain is greatest in the corner of the mold. It is noteworthy that while the mold reaches a steady position of 12μm after about 20 seconds, additional time under pressure is required for the mold to fill completely. Thus, sufficient hold time at pressure is needed to fill intricate geometries.

In the next section, we describe the results of a micro-hot-embossing experiment carried out under these processing conditions.

4.2.2 Experimental procedures and results

The hot-embossing experiment was carried out on a servo-hydraulic Instron testing machine equipped with heated compression platens.[1] A 12 mm square sheet specimen of Vitreloy-1 and a 12 mm square patterned-silicon tool were aligned and placed between the heated compression platens. The embossing experiment was conducted under nominally isothermal conditions at a temperature of 420°C in air. The load was ramped up to produce a pressure of 20 MPa in 2 seconds, and thereafter held constant for another 2 minutes. Following the embossing process, the metallic glass substrate and silicon wafer, now bonded together, are removed from the load frame. The metallic glass is separated from the silicon mold by etching away the silicon in a heated KOH bath, leaving the embossed metallic glass part.

Figure 4-3a shows an SEM image of two channels in the silicon tool, and Figure 4-3b (a closeup of the side-wall of a channel) shows the micron-level scalloping produced by the DRIE process used to manufacture the tool. SEM images of embossed ridges in Vitreloy-1 are shown Figure 4-3c, and Figure 4-3d shows a closeup of the side-wall of a ridge in

[1]For a detailed explanation of the procedures employed in this micro-hot-embossing experiment, see Appendix B

the embossed BMG. These results show good mold-filling and replication under the process conditions. The closeup images of the walls of the tool and the embossed features show that the BMG replicates the small-scale striations produced in the silicon mold during deep reactive ion etching. Thus, even though the macroscopic features in our silicon tool are on the order of tens of microns, the BMG can replicate features in the tool which are as small as $\approx 1\,\mu$m.

We further investigated the quality of the embossed feature by using optical profilometry methods. Figure 4-4 compares cross-sections of the silicon tool and the embossed BMG feature, along with 3D images of a channel in the tool and a corresponding ridge in the embossed substrate. The dimensions of the embossed feature closely match those of the corresponding feature in the mold.

4.3 Embossing of a microfluidic mixer device

While the embossing of the previous pattern serves as a good representative hot-embossing process, the resulting metallic glass part has little applicability. In this section, we wish to produce a metallic glass part with practical use. An emerging application for micro-patterned metallic glass surfaces is as a die for the embossing of polymeric microfluidic devices. In recent micro-hot-embossing studies on polymeric materials [cf., e.g., 8–13], patterned silicon wafers are predominantly used as mold materials. Unlike in the hot-embossing of metallic glasses where the tool is considered sacrificial, in the embossing of polymeric materials, the tool may be demolded from the polymeric part to be used again. However, silicon is a highly brittle material and generally fails after only a few embossings. Therefore, patterned metallic glass surfaces may be used as highly robust tooling for the micro-hot-embossing of polymeric microfluidic devices.

In this section, we use the simulation capability to determine appropriate processing parameters to produce a metallic glass part with a microfluidic device pattern. We then use the resulting part to produce a polymeric microfluidic device.

4.3.1 Finite element simulation

The pattern considered in this example is that of a standard snake mixer. This pattern consists of two inlets which converge into a single channel. This channel then winds around forming a series of long, straight, parallel channels before finally terminating in a single outlet. The channel is 50 microns wide and 65 microns deep. A schematic of the mixer pattern is shown in Figure 4-5a, and a schematic of the channel cross-section is shown in Figure 4-5b. As in the previous example, a silicon tool was manufactured using DRIE. Figures 4-6 show SEM photomicrographs of several portions of the silicon tool.

Since the microfluidic mixer is a complex three-dimensional pattern, simulation of the entire pattern would be prohibitively expensive computationally. The bulk of the pattern consists of long, straight, parallel channels. Thus, we take the same approach as in the previous section and employ a plane strain idealization, considering a single half-segment with

suitable boundary conditions. Figure 4-5c shows the finite element mesh. The metallic glass substrate is modeled using a mesh consisting of 3047 ABAQUS-CPE4R plane strain elements, and the silicon tool is modeled using an appropriately shaped rigid surface. As before, contact between the substrate and tool is approximated as frictionless, and the displacement boundary conditions on the portions AD and BC of the mesh boundary are $u_1 = 0$, while on the portion CD of the mesh, $u_1 = u_2 = 0$ are prescribed.

Again, we chose typical conditions for micro-hot-embossing, specifically a temperature of 420°C and a process time of 2 minutes, and use the simulation capability to determine a molding pressure that will result in good replication. We wish for the entire process to be completed in two minutes; however, we are only simulating a portion of the pattern, the long, straight channels. Therefore, in order to ensure that the other features of the pattern, i.e. the bends and the inlets and outlet, are filled, we seek a pressure that will result in a filled mold after 90 seconds. After a few trial simulations, it was found that for the geometry under consideration, at 420°C, a pressure of 40 MPa would result in a filled mold after 90 seconds. Figure 4-7a,b show the time-histories of the compressive pressure and the vertical position of the tool. Figure 4-7c shows contours of the equivalent plastic strain after 90 seconds when the mold is filled, and once again, as expected, the plastic strain is greatest in the corner of the mold. Furthermore, the magnitude of equivalent plastic strain is significantly greater in this example than in the previous process; however, the plastic strain is predominantly localized to the wall of the resulting ridge. In this process, the long, straight channels of the pattern will be replicated after 90 seconds under 40 MPa at 420°C. An extra 30 seconds of hold time are allotted to ensure complete replication of all the features of the pattern.

In the following section, we describe the results of a micro-hot-embossing experiment carried out under these processing conditions, as well as the embossing of a polymeric microfluidic device.

4.3.2 Experimental procedures and results

The hot-embossing experiment was carried out on the same apparatus and using similar procedures as the previous example. In this case, a 12 mm by 25 mm sheet specimen of Vitreloy-1, and a 12 mm by 25 mm patterned-silicon tool were aligned and placed between the heated compression platens. The embossing experiment was conducted at a temperature of 420°C, and the load was ramped up to produce a pressure of 40 MPa in 2 seconds, and thereafter held constant for another 2 minutes. The metallic glass part was then separated from the silicon mold via a heated KOH bath.

Figure 4-8 shows SEM images of various portions of the BMG part, including a channel, a bend, and part of an inlet. These results show good mold-filling and replication under the process conditions. Thus, a complex pattern with practical applicability was successfully produced under the conditions determined by the numerical simulation capability.

Next, the resulting metallic glass part was used for its intended purpose: to emboss a polymeric microfluidic device. The amorphous polymer used in this study was the cyclo-olefin-polymer Zeonex 690R with a glass transition temperature of 136°C. From a recent

study on the micro-hot-embossing of Zeonex 690R [14], it has been determined that embossing at 165°C for 2 minutes under a pressure of 2 MPa is sufficient for good replication. This process was then carried out using the same embossing apparatus on a 12 mm by 25 mm sheet of Zeonex 690R. After the embossing was completed, the polymeric part and metallic glass tool were left under pressure as the apparatus cooled to below the glass transition of the polymer. This was done to minimize distortion of the features in the polymeric device upon cooling. After the assembly had sufficiently cooled, the pressure was removed, and the polymeric part and metallic glass tool were physically separated. The metallic glass tool suffered no degradation during this process and may be used for further embossing procedures. SEM images of various portions of the resulting polymeric device are shown in Figure 4-9. Here we see accurate replication of the intended geometry. Thus, we have successfully reproduced the pattern of a microfluidic mixer in a polymeric material without degradation to the metallic glass mold. This work demonstrates an emerging application for micro-patterned surfaces manufactured from metallic glasses.

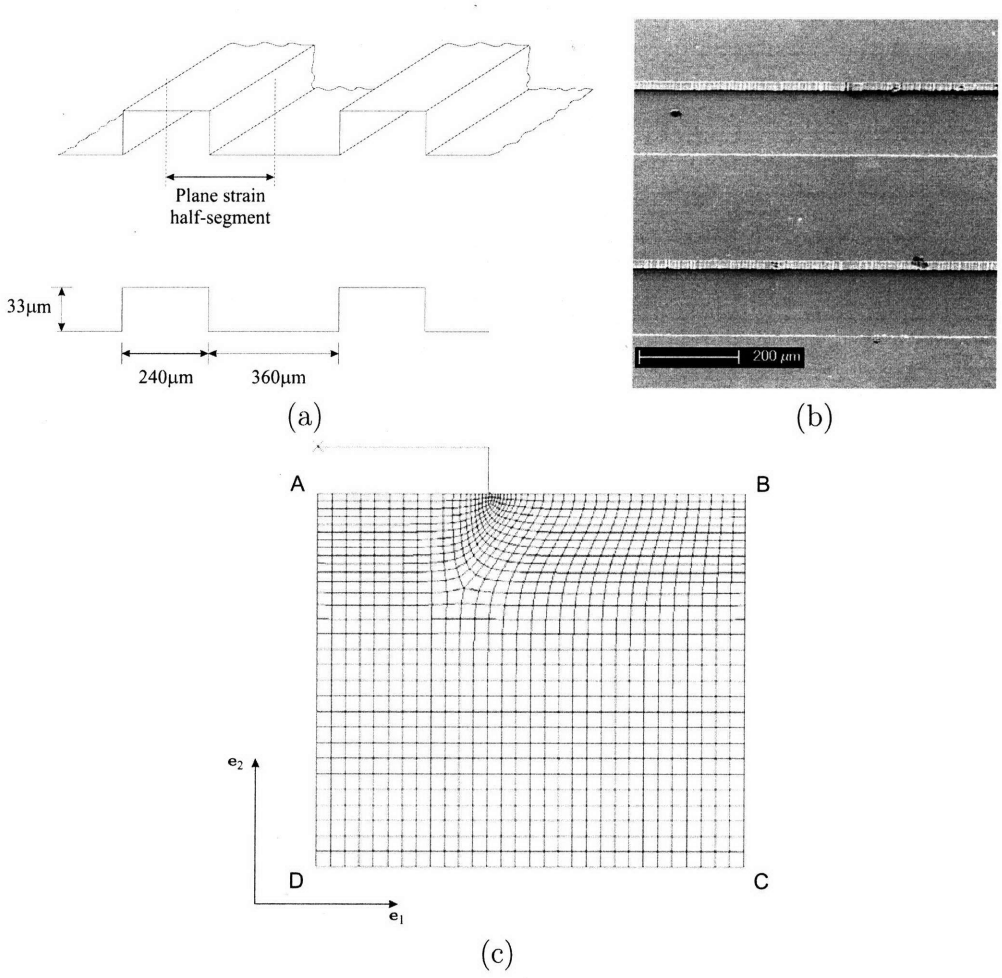

Figure 4-1: (a) Schematic of plane strain tool (not to scale). (b) SEM image of the silicon tool. (c) Finite element mesh for a plane strain simulation showing the meshed substrate and the tool modeled as a rigid surface. The displacement boundary conditions on the portions AD and BC of the mesh boundary are $u_1 = 0$, while on the portion CD of the mesh, $u_1 = u_2 = 0$ are prescribed.

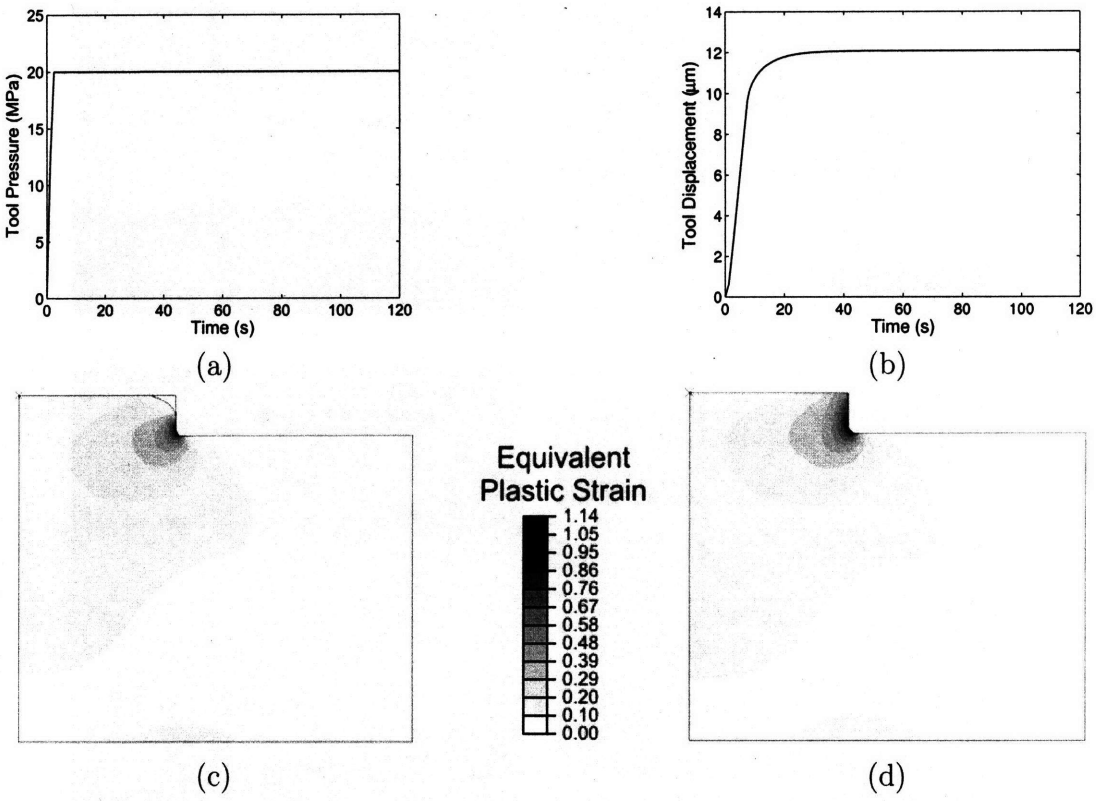

Figure 4-2: (a) Tool pressure history. (b) Tool displacement history. (c) Partially filled mold at 20 seconds. (d) Filled mold at 120 seconds.

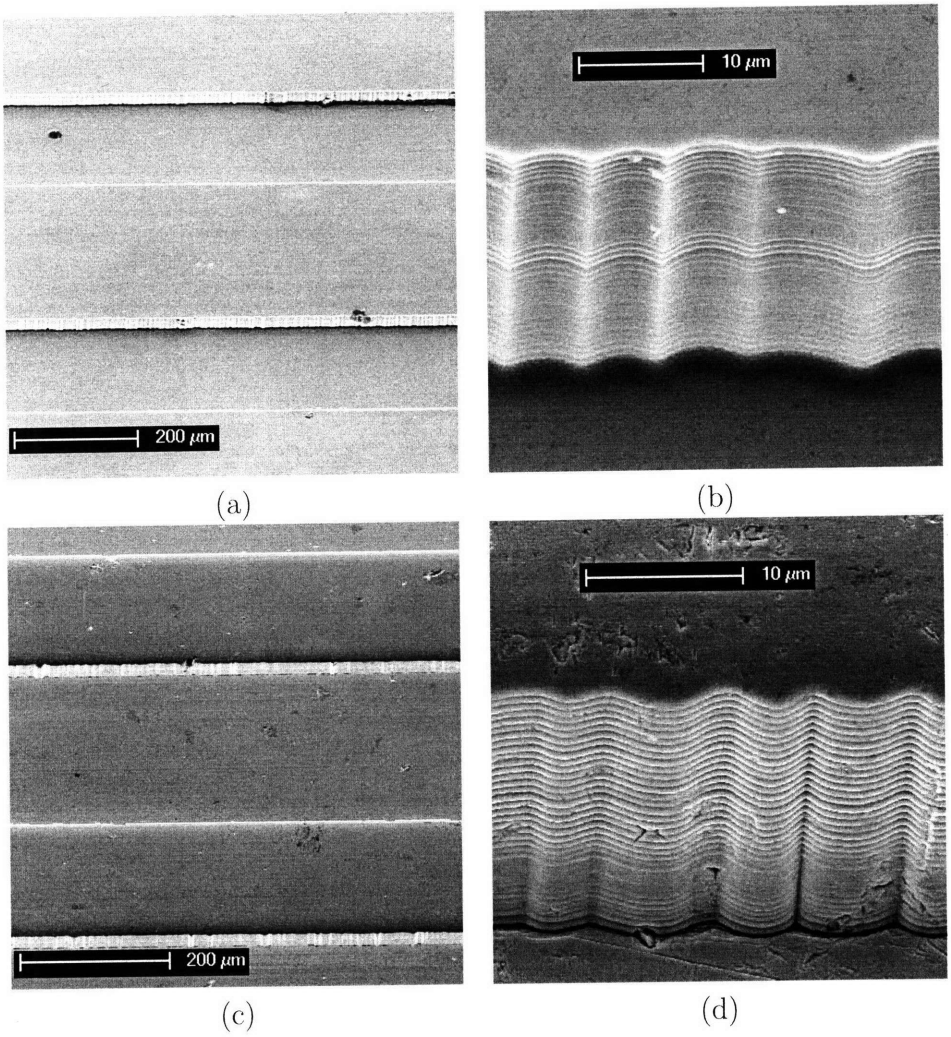

Figure 4-3: (a) SEM image of silicon tool. (b) Closeup of the side-wall of a channel in the silicon tool showing the micron-level scalloping produced by DRIE. (c) SEM image of embossed ridges in Vitreloy-1. (d) Closeup of the side-wall of a ridge in the embossed BMG – the scalloped walls of the channels in the tool are nicely replicated.

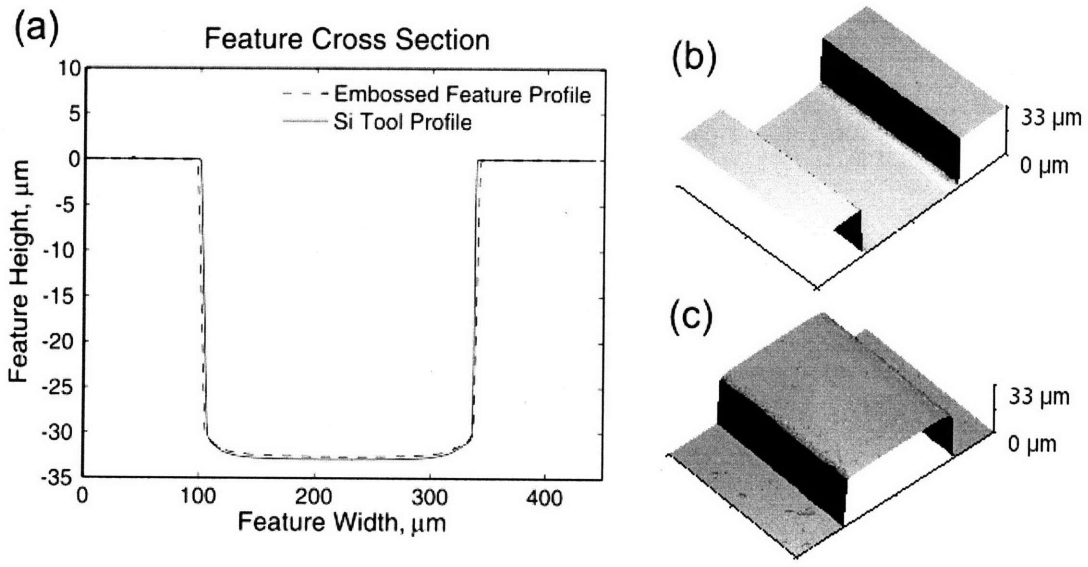

Figure 4-4: (a) Comparisons of the cross sections of the silicon mold and embossed feature in the metallic glass. (b) 3D image of a channel in the silicon mold. (c) Corresponding image of the embossed ridge in the metallic glass substrate.

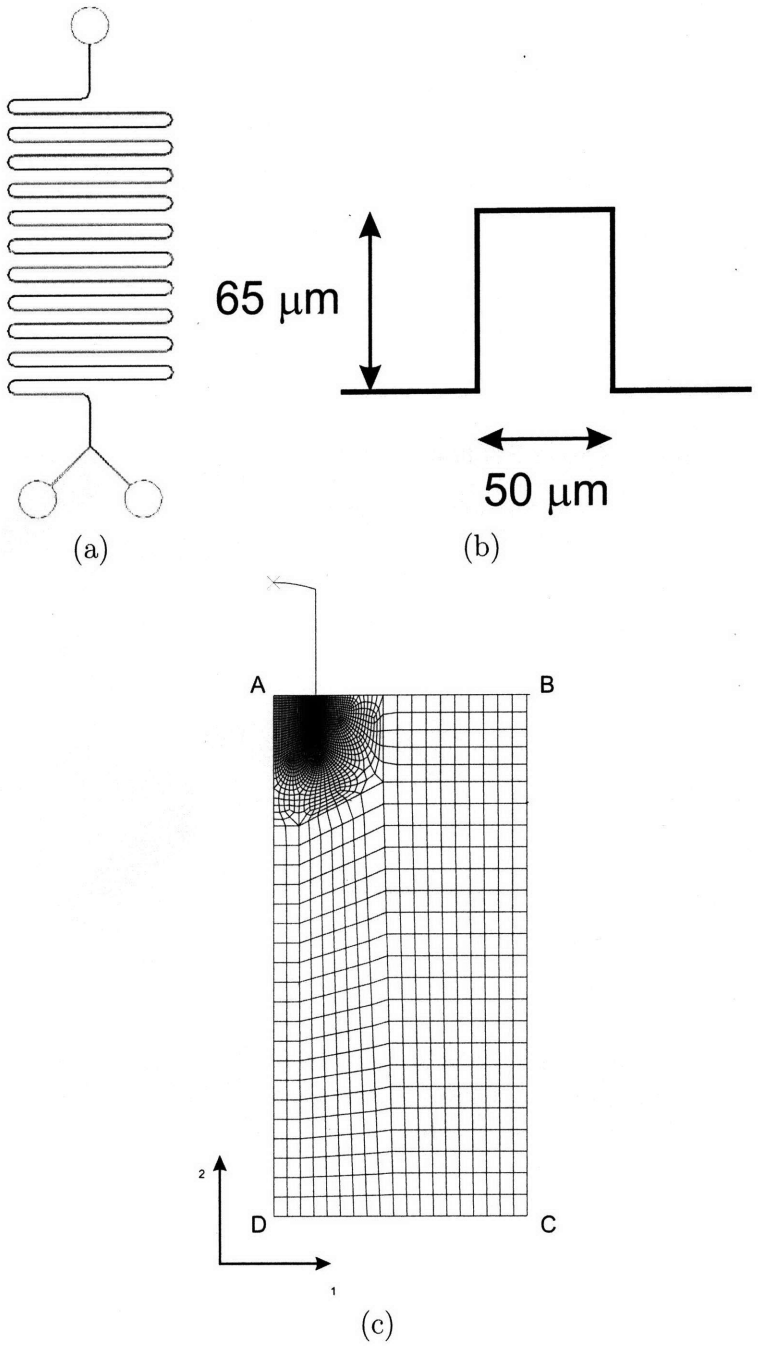

Figure 4-5: (a) Schematic of the microfluidic mixer pattern. (b) Schematic of the channel cross-section. (c) Finite element mesh for a plane strain simulation showing the meshed substrate and the tool modeled as a rigid surface. The displacement boundary conditions on the portions AD and BC of the mesh boundary are $u_1 = 0$, while on the portion CD of the mesh, $u_1 = u_2 = 0$ are prescribed.

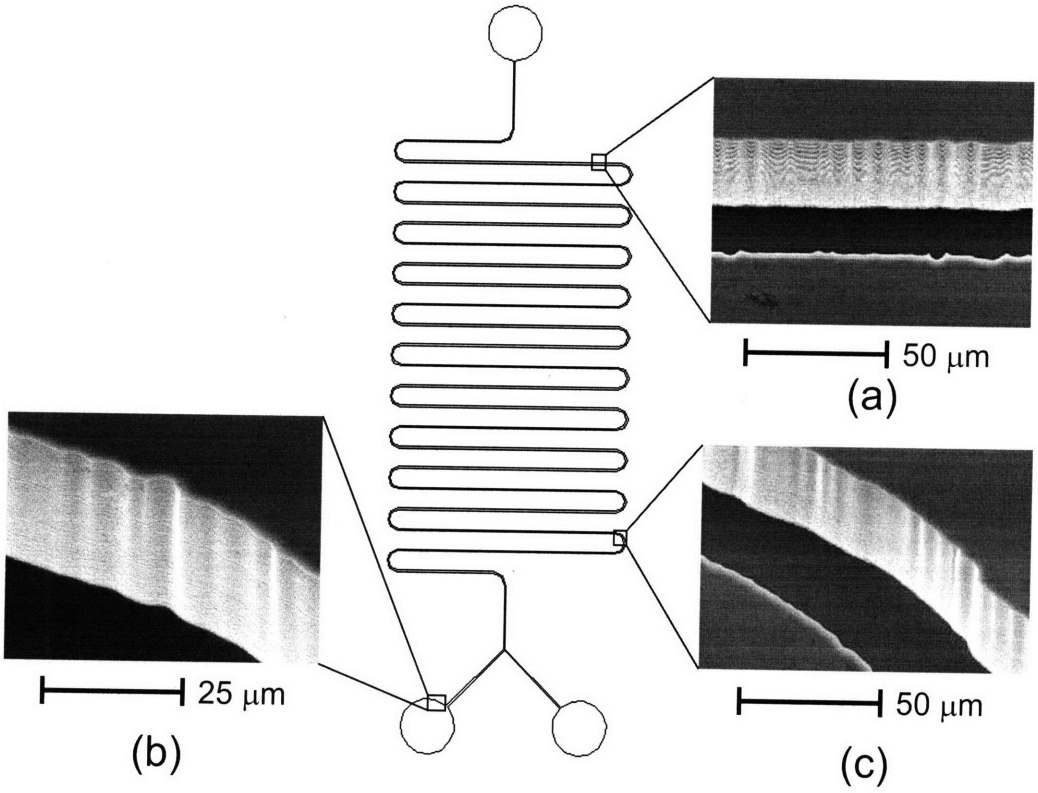

Figure 4-6: SEM micrographs of the silicon tool used to emboss a microfluidic mixer pattern, including (a) a channel, (b) part of an inlet, and (c) a bend.

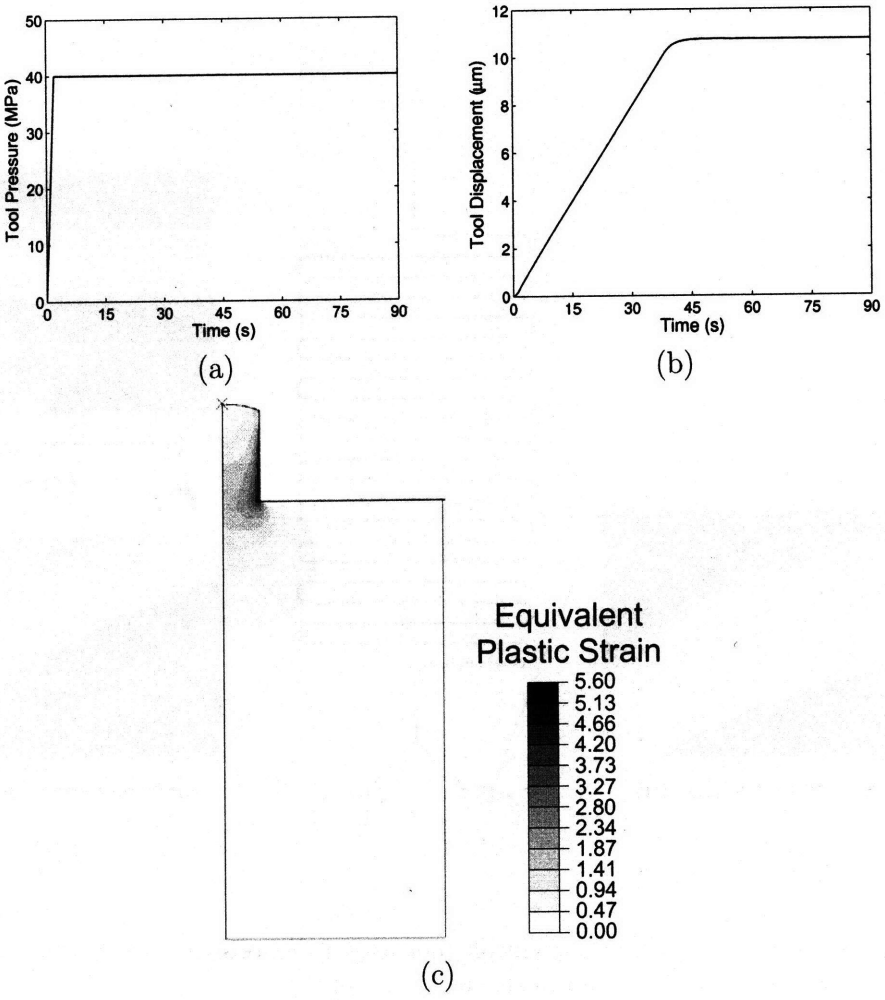

Figure 4-7: (a) Tool pressure history. (b) Tool displacement history. (c) Filled mold at 90 seconds.

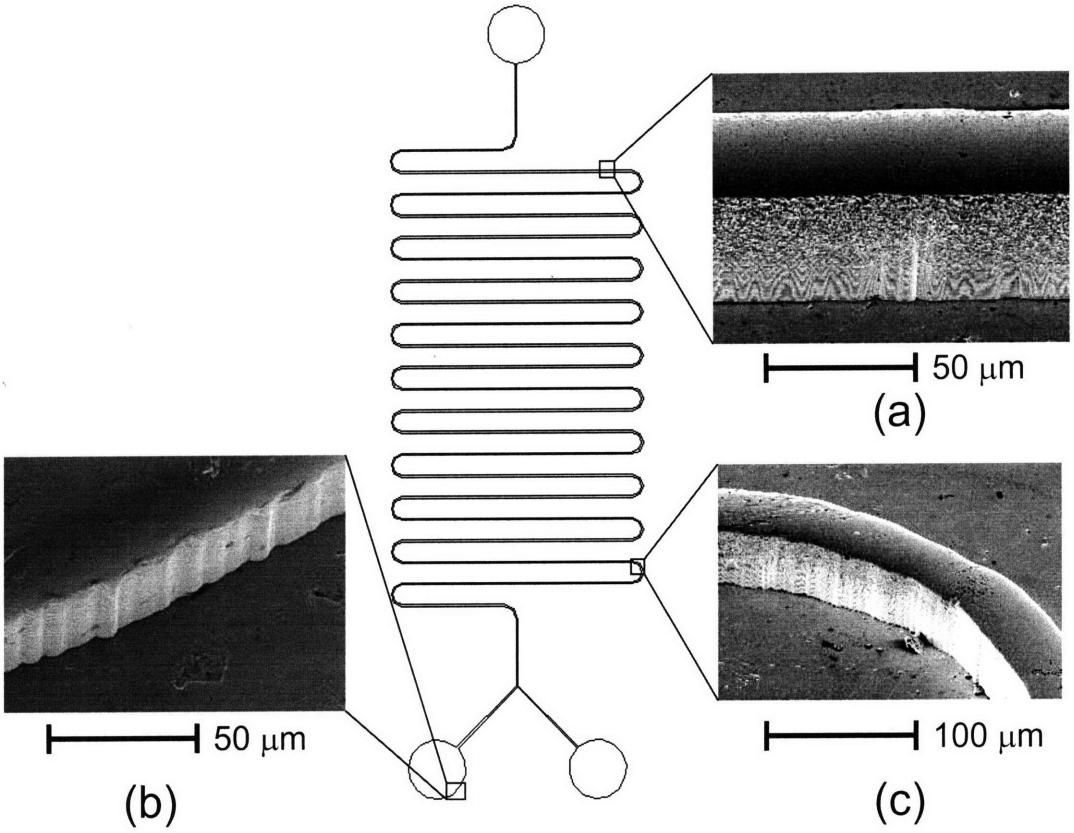

Figure 4-8: SEM results of the micro-hot-embossing of a microfluidic mixer into a metallic glass substrate, including (a) a straight ridge, (b) part of an inlet, and (c) a raised bend.

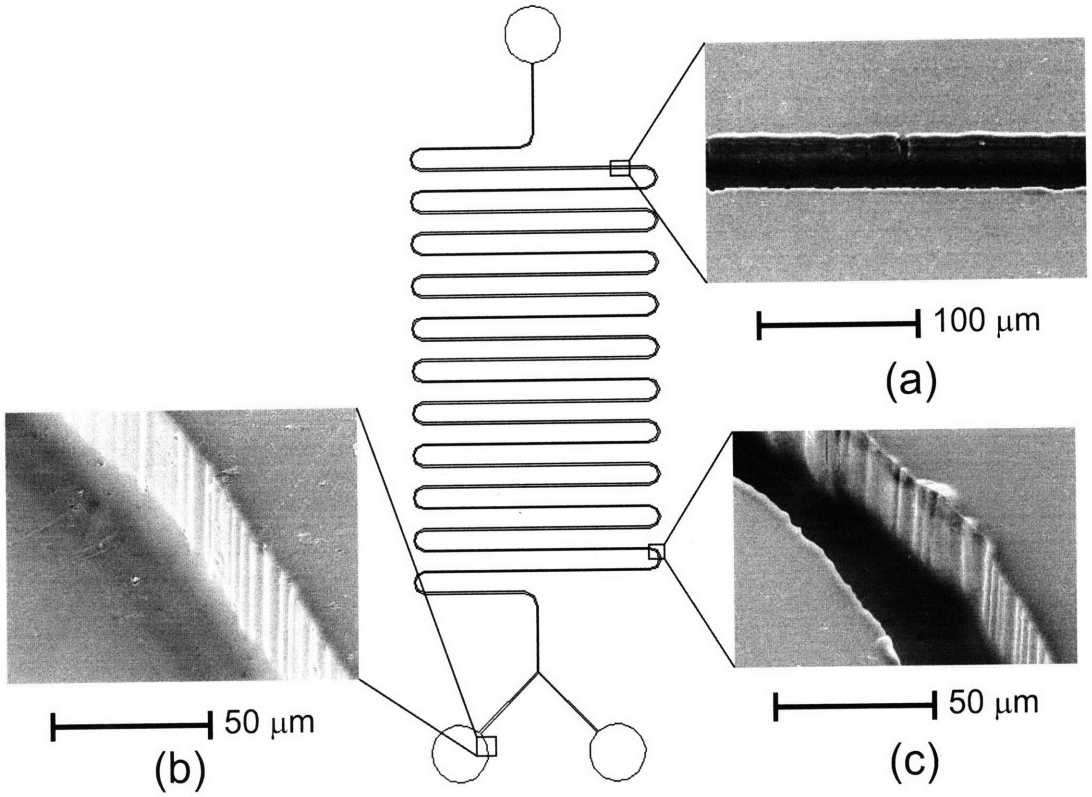

Figure 4-9: SEM results of the micro-hot-embossing of a polymeric microfluidic mixer, including (a) a channel, (b) part of an inlet, and (c) a bend.

Bibliography

[1] Y. Saotome, S. Miwa, T. Zhang, and A. Inoue. The micro-formability of Zr-based amorphous alloys in the supercooled liquid state and their application to micro-dies. *Journal of Materials Processing Technology*, 113:64–69, 2001.

[2] Y. Saotome, K. Itoh, T. Zhang, and A. Inoue. Superplastic nanoforming of Pd-based amorphous alloys. *Scripta Materialia*, 44:1541–1545, 2001.

[3] Y. Saotome, K. Itoh, T. Zhang, and A. Inoue. The micro-nanoformability of Pt-based metallic glass and the nanoforming of three-dimensional structures. *Intermetallics*, 104: 1241–1247, 2002.

[4] Y. Saotome, Y. Noguchi, T. Zhang, and A. Inoue. Characteristic behavior of Pt-based metallic glass under rapid heating and its application to microforming. *Materials Science and Engineering A*, 375:389–393, 2004.

[5] J. Schroers. The superplastic forming of bulk metallic glasses. *Journal of Metals*, 57, 2005.

[6] J. Schroers, T. Nguyen, and A Desai. Thermoplastic forming of bulk metallic glass — a technology for MEMS and microstructure fabrication. *Journal of Microelectromechanical Systems*, 16, 2007.

[7] ABAQUS, Inc. ABAQUS Reference Manuals, 2006.

[8] S. Y. Chou. Nanoimprint lithography and lithographically induced self-assembly. *MRS Bulletin*, 26:512–517, 2001.

[9] T. L. Edwards, S. K. Mohanty, R. K. Edwards, C. Thomas, and A. B. Frazier. Rapid micromold tooling for injection molding microfluidic components. *Sensors and Materials*, 14:167–178, 2002.

[10] M. Heckele and W. K. Schomburg. Review on micro-molding of thermoplastic polymers. *Journal of Micromechanics and Microengineering*, 14:R1–R14, 2004.

[11] T. Nielsen, D. Nilsson, and F. Bundgaard. Nanoimprint lithography in the cycle olefin copolymer, Topas®, a highly ultraviolet-transparent and chemically resistant thermoplast. *Journal of Vacuum Science and Technology B*, 22:1770–1775, 2004.

[12] B. Bilenberg, M. Hansen, D. Johansen, V. Özkapici, C. Jeppesen, P. Szabo, I. M. Obieta, O. Arroyo, J. O. Tegenfeldt, and A. Kristensen. Topas-based lab-on-a-chip microsystems fabricated by thermal nanoimprint lithography. *Journal of Vacuum Science and Technology B*, 23:2944–2949, 2005.

[13] N. M. Ames. A thermo-mechanical finite deformation theory of plasticity for amorphous polymers: application to micro-hot-embossing of poly(methyl methacrylate). PhD thesis, Massachusetts Institute of Technology, June 2007.

[14] V. Srivastava. Personal communication, 2007.

Chapter 5

Concluding remarks

We have generalized the finite-deformation constitutive theory of Anand and Su [1–3] to represent the mechanical response of metallic glasses in the temperature range $0.9\vartheta_g \lesssim \vartheta \lesssim \vartheta_x$. The material parameters appearing in the theory have been estimated for Vitreloy-1 ($\vartheta_g = 623$K) in a temperature range spanning 593K to 683K, and in a strain-rate range of $\approx 10^{-5}$ s^{-1} to 10^{-1} s^{-1}. The calibrated constitutive model reproduces important aspects of the mechanical behavior, such as stress-overshoot and strain-softening as well as the the non-Newtonian viscous-type character of the steady-state response of Vitreloy-1 in this temperature and strain rate range.

The new constitutive theory has been implemented in the finite element program ABAQUS/Explicit (2006) by writing a user material subroutine. This numerical simulation capability is then used to determine appropriate processing parameters in order to carry out representative micron-scale hot-embossing operations. By carrying out corresponding hot-embossing experiments, we have demonstrated that micron-scale features in Vitreloy-1 may be accurately replicated under the processing conditions determined by use of the numerical simulation and design capability reported in this thesis. Furthermore, we have demonstrated an emerging application for the resulting micro-patterned metallic glass parts: as robust tooling for the micro-hot-embossing of polymeric materials.

The constitutive equations and numerical simulation capability presented in this thesis, should facilitate further simulation-based study and design of micro-scale thermoplastic forming processes of metallic glasses.

5.1 Future Work

Below are listed several directions for future work:

- In order to simulate the full hot-embossing process, including heat-up and cool-down, the current theory must be extended to a thermo-mechanically coupled one.

- Recent work towards a constitutive theory for metallic glasses at high temperatures [5, 6] utilize a single internal variable that represents the free volume of the material. In order for a theory of this type to work over a wide range of temperatures and strain rates, an understanding of how the free-volume changes with both deformation and temperature is required; however, the data necessary to formulate a theory of this type does not exist in the literature. Therefore, it is necessary to perform a suite of stress/strain experiments spanning a wide range of temperatures and strain rates, accompanied by the attendant DSC experiments. A set of experiments of this type will provide the necessary insight into the deformation and temperature dependence of the free volume.

- The simulation results appearing in Chapter 4 relied on the implementation of the constitutive equations in an explicit integration scheme. In order to improve the robustness of the numerical simulation capability, an implicit integration procedure for the constitutive equations presented in this thesis needs to be determined.

- The theory presented in this thesis is length-scale independent. However, there are indications in the literature that at sufficiently small length-scales, this is not the case. Thus, higher-order theories of plasticity will need to be explored to capture this length-scale dependence.

Bibliography

[1] L. Anand and C. Su. A theory for amorphous viscoplastic materials undergoing finite deformations, with application to metallic glasses. *Journal of Mechanics and Physics of Solids*, 53:1362–1396, 2005.

[2] C. Su and L. Anand. Plane strain indentation of a Zr-based metallic glass: Experiments and numerical simulation. *Acta Materialia*, 54:179–189, 2006.

[3] L. Anand and C. Su. A constitutive theory for metallic glasses at high homologous temperatures. *Acta Materialia*, 55, 2007.

[4] ABAQUS, Inc. ABAQUS Reference Manuals, 2006.

[5] Q. Yang, A. Mota, and M. Ortiz. A finite deformation constitutive model of bulk metallic glass plasticity. *Computational Mechanics*, 37:194–204, 2006.

[6] P. Thamburaja and R. Ekambaram. Coupled thermo-mechanical modelling of bulk-metallic glasses: Theory, finite-element simulations and experimental verification. *Journal of the Mechanics and Physics of Solids*, 55:1236–1273, 2007.

Appendix A

A heuristic procedure for material parameter estimation

A.1 Introduction

The constitutive model summarized in Chapters 2 and 3 contains 33 material parameters which are used to represent the elastic-viscoplastic behavior of a metallic glass through its glass transition temperature.[1] The material parameters may be grouped according to the following three lists:

(MP1) $\{\nu_0, d_1, d_2, \vartheta_{\text{ref}}, \Delta F_{gl}, \Delta F_{sc}, \Delta_F, V_{gl}, V_{sc}, \Delta_V, \vartheta_{\text{v}}\}$ used to represent the "steady-state" viscoplastic flow;

(MP2) $\{S_0, h_0, b_{\text{dil}}, b_{\text{com}}, \varphi_0, g, \vartheta_0, p, q, k_1, k_2, l_1, l_2, \nu_{\text{ref}}\}$ used to represent the transient stress-overshoot and strain-softening response of the material due to microstructural disordering; and

(MP3) $\{E_{gl}, E_{sc}, \Delta_E, \vartheta_g, k_{E_{gl}}, k_{E_{sc}}, \nu_{gl}, \nu_{sc}\}$ used to represent the temperature dependence of the elastic moduli of the material.

In this Appendix we outline a heuristic procedure for estimating the values of these parameters for a metallic glass. Using available experimental data in the literature [1–3], we illustrate this procedure by estimating the material parameters for Vitreloy-1 in the temperature range $[593, 683]$ K and strain rate range $[10^{-5}, 10^{-1}]\,\text{s}^{-1}$. The literature value of the glass transition temperature of this material is

$$\vartheta_g = 623\text{K}. \tag{A.1}$$

[1] We acknowledge that this is a rather long list, but most of these parameters enter the phenomenological functions employed to represent the strong temperature dependence of the underlying physical quantities.

A.2 Estimation of the parameter list MP1

In simple compression, the principal stresses are

$$\sigma_1 = \sigma_2 = 0, \qquad \sigma_3 < 0. \tag{A.2}$$

Straight-forward calculations using (2.145) and (2.148) show that in this case the resolved shear stresses on the slip systems are given by

$$\tau \stackrel{\text{def}}{=} \tau^{(1)} = \tau^{(2)} = \tau^{(5)} = \tau^{(6)} = -\tfrac{1}{2}\sigma_3, \quad \tau^{(3)} = \tau^{(4)} = 0. \tag{A.3}$$

Thus, (3.6) dictates that the shearing rate on the slip systems must obey,

$$\nu^{(1)} = \nu^{(2)} = \nu^{(5)} = \nu^{(6)} > 0, \quad \text{and} \quad \nu^{(3)} = \nu^{(4)} = 0. \tag{A.4}$$

Further, it is easy to verify that the non-zero resolved shear stresses and shearing rates on the slip systems are given by

$$\tau = \tau^{(1)} = \tau^{(2)} = \tau^{(5)} = \tau^{(6)} = \tfrac{1}{2}\sigma, \quad \text{and} \quad \nu^{(1)} = \nu^{(2)} = \nu^{(5)} = \nu^{(6)} = \tfrac{1}{2}\dot{\epsilon}^p, \tag{A.5}$$

where $\sigma > 0$ and $\dot{\epsilon}^p > 0$ are the axial stress and axial plastic strain rate in a compression test. Thus, in one dimension Equation (3.6) gives

$$\dot{\epsilon}^p = 2\nu_0 \exp\left(-\frac{1}{\zeta}\right) \exp\left(-\frac{\Delta F}{k_B\vartheta}\right) \sinh\left(\frac{(\frac{1}{2}\sigma - S)V}{2k_B\vartheta}\right) \geq 0. \tag{A.6}$$

In a fully-developed flow state at given temperature ϑ and strain rate $\dot{\epsilon}$, when the stress reaches a steady-state "plateau" value σ_{ss}, $\dot{\epsilon} \approx \dot{\epsilon}^p$ and

$$\tau_{ss} \stackrel{\text{def}}{=} \tfrac{1}{2}\sigma_{ss}, \quad \text{and} \quad \nu^p \stackrel{\text{def}}{=} \textstyle\sum_{\alpha=1}^{6} \nu^{(\alpha)} = 2\dot{\epsilon}\,. \tag{A.7}$$

Further, at steady-state at given temperature and strain rate, the order-parameter reaches its steady-state value φ^*, the disordering resistance S goes to zero (cf. (3.14)), and (A.6) reduces to

$$\dot{\epsilon} = 2\nu_0 \exp\left(-\frac{1}{\zeta}\right) \exp\left(-\frac{\Delta F}{k_B\vartheta}\right) \sinh\left(\frac{\sigma_{ss}V}{4k_B\vartheta}\right) \geq 0. \tag{A.8}$$

Equation (A.8) is easily inverted to obtain an expression for steady-state stress as a function of applied strain rate and temperature

$$\sigma_{ss} = \frac{4k_B\vartheta}{V} \sinh^{-1}\left(\frac{\dot{\epsilon}}{2\nu_0} \exp\left(\frac{1}{\zeta}\right) \exp\left(\frac{\Delta F}{k_B\vartheta}\right)\right). \tag{A.9}$$

Equation (A.9), along with experimental data for the steady-state stress as a function of strain rate and temperature [1], as well as the variation of the viscosity of the material

with temperature at high temperatures [2], allow one to estimate numerical values for the parameter list MP1.

The procedure that we have used for estimating the values of these parameters is as follows. First, let

$$\sigma^* \stackrel{\text{def}}{=} \frac{\sigma_{\text{ss}}}{\vartheta}, \qquad \text{and} \qquad \dot{\epsilon}^* \stackrel{\text{def}}{=} \frac{\dot{\epsilon}}{2\nu_0} \exp\left(\frac{1}{\zeta}\right) \exp\left(\frac{\Delta F}{k_B \vartheta}\right), \tag{A.10}$$

define "temperature-compensated" values of σ_{ss} and $\dot{\epsilon}$, respectively, so that (A.9) may be written as

$$\sigma^* = \frac{4k_B}{V} \sinh^{-1}(\dot{\epsilon}^*). \tag{A.11}$$

Thus, at each temperature, σ^* depends linearly on $\sinh^{-1}(\dot{\epsilon}^*)$ as shown schematically in Figure A-1; however, note that the slope of this line depends on temperature because the activation volume is temperature dependent. Note that values of σ^* are known directly from the experimental data of Lu et al. [1]. However, to determine values for $\dot{\epsilon}^*$ one needs a value for the reference strain rate ν_0 and the parameters $\{d_1, d_2, \vartheta_{\text{ref}}, \Delta F_{gl}, \Delta F_{sc}, \Delta_F\}$.

We choose a reference strain rate ν_0 of 5×10^{12} s^{-1} which is on the order of the Debye frequency. For the parameters, d_1, d_2, and ϑ_{ref} in the Grest-Cohen equation (3.16), we employ the viscosity data reported in [2] for Vitreloy-1. These authors fit the temperature dependence of the high-temperature viscosity data using the following functional form

$$\eta(\vartheta) = \eta_0 \exp\left(\frac{1}{\zeta}\right), \quad \text{with} \quad \zeta(\vartheta) = \frac{1}{2d_1}\left[\vartheta - \vartheta_{\text{ref}} + \sqrt{(\vartheta - \vartheta_{\text{ref}})^2 + d_2\vartheta}\right], \tag{A.12}$$

which differs from Equation (3.25) of the present theory, in that it does not contain an activation energy term $\exp(\Delta F/k_B\vartheta)$. We use the values $d_2 = 162$K and $\vartheta_{\text{ref}} = 672$K from [2]; however, we adjust their value of d_1 in order to fit the non-Newtonian viscosity (3.24) estimated by using the data of [1]. Values of d_1 and ΔF were determined by using an iterative procedure. The starting value of d_1 was taken as $d_1 = 4933$K [2], and an activation energy ΔF was estimated for each temperature that would result in the linear relationship (A.11) at that temperature. This process was repeated until the values of d_1 and ΔF for each temperature provided acceptable fits to Equation (A.11). Once the temperature dependence of ΔF was determined, the values of the subsidiary values $\{\Delta F_{gl}, \Delta F_{sc}, \Delta_F\}$ were determined by fitting this data to Equation (3.17). The temperature dependent free volume concentration of Equation (3.16) is plotted in Figure A-2, and the resulting temperature dependent values of the activation energy along with the fit to Equation (3.17) are shown in Figure A-3a.[2] Finally, with the values of $\dot{\epsilon}^*$ determined at each temperature, the activation volume V for each temperature was determined from the slopes of the σ^* versus $\sinh^{-1}(\dot{\epsilon}^*)$ plots at each temperature. The values of activation volume determined in this manner are

[2]It is important to note that while the variation of ΔF with temperature appears to be quite small — from $\Delta F_{gl} = 1.64 \times 10^{-19}$J to $\Delta F_{sc} = 1.51 \times 10^{-19}$ J — it is necessary to account for this variation to obtain a good fit to the values of the steady-state stress over a wide range of temperatures.

plotted in Figure A-3b, and the subsidiary values $\{V_{gl}, V_{sc}, \Delta_V, \vartheta_V\}$ were determined by fitting (3.18) to this data. The values of the parameters in the list MP1, determined using this procedure, are given in Table A.1.

Parameter	Value
ν_0 (s^{-1})	5×10^{12}
d_1 (K)	2865.8
d_2 (K)	162
ϑ_{ref} (K)	672
ΔF_{gl} (J)	1.64×10^{-19}
ΔF_{sc} (J)	1.51×10^{-19}
Δ_F (K)	7.57
V_{gl} (m^3)	1.82×10^{-28}
V_{sc} (m^3)	3.54×10^{-28}
ϑ_V (K)	655.63
Δ_V (K)	9.18

Table A.1: List MP1.

A.3 Estimation of the parameter list MP2

Once the steady-state levels of the flow stress at each temperature and strain rate have been fit adequately by the constitutive model, it remains to determine the parameters $\{S_0, h_0, b_{dil}, b_{com}, \varphi_0, g, \vartheta_0, p, q, k_1, k_2, l_1, l_2, \nu_{ref}\}$ which determine the evolution of S and φ,

Parameter	Value
S_0 (MPa)	0
h_0	40
b_{dil} (GPa)	500
b_{com} (GPa)	125
φ_0	0
g	12.5
ϑ_0 (K)	300
p	1.5
q	0.5
k_1	5.0×10^{-4}
k_2	3.00×10^{-4}
ν_{ref} (s^{-1})	2.00×10^{-5}
l_1 (K)	292
l_2 (K)	9

Table A.2: List MP2.

and control the levels of stress-overshoot and strain-softening in the stress-strain curves. The parameters S_0 and φ_0 describe the initial values of the internal variables. We assume that the material begins in a well-annealed, "ground" state as far as the internal variables S and φ are concerned. Thus, we take S_0 and φ_0 to be zero. The parameter h_0 controls the strain-hardening slope of the curves, b_{dil} affects the peak value, and g controls how quickly the strain-softening occurs, while $\{\vartheta_0, p, q, k_1, k_2, l_1, l_2, \nu_{\text{ref}}\}$ affect the strain rate and temperature sensitivity of the peak value of the stress. First, the values of h_0, g, and b_{dil} were selected following a few trials using different values of these parameters. Next, the necessary value of φ^* to attain the appropriate stress peak value was determined for each stress-strain curve. Then, the values of $\{\vartheta_0, p, q, k_1, k_2, l_1, l_2, \nu_{\text{ref}}\}$ were adjusted to fit the dependence of φ^* on strain rate and temperature. This dependence is shown in Figure A-4. Lastly, an appropriate value for b_{com} was selected based on magnitude of the stress trough in strain rate decrement tests. The values of the parameters in the list MP2 are given in Table A.2.

A.4 Estimation of the parameter list MP3

The temperature dependence of Young's modulus was estimated from the DMA data of [3] for Vitreloy-1. This data provides guidance in choosing values for E_{gl}, Δ_E, and $k_{E_{gl}}$. However, due to the onset of crystallization during a DMA test, reliable data for E is inaccessible for higher temperatures, leaving definite values for E_{sc} and $k_{E_{sc}}$ unclear; for these parameters we simply assume plausible extrapolated values. Likewise, we choose a value for ν_{gl} based on the room temperature value of the Poisson's ratio, and we base our choice for ν_{sc} on the assumption that material is almost incompressible above the glass transition temperature. The values of the parameters in the list MP3, determined using this iterative procedure, are given in Table A.3.

Parameter	Value
E_{gl} (GPa)	80.7
E_{sc} (GPa)	30.0
Δ_E (K)	24.0
$k_{E_{gl}}$ (MPa)	39.0
$k_{E_{sc}}$ (MPa)	39.0
ν_{gl}	0.360
ν_{sc}	0.447

Table A.3: List MP3.

Using the temperature dependent functions (3.19) and (3.21) for the Young's modulus and the Poisson's ratio, we may calculate the temperature dependence of the shear and bulk moduli using (3.22). The temperature dependence of the estimated elastic moduli for Vitreloy-1 is shown in Figure A-5.

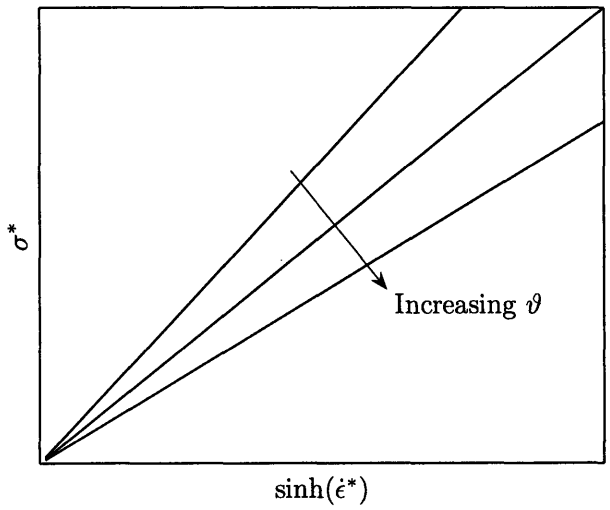

Figure A-1: Schematic of the fit of temperature-compensated strain rate to temperature-compensated stress.

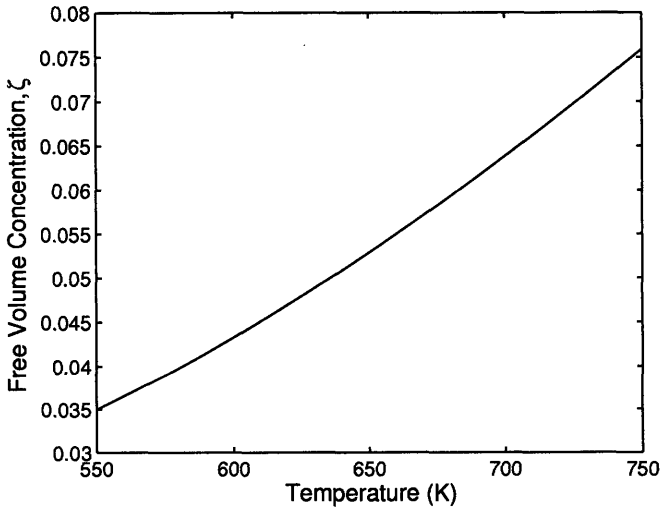

Figure A-2: Free volume concentration as a function of temperature.

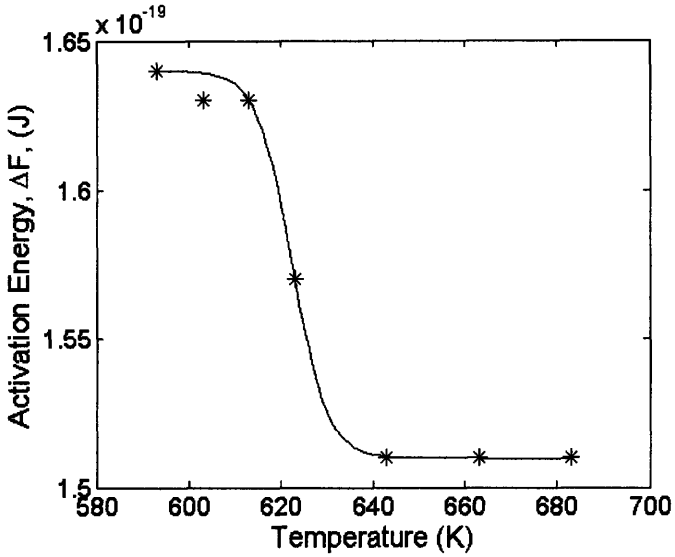

(a)

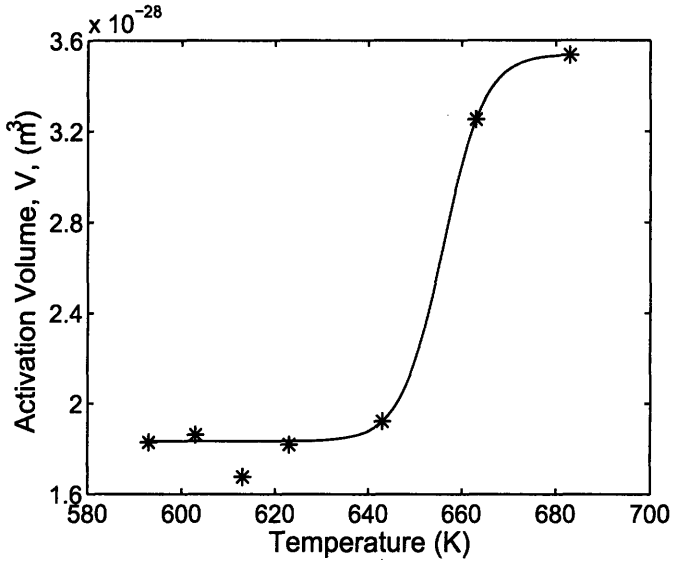

(b)

Figure A-3: (a) Activation energy as a function of temperature. (b) Activation volume as a function of temperature.

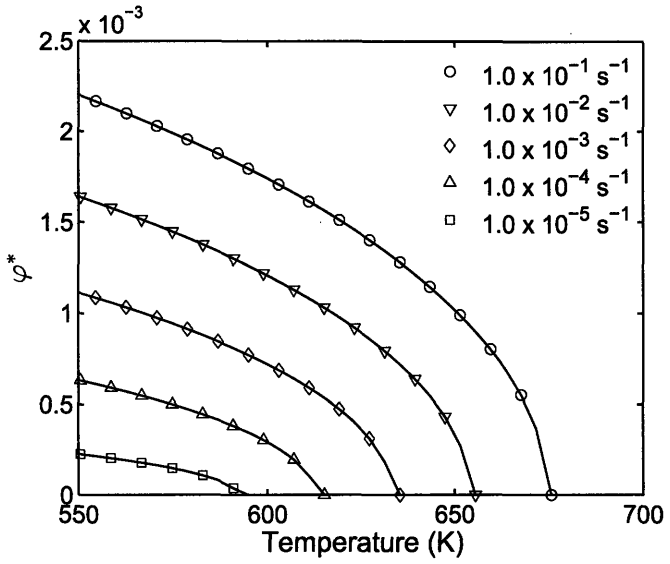

Figure A-4: Dependence of φ^* on strain rate and temperature.

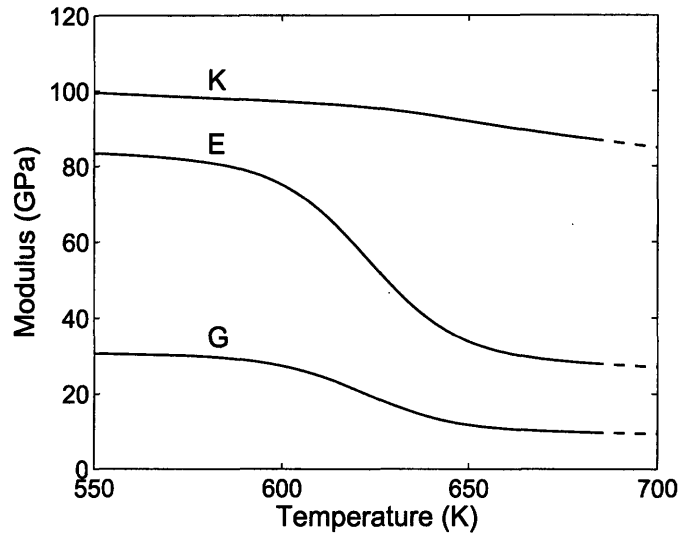

(a)

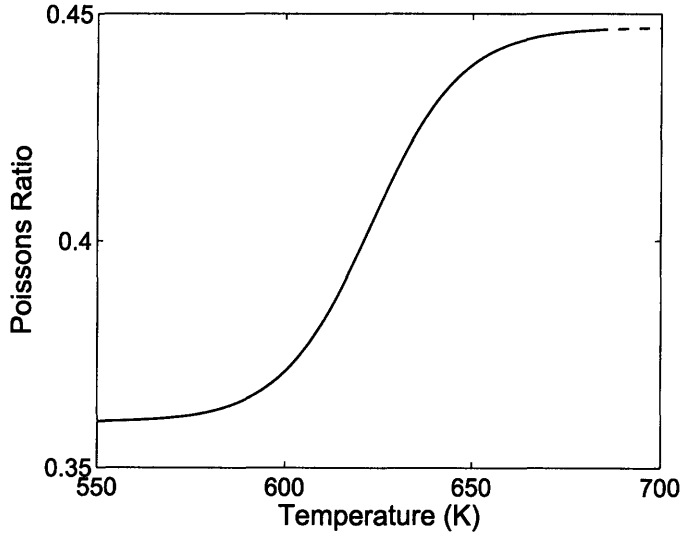

(b)

Figure A-5: (a) Temperature dependence of elastic moduli. (b) Temperature dependence of Poisson's ratio.

Bibliography

[1] J. Lu, G. Ravichandran, and W. L. Johnson. Deformation behavior of the $Zr_{41.2}Ti_{13.8}Cu_{12.5}Ni_{10.0}Be_{22.5}$ bulk metallic glass over a wide range of strain-rates and temperatures. *Acta Materialia*, 51:3429–3443, 2003.

[2] A. Masuhr, T. A. Waniuk, R. Busch, and W. L. Johnson. Time scales for viscous flow, atomic transport, and crystallization in the liquid and supercooled liquid state of $Zr_{41.2}Ti_{13.8}Cu_{12.5}Ni_{10.0}Be_{22.5}$. *Physical Review Letters*, 82, 1999.

[3] Chun-Huei Tsau, Chih-Chung Wu, and Shyue-Sheng Wu. The thermal stability and mechanical behaviors of $Zr-Cu-Ni-Ti-Be$ bulk metallic glasses. *Journal of Materials Processing Technology*, 182:257–261, 2007.

Appendix B

Experimental Details

B.1 Introduction

This appendix explains in detail the micro-hot-embossing experimental procedures described in Chapter 4.

B.2 Procedures

B.2.1 Micro-hot-embossing of metallic glass substrates

The samples of $Zr_{41.2}Ti_{13.8}Cu_{12.5}Ni_{10}Be_{22.5}$ used in this study were obtained from the cases of SanDisk Cruzer Titanium USB Flash Drives. The material was cut into square sheets with sides approximately 12.5 mm in length. After being cut from the case, the sheets are slightly curved. The samples were flattened by applying a pressure of about 40 MPa at 400°C for a few seconds. The flattened samples were then polished to a 1 micron surface finish on a South Bay Technology (SBT) 920 Lapping and Polishing Machine. The resulting sample has a thickness of about 1 mm.

Patterned silicon tools were used in the micro-hot-embossing experiments. To manufacture the tool, a 100 mm diameter (100) silicon wafer was spin-coated with a 10 μm thick layer of AZ4620 positive photoresist (Shipley, Newton, MA). For the plane strain, repeated pattern, the resist was photolithographically patterned with an array of long, parallel rectangular openings that were 240 μm wide spaced 360 μm apart, and for the microfluidic mixer pattern, the resist was patterned with the 50 μm snake mixer pattern. The photoresist served as a mask for the subsequent deep reactive ion etching of the underlying silicon. The silicon was etched to a depth of approximately 33 μm for the plane strain, repeated pattern and to a depth of approximately 65 μm for the mixer pattern, using a fluorine-based inductively coupled plasma in a machine manufactured by Surface Technology Systems of Newport, UK. After etching, the photoresist was stripped from the wafer in a Piranha bath.

SEM images of the plane strain repeated mold and mixer mold are shown in Figures 4-3a,b and 4-6, respectively.

All experiments were conducted using a biaxial servo-hydraulic Instron testing machine having a normal load capacity of 220 kN over an axial travel of 100 mm and a torque capacity of 2.2 kN-m over a rotational travel of 95°. A custom heated load train shown in Figure B-1 was designed for the micro-hot-embossing experiments. The loading blocks are manufactured from H13 tool steel[1], which provides decent heat conduction, but it is also very durable. These are thermally isolated from the rest of the load train by 1 inch thick Cogetherm-P blocks.[2] The load train is attached to the hydraulic Instron grips through platen connectors manufactured from H13 tool steel.[3] An assembly drawing of the load train is shown in Figure B-2, and detailed engineering drawings of each component are shown in Figures B-3, B-4, and B-5. The embossing experiments were conducted under load control. The Instron Waveform Generator software was used to specify the load profiles.

After embossing, the metallic glass part and silicon tool become bonded together. The silicon is removed from the metallic glass by dissolving it away in a heated potassium hydroxide (KOH) bath. A 4.5M KOH solution was prepared at room temperature and heated to 80-90°C on a hot plate. The bonded silicon and metallic glass were placed into the heated solution, and the solution was stirred with a magnetic stirrer at 100 rpm. After about 30 minutes, all of the silicon tool had been dissolved away, leaving the metallic glass part.

B.2.2 Micro-hot-embossing of polymeric substrates

The samples of Zeonex 690R were obtained as 3 mm thick sheets from Zeon Chemicals L.P. and subsequently cut to the appropriate size. The metallic glass tool was manufactured as described above, and the same experimental apparatus as described above was used. After the embossing was completed, the polymeric part and metallic glass tool were left under pressure as the apparatus cooled to below the glass transition of the polymer. This was done to minimize distortion of the features in the polymeric device upon cooling. After the assembly had sufficiently cooled, the pressure was removed, and the polymeric part and metallic glass tool were physically separated. The metallic glass tool suffered no degradation during this process. This is in contrast to the separation of the silicon mold from the metallic glass part where the silicon mold is completely destroyed.

B.2.3 Temperature Control

An easy to control heating system was designed to allow for quick and precise control of the embossing temperature. Each loading block was supplied 800 W of electrical heating power from 4 cartridge heaters,[4] and the temperature in each loading block was measured by a J-

[1]Carpenter Powder Products, H13 Tool Steel, 3.75 in. dia x 12 in. long stock

[2]Foundry Services, Inc.

[3]Carpenter Powder Products, H13 Tool Steel, 2 in. dia x 12 in. long stock

[4]McMaster-Carr 3614K36, 200 W, 1.7 A, 0.25 in. dia., 2 in. length, bonded-graphite coating

type thermocouple probe.[5] Benchtop controllers[6] were used to maintain the temperature in each loading block through a feedback loop between the thermocouple probes and cartridge heaters.

This set-up along with the thermal insulation provided by the Cogetherm-P insulating blocks allowed for temperatures of 500°C and above to be reached in 20 to 30 minutes when heating from room temperature.

[5]Omega JMQSS-062E-6, 304 SS sheath, 0.062 in. dia., 6 in. length, exposed junction, miniature connector
[6]Omega CSC32J-C2/4 benchtop controller

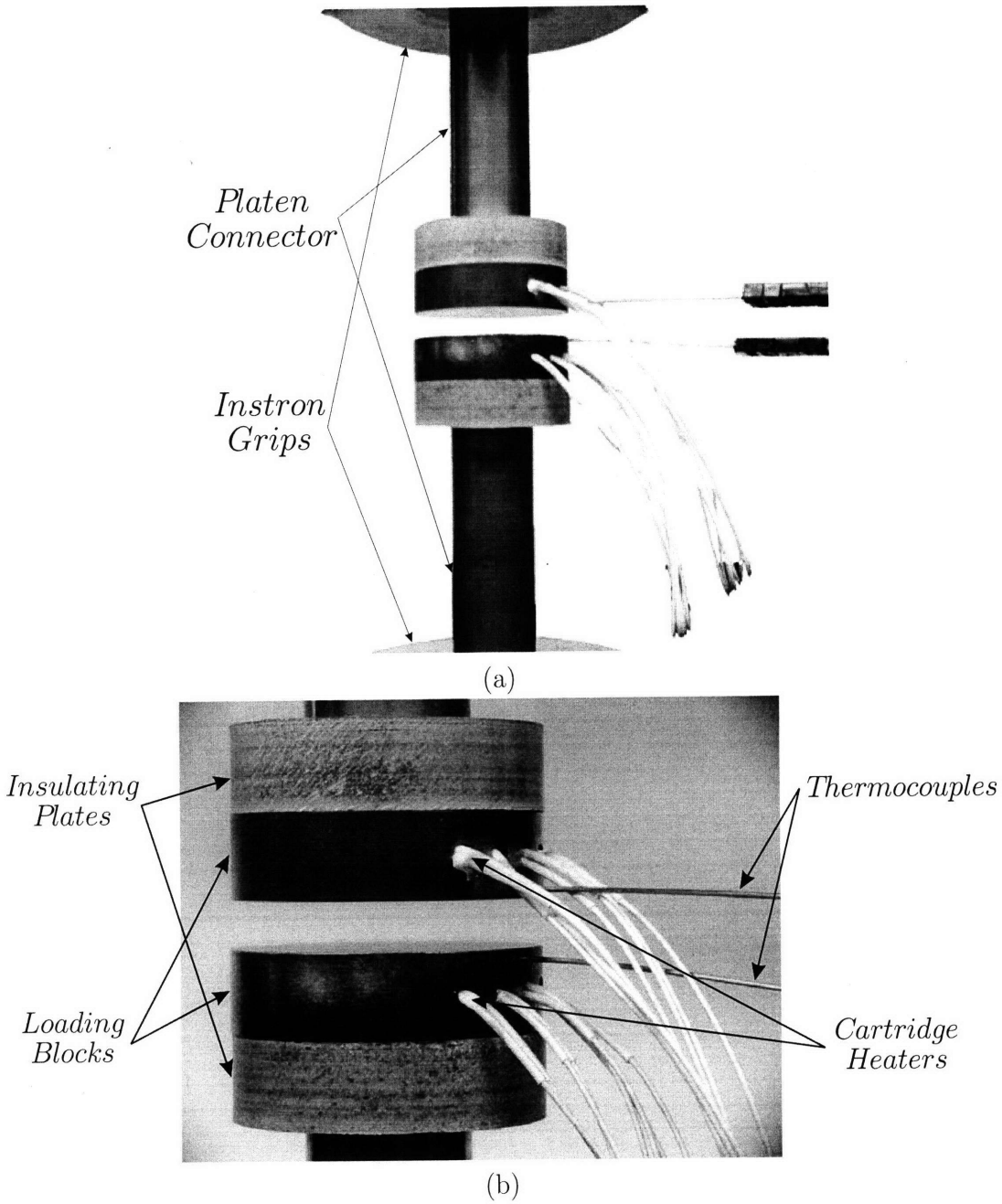

Figure B-1: Images of the experimental set-up used for micro-hot-embossing. (a) Large image of set-up showing platen connectors and Instron grips. (b) Close-up of the experimental set-up showing the cartridge heaters and thermocouples on the right.

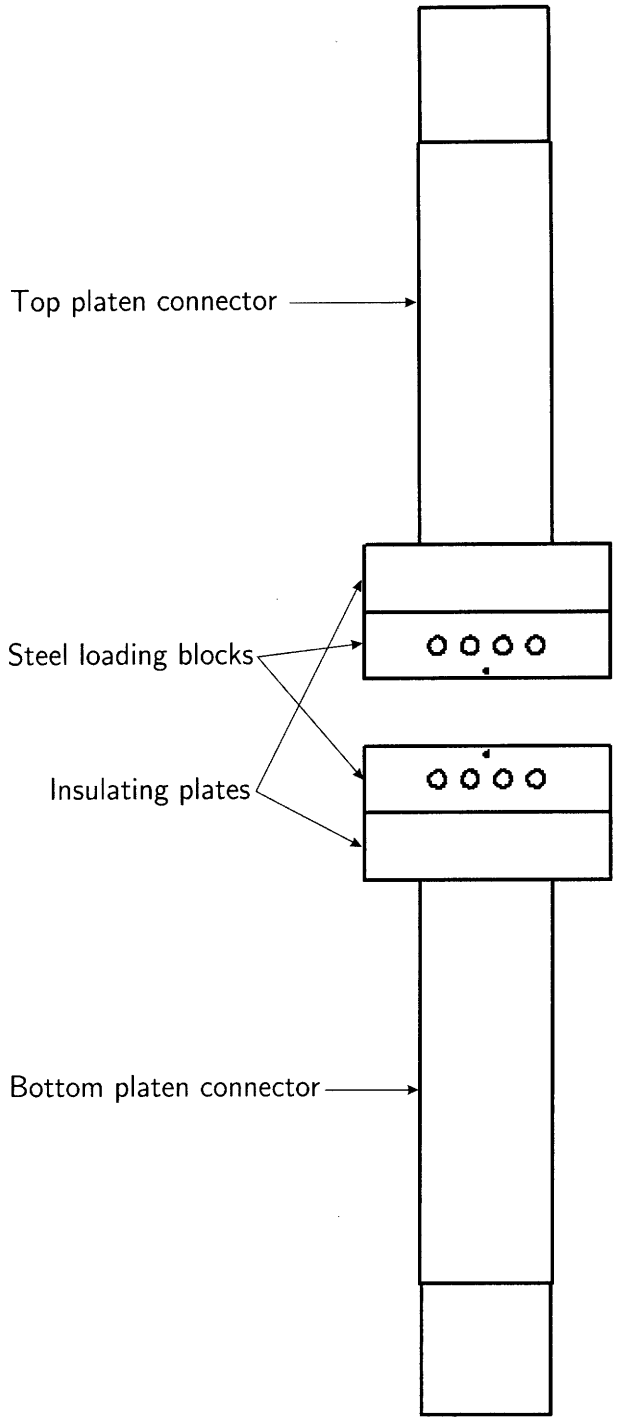

Figure B-2: Assembly drawing of the complete load train.

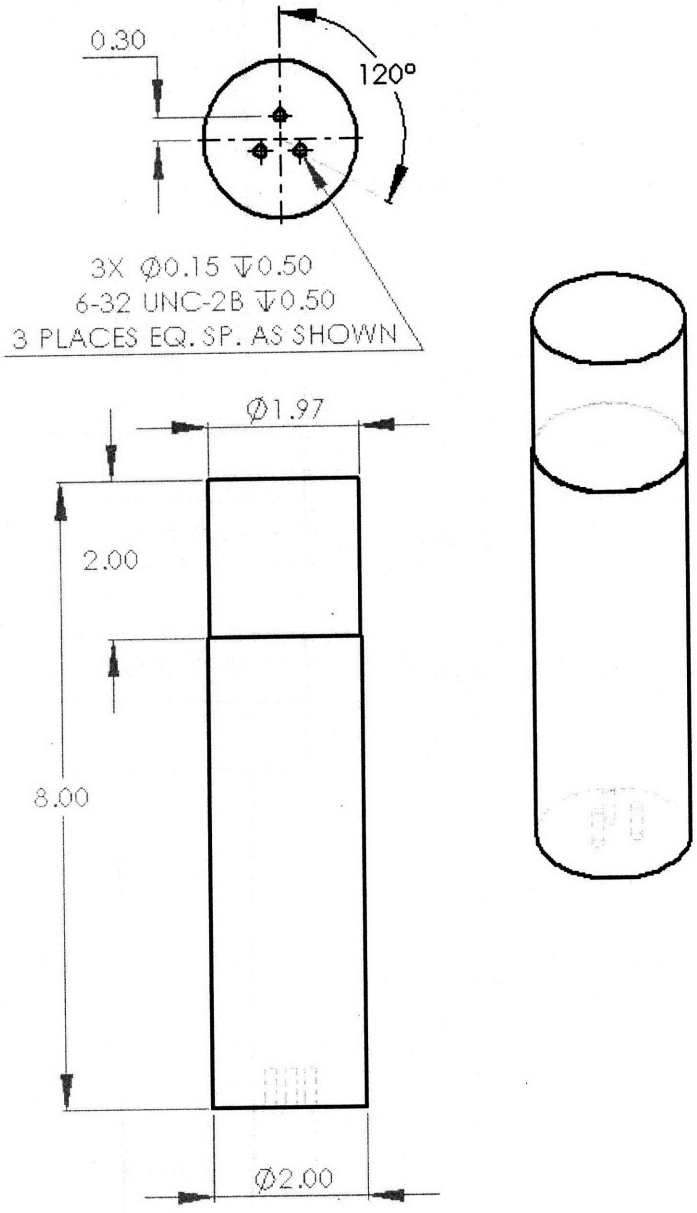

Figure B-3: Drawing of platen connector used to connect load train to the Instron. Dimensions in inches unless otherwise noted.

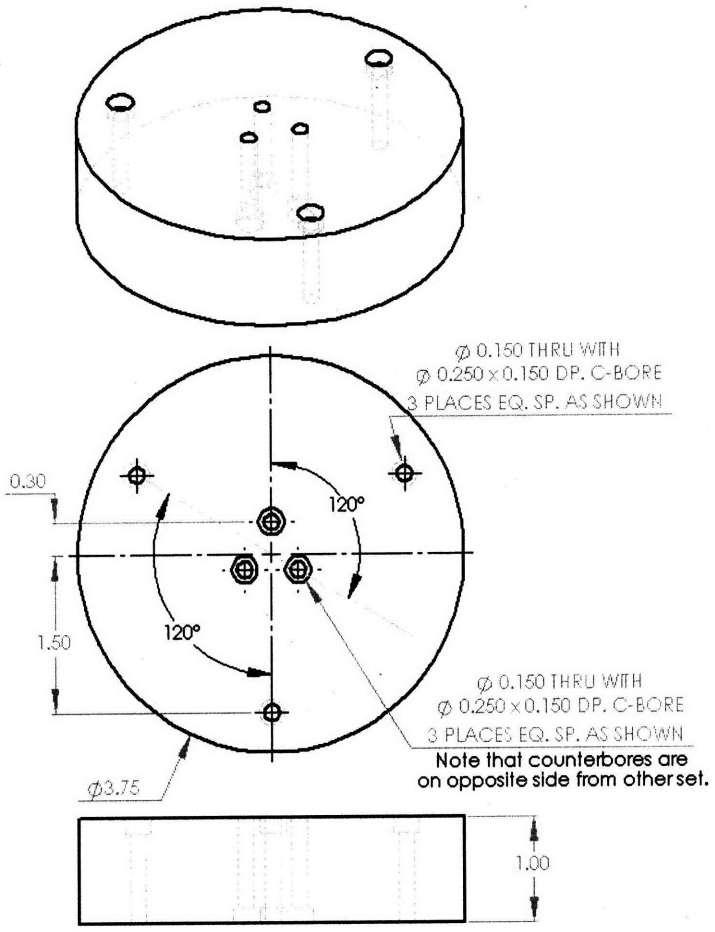

Figure B-4: Drawing of insulating plate. Dimensions in inches unless otherwise noted.

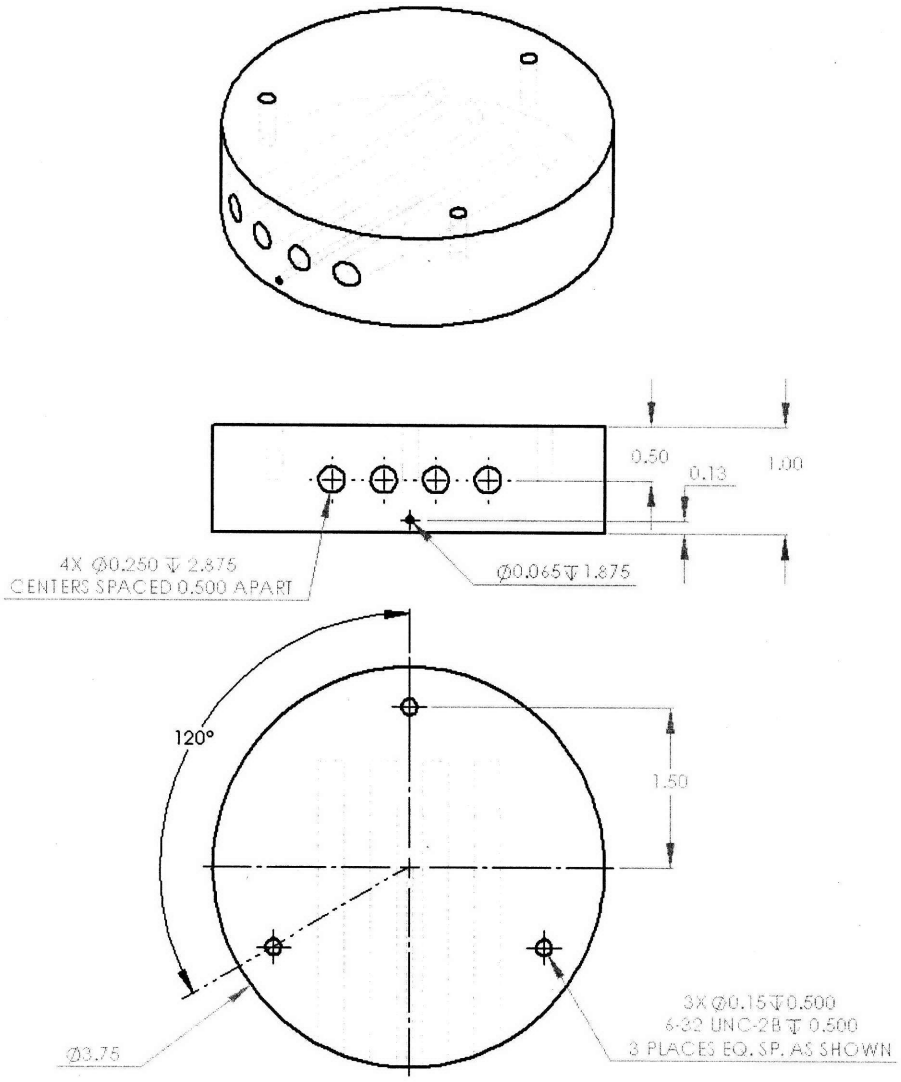

Figure B-5: Drawing of loading block. Dimensions in inches unless otherwise noted.